RMZ

MATERIALS and GEOENVIRONMENT

MATERIALI in GEOOKOLJE

RMZ – M&G, **Vol. 66**, No. 3
pp. 139–210 (2019)

Ljubljana, December 2019

ISSN 1408-7073

RMZ – Materials and Geoenvironment
RMZ – Materiali in geookolje
ISSN 1408-7073

Old title/Star naslov
Mining and Metallurgy Quarterly/Rudarsko-metalurški zbornik
ISSN 0035-9645, 1952–1997

Published by/Izdajatelj
Faculty of Natural Sciences and Engineering, University of Ljubljana/
Naravoslovnotehniška fakulteta, Univerza v Ljubljani

Associated Publisher/Soizdajatelj
Institute for Mining, Geotechnology and Environment, Ljubljana/
Inštitut za rudarstvo, geotehnologijo in okolje
Velenje Coal Mine/Premogovnik Velenje
Slovenian Chamber of Engineers/Inženirska zbornica Slovenije

Editorial Office/Uredništvo
Technical editors/Tehnična urednika Teja Čeru and Jože Žarn
Secretary/Tajnica Nives Vukič

Editorial Address/Naslov uredništva
RMZ – Materials and Geoenvironment
Aškerčeva cesta 12, p. p. 312
1001 Ljubljana, Slovenija
Tel.: +386 (0)1 470 46 10
Fax.: +386 (0)1 470 45 60
E-mail: rmz-mg@ntf.uni-lj.si

Published/Izhajanje
4 issues per year/4 številke letno

Partly funded by Ministry of Education, Science and Sport of Republic of Slovenia./Pri financiranju revije sodeluje Ministrstvo za izobraževanje, znanost in šport Republike Slovenije.

Articles published in Journal "RMZ M&G" are indexed in international secondary periodicals and databases:/Članki, objavljeni v periodični publikaciji „RMZ M&G", so indeksirani v mednarodnih sekundarnih virih:
CA SEARCH® – Chemical Abstracts®, METADEX®, GeoRef.

Annual subscription for individuals in Slovenia: 20 EUR, for institutions: 30 EUR. Annual subscription for the rest of the world: 30 EUR, for institutions: 50 EUR/Letna naročnina za posameznike v Sloveniji: 20 EUR, za inštitucije: 30 EUR. Letna naročnina za tujino: 30 EUR, inštitucije: 50 EUR

Transaction account/Tekoči račun
Nova Ljubljanska banka, d. d., Ljubljana: UJP 01100-6030708186

VAT identification number/Davčna številka
24405388

Online Journal/Elektronska revija
www.rmz-mg.com
www.degruyter.com/view/j/rmzmag

Table of Contents

Kazalo

Historical Review

More than 90 years have passed since the University Ljubljana in Slovenia was founded in 1919. Technical fields were united in the School of Engineering that included the Geologic and Mining Division, while the Metallurgy Division was established only in 1939. Today, the Departments of Geology, Mining and Geotechnology, Materials and Metallurgy are all part of the Faculty of Natural Sciences and Engineering, University of Ljubljana.

Before World War II, the members of the Mining Section together with the Association of Yugoslav Mining and Metallurgy Engineers began to publish the summaries of their research and studies in their technical periodical Rudarski zbornik (Mining Proceedings). Three volumes of Rudarski zbornik (1937, 1938 and 1939) were published. The War interrupted the publication and it was not until 1952 that the first issue of the new journal Rudarsko-metalurški zbornik – RMZ (Mining and Metallurgy Quarterly) was published by the Division of Mining and Metallurgy, University of Ljubljana. Today, the journal is regularly published quarterly. RMZ – M&G is co-issued and co-financed by the Faculty of Natural Sciences and Engineering Ljubljana, the Institute for Mining, Geotechnology and Environment Ljubljana, and the Velenje Coal Mine. In addition, it is partly funded by the Ministry of Education, Science and Sport of Slovenia.

During the meeting of the Advisory and the Editorial Board on May 22, 1998, Rudarsko-metalurški zbornik was renamed into "RMZ – Materials and Geoenvironment (RMZ – Materiali in Geookolje)" or shortly RMZ – M&G. RMZ – M&G is managed by an advisory and international editorial board and is exchanged with other world-known periodicals. All the papers submitted to the RMZ – M&G undergoes the course of the peer-review process.

RMZ – M&G is the only scientific and professional periodical in Slovenia which has been published in the same form for 60 years. It incorporates the scientific and professional topics on geology, mining, geotechnology, materials and metallurgy. In the year 2013, the Editorial Board decided to modernize the journal's format.

A wide range of topics on geosciences are welcome to be published in the RMZ – Materials and Geoenvironment. Research results in geology, hydrogeology, mining, geotechnology, materials, metallurgy, natural and anthropogenic pollution of environment, biogeochemistry are the proposed fields of work which the journal will handle.

Editor-in-Chief

Zgodovinski pregled

Že več kot 90 let je minilo od ustanovitve Univerze v Ljubljani leta 1919. Tehnične stroke so se združile v Tehniški visoki šoli, ki sta jo sestavljala oddelka za geologijo in rudarstvo, medtem ko je bil oddelek za metalurgijo ustanovljen leta 1939. Danes oddelki za geologijo, rudarstvo in geotehnologijo ter materiale in metalurgijo delujejo v sklopu Naravoslovnotehniške fakultete Univerze v Ljubljani.

Pred 2. svetovno vojno so člani rudarske sekcije skupaj z Združenjem jugoslovanskih inženirjev rudarstva in metalurgije začeli izdajanje povzetkov njihovega raziskovalnega dela v Rudarskem zborniku. Izšli so trije letniki zbornika (1937, 1938 in 1939). Vojna je prekinila izdajanje zbornika vse do leta 1952, ko je izšel prvi letnik nove revije Rudarsko-metalurški zbornik – RMZ v izdaji odsekov za rudarstvo in metalurgijo Univerze v Ljubljani. Danes revija izhaja štirikrat letno. RMZ – M&G izdajajo in financirajo Naravoslovnotehniška fakulteta v Ljubljani, Inštitut za rudarstvo, geotehnologijo in okolje ter Premogovnik Velenje. Prav tako izdajo revije financira Ministrstvo za izobraževanje, znanost in šport.

Na seji izdajateljskega sveta in uredniškega odbora je bilo 22. maja 1998 sklenjeno, da se Rudarsko-metalurški zbornik preimenuje v RMZ – Materiali in geookolje (RMZ – Materials and Geoenvironment) ali skrajšano RMZ – M&G. Revijo RMZ – M&G upravljata izdajateljski svet in mednarodni uredniški odbor. Revija je vključena v mednarodno izmenjavo svetovno znanih publikacij. Vsi članki so podvrženi recenzijskemu postopku.

RMZ – M&G je edina strokovno-znanstvena revija v Sloveniji, ki izhaja v nespremenjeni obliki že 60 let. Združuje področja geologije, rudarstva, geotehnologije, materialov in metalurgije. Uredniški odbor je leta 2013 sklenil, da posodobi obliko revije.

Za objavo v reviji RMZ – Materiali in geookolje so dobrodošli tudi prispevki s širokega področja geoznanosti, kot so: geologija, hidrologija, rudarstvo, geotehnologija, materiali, metalurgija, onesnaževanje okolja in biokemija.

Glavni urednik

Original scientific paper

Received: Dec 03, 2019
Accepted: Dec 16, 2019
DOI: 10.2478/rmzmag-2019-0018

Analysis of Chemical Composition Homogeneity in the Cross-section of the Rods Produced from Alloys of 6xxx Group

Analiza homogenosti kemijske sestave po preseku litih drogov izdelanih iz zlitin iz skupine 6xxx

Maja Vončina[1,*], Peter Cvahte[2], Ana Kračun[2], Tilen Balaško[1], Jožef Medved[1]

[1] Faculty of Natural Sciences and Engineering, Department for Materials and Metallurgy, University of Ljubljana, Ljubljana, Slovenia

[2] Impol Group, Partizanska 38, 2310 Slovenska Bistrica, Slovenia

* maja.voncina@omm.ntf.uni-lj.si

Abstract

The alloys from Al–Mg–Si system provide an excellent combination of mechanical properties, heat treatment at extrusion temperature, good weldability, good corrosion resistance and formability. Owing to the high casting speed of rods or slabs, the solidification is rather non-equilibrium, resulting in defects in the material, such as crystalline segregations, the formation of low-melting eutectics, the unfavourable shape of intermetallic phases and the non-homogeneously distributed alloying elements in the cross-section of the rods or slabs and in the entire microstructure. The inhomogeneity of the chemical composition and the solid solution negatively affects the strength, the formability in the warm and the corrosion resistance, and can lead to the formation of undesired phases due to segregation in the material. In this experimental investigation, the cross-sections of the rods from two different alloys of the 6xxx group were investigated. From the cross-sections of the rods, samples for differential scanning calorimetry (DSC) at three different positions (edge, D/4 and middle) were taken to determine the influence of inhomogeneity on the course of DSC curve. Metallographic sample preparation was used for microstructure analysis, whereas the actual chemical composition was analysed using a scanning electron microscope (SEM) and an energy dispersion spectrometer (EDS).

Key words: casted rods for extrusion, homogeneity of chemical composition, DSC analysis, microstructure.

Povzetek

Zlitine iz sistema Al-Mg-Si zagotavljajo odlično kombinacijo mehanskih lastnosti, toplotno obdelavo pri temperaturi ekstruzije, dobro varivost, dobro korozijsko odpornost in preoblikovalnost. Zaradi visoke hitrosti ulivanja drogov ali bram je strjevanje dokaj neenakomerno, kar ima za posledico nastanek napak v materialu, kot so kristalne segregacije, tvorba nizkotaljivih evtektikov, neugodna oblika intermetalnih faz in nehomogena porazdelitev legirnih elementov po preseku drogov ali bram in v celotni mikrostrukturi. Nehomogenost kemične sestave in trdne raztopine negativno vpliva na trdnost, preoblikovalnost v toplem ter korozijsko odpornost, poleg tega pa lahko vodi do tvorbe nezaželenih faz zaradi segregacije v materialu. V tej eksperimentalni preiskavi smo preučili preseka drogov dveh različnih zlitin iz skupine 6xxx. Vzorci za diferencialno vrstično kalorimetrijo (DSC) so bili odvzeti iz prečnega prereza droga na treh različnih mestih (rob, D/4 in sredina), z namenom ugotavljanja vpliva nehomogenosti na potek DSC krivulje. Za analizo mikrostrukture smo uporabili metalografski vzorec, medtem ko smo dejansko kemijsko sestavo analizirali z energijsko disperzijskim spektrometrom (EDS) na vrstičnem elektronskem mikroskopu (SEM).

Ključne besede: liti drogovi za ekstrudiranje, homogenost kemične sestave, DSC analiza, mikrostruktura.

Introduction

Aluminium alloys from the group 6xxx have good mechanical properties, good formability and corrosion resistance. Alloyed elements affect weldability, corrosion resistance, corrosion cracking, electrical conductivity and density. Alloying magnesium and silicon to aluminium alloys from the group 6xxx takes place in the appropriate ratio (Mg/Si = 1.73) to form the Mg_2Si phase [1]. In practice, alloys of the 6xxx system produced by casting techniques containing excess silicon or magnesium. Excess silicon results in higher strength and increases their transformability but reduces corrosion resistance. Excess magnesium increases corrosion resistance but reduces transformability and strength [2, 3].

The presence of iron in alloys of the 6xxx system results in the formation of phases such as Al_3Fe, Al_8Fe_2Si, $Al_8FeMg_3Si_6$ and Al_6Fe, which may be detrimental to the properties of these alloys [4]. Iron reduces ductility and toughness by forming coarse components with aluminium and other alloying elements. It also reduces strength, corrosion resistance and fatigue resistance. The alloying elements of chromium and manganese correct the shape and size of iron phases and its compounds in alloys of the 6xxx system. The presence of manganese not only increases the temperature of recrystallisation and corrosion resistance but also allows dispersion hardening and ageing [2].

Although alloys from the group 6xxx have lower strength than alloys from the groups 2xxx and 7xxx, they have advantages such as good formability and corrosion resistance. Bismuth and lead can also be added for better machining by cutting. These alloys are used for profiles for doors, windows, ladders, walls and fences. They are used for the manufacture of frames for motors and cabinets of electric motors, heating and cooling pipes, office equipment, etc. [5].

The production of products from the alloys of the group 6xxx begins with the continuous or semi-continuous casting of the rods, followed by homogenisation. With a higher degree of homogenisation, better formability properties can be expected, which are crucial for further processing. Homogenisation annealing is the process by which crystal segregations and low-melting eutectics are eliminated, the shape of intermetallic phases is changed and small precipitates are formed. The homogenisation process achieves a uniform distribution of the alloying elements throughout the entire microstructure. The inhomogeneity of the solid solution can adversely affect the corrosion/oxidation resistance, strength, working temperature (consequence of artificial reduction of melting point in interdendritic spaces) and formability in a warm, and can cause undesired phases due to segregation [6, 7]. Thus, by means of homogenisation annealing, the formability of bars, ingots and other cast semi-finished products is improved; in this case, casted rods made of aluminium alloys, since they have non-homogeneously distributed alloying elements throughout the microstructure [8–10].

The uneven distribution of alloying elements inside the dendritic microstructure is a feature of high cooling rates. These differences increase with increasing cooling rates and greater differences in the composition between the melt and the solid phases at the beginning of crystallisation, which in some alloys can only be equated with long-term homogenisation as a result of solid-phase diffusion processes [11–13].

Owing to the non-equilibrium solidification, in the solid state, eutectic can be obtained, which according to the theoretical phase diagram should not form. Lowering the temperature at which incipient fusion started is so called a non-equilibrium solidus (NRS). In order to avoid local incipient fusion, each heat treatment must be carried out below the NRS temperature. Local incipient fusion may result in the formation of porosity resulting from the dissolution of non-equilibrium phases. The cracks formed during the forming can be the result of a molten eutectic phase that does not dissolve.

The degree of inhomogeneity is influenced by several different factors. The wider interval of solidification of the individual alloy in practical and theoretical aspects contributes to greater non-homogeneity. The increase in non-homogeneity is also influenced by the difference in the size of the solvent atoms and dissolved atoms, and their crystalline structure [5, 11].

The homogenisation annealing of cast structures to improve the formability was developed on the basis of empirical methods for determin-

ing the time and temperature of the annealing. One of the determining factors is diffusion. In the empirical determination of the time and temperature of the annealing, the diffusivity of the local chemical composition must be taken into account. The diffusion of individual particles can be used to approximately determine the diffusion time, for which the following expression (1) can be used: [8, 10].

$$\sim \frac{x^2}{D} \tag{1}$$

In this equation x is the diffusion path and represents half of the space between the secondary dendritic arms. Therefore, the process of homogenisation is more effective if the grains are smaller, since the elements need to take a shorter path. D represents the diffusivity given in the following equation, whereas D_0 represents diffusion constant; Q is the activation energy for the diffusion; R is a gas constant and T is the temperature at which diffusion takes course.

$$D = D_0 \exp\left(\frac{-Q}{RT}\right) \tag{2}$$

According to this equation, the temperature has an exponential influence on the diffusion and consequently also on the time and temperature of homogenisation. By homogenisation annealing, only micro-segregation can be influenced. By the solidification of large castings, macro-segregations may occur, which may also be one metre high and could not be affected by homogenisation annealing [11].

In Table 1, the calculation of the diffusion coefficients of the various elements and the time needed at the certain temperature at which the element travels 50 µm (the hypothetical half-distance between the secondary dendritic arms) are given. Table 1 shows that the time drastically reduces with the rising temperature. Among the selected elements, the longest diffusion times are for manganese, where at a temperature of 600°C, the homogenisation annealing should last as much as for 567.3 h. Among other elements, only iron is also more difficult, which requires 21.6 h at the same temperature, while for other elements, the diffusion at a distance of 50 µm takes place in 2.2 h (Cu), 2.1 h (Al – self – diffusion), 0.7 h (Si), 0.5 h (Mg) and 0.3 h (Zn) [14–17].

Table 1: *Diffusion of elements in aluminium at temperatures 550, 600 and 650°C at a distance of 50 mm [14–17].*

Element	T [°C]	D [cm²/s]	t [h]
Al	550	9.64E-10	7.2
	600	3.32E-09	2.1
	650	9.98E-09	0.7
Fe	550	6.70E-11	103.6
	600	3.22E-10	21.6
	650	1.30E-09	5.3
Si	550	3.21E-09	2.2
	600	1.04E-08	0.7
	650	2.95E-08	0.2
Mg	550	4.30E-09	1.6
	600	1.31E-08	0.5
	650	3.55E-08	0.2
Mn	550	2.01E-12	3461.6
	600	1.22E-11	567.3
	650	6.14E-11	113.1
Cu	550	9.83E-10	7.1
	600	3.15E-09	2.2
	650	8.88E-09	0.8
Zn	550	7.30E-09	1.0
	600	2.00E-08	0.3
	650	4.92E-08	0.1

Owing to all the factors listed earlier, which influence the quality of the production of cast rods, the process of homogenisation and further processing of rods, two cross-sections of the rods from two different alloys of the 6xxx group, were analysed in this study. From the cross-sections of the rods, samples for differential scanning calorimetry (DSC) were taken at three locations in order to determine the effect of inhomogeneity on the DSC curve. The samples after the DSC analysis were, furthermore, metallographically prepared and microstructure was analysed, where the actual chemical composition was analysed using a scanning electron microscope (SEM) and an energy dispersion spectrometer (EDS).

Materials and Methods

Based on the chemical composition of investigated alloys, which correspond to the EN AW-6008 and EN AW-6060 standards given in Table 2, a simulation of the thermodynamically non-equilibrium solidification according to Scheil was performed using the Thermo-Calc software and the TCAL6 database.

In addition, DSC analysis was performed in order to determine the temperature changes and the thermal effects that occur during heating/melting and cooling/solidification of the investigated alloys. Experiments were carried out using the STA Jupiter 449C device from Netzsch by placing two identical corundum crucibles on the platinum sensor. In one crucible, the investigated sample, and in the other, a comparative (inert) sample was placed. The system was heated in a furnace according to the pre-programmed temperature program up to 720°C. At this temperature, it was kept for 10 minutes. Heating and cooling stages were carried out at a constant rate of 10 K/min. The test was performed in a protective atmosphere of argon Ar 6.0. During the measurement, the apparatus measured the temperature, the difference in temperatures between the investigated and the comparative samples and the time. DSC analysis was carried out on cast samples taken from the centre, on D/4 and on the edge of the cross-section of the rod. The samples were cut from the cross-section of the rod and turning at a diameter of 4.5 mm and a height of 4 mm, which were inserted into the device where analysis was performed.

Table 2: *Chemical composition of investigated alloys according to EN-AW standards in wt.%.*

Alloy	Si	Fe	Cu	Mn	Mg	Cr	Zn	Ti	V	Al
6008	0.50–0.90	0.35	0.30	0.30	0.40–0.70	0.30	0.20	0.10	0.05–0.20	Rest
6060	0.30–0.60	0.10–0.30	0.10	0.10	0.35–0.60	0.05	0.15	0.10	–	Rest

After the measurements, the heating and cooling DSC curves were plotted; the characteristic temperatures were determined from heating and cooling DSC curves, and the influence of the sampling site on the characteristic temperatures was analysed. After the DSC analysis, the samples were metallographically prepared and photographed using a BX61 light microscope with the purpose of analysing the influence of the sampling site from the cross-section of the rod on the formation and distribution of microstructural components. Furthermore, using the SEM Jeol JSM-7600F and EDS analyzer NCA Oxford 350 EDS SDD, the chemical composition of all samples after DSC analysis was analysed, and the homogeneity of the chemical composition in the intersection of the rod was analysed.

Results and Discussion

Figure 1a shows the calculated cooling curve of the alloy EN AW-6008 (Scheil's model), with the dotted line showing the course of equilibrium solidification. In this alloy, according to the calculation, in the microstructure, the primary α-Al, eutectic α-Al + $Al_{15}Si_2M_4$ and eutectic α-Al + $Al_{15}Si_2M_4$ + $Al_9Fe_2Si_2$ phases can be expected, while at a lower temperature (approximately 568°C), the eutectic phases $Al_{18}Fe_2Mg_7Si_{10}$ and Mg_2Si can solidify. Non-equilibrium solidification begins at 654°C and ends at 558°C. In the following, the Scheil's model of non-equilibrium solidification taking into account the large diffusion coefficients of the elements of silicon and magnesium is calculated (Figure 1b). In this case, only three phases are obtained: α-Al, eutectic α-Al + $Al_{15}Si_2M_4$ and eutectic α-Al + Al_8Fe_2Si. The solidification starts at T_L = 654°C and ends at T_S = 603°C.

Figure 2 shows the calculated cooling curve of the alloy EN AW-6060 (Scheil's model). In this alloy, the primary crystals of α-Al, eutectic α-Al + $Al_{13}Fe_4$ and eutectic α-Al + $Al_{13}Fe_4$ + Al_8Fe_2Si can be found in the microstructure; the phase

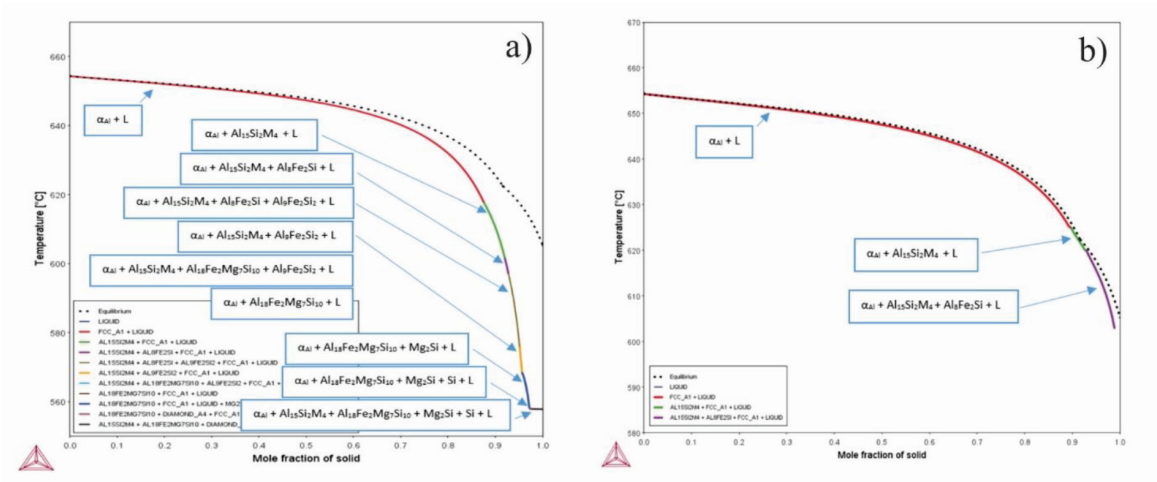

Figure 1: *The cooling curve of the non-equilibrium solidification of the alloy EN AW-6008 without considering the diffusion (a) and taking into account the larger diffusion coefficients of the elements of silicon and magnesium (b).*

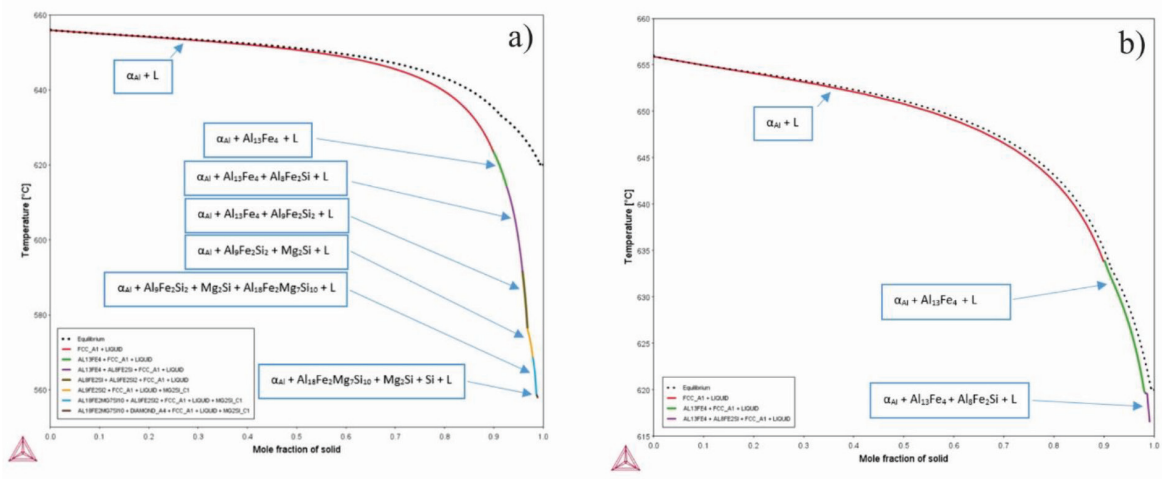

Figure 2: *The cooling curve of the non-equilibrium solidification of the alloy EN AW-6060 without considering the diffusion (a) and taking into account the larger diffusion coefficients of the elements of silicon and magnesium (b).*

Al_8Fe_2Si is transformed into the phase $Al_9Fe_2Si_2$; also at a lower temperature, the eutectic phases $Al_{18}Fe_2Mg_7Si_{10}$ and Mg_2Si can solidify. Non-equilibrium solidification begins at 656°C and ends at 557°C. Figure 2b shows Scheil's model of non-equilibrium solidification taking into account the large diffusion coefficients of silicon and magnesium. In this case, only three phases are obtained in the non-equilibrium curve: α-Al, eutectic α-Al + $Al_{13}Fe_4$ and eutectic α-Al + $Al_{13}Fe_4$ + Al_8Fe_2Si. The solidification starts at T_L = 656°C and ends at T_S = 616°C.

At the heating DSC curve, the Al_3Ti and AlMg-β phases at the temperature of 233.2°C and 282.4°C, respectively, presumably precipitate (Figure 3b), which was verified by thermodynamic calculations/simulations of equilibrium solidification and is a consequence of the supersaturated solid solution of the pre-hardened alloy. At 601.0°C, the eutectic α-Al + Al_8Fe_2Si melts, which represents a solidus temperature, and at a temperature of 609.6°C, the eutectic α-Al + $Al_{15}Si_2M_4$ melts with respect to the Scheil's calculation in Figure 1. Furthermore, at 646.8°C, melting of primary

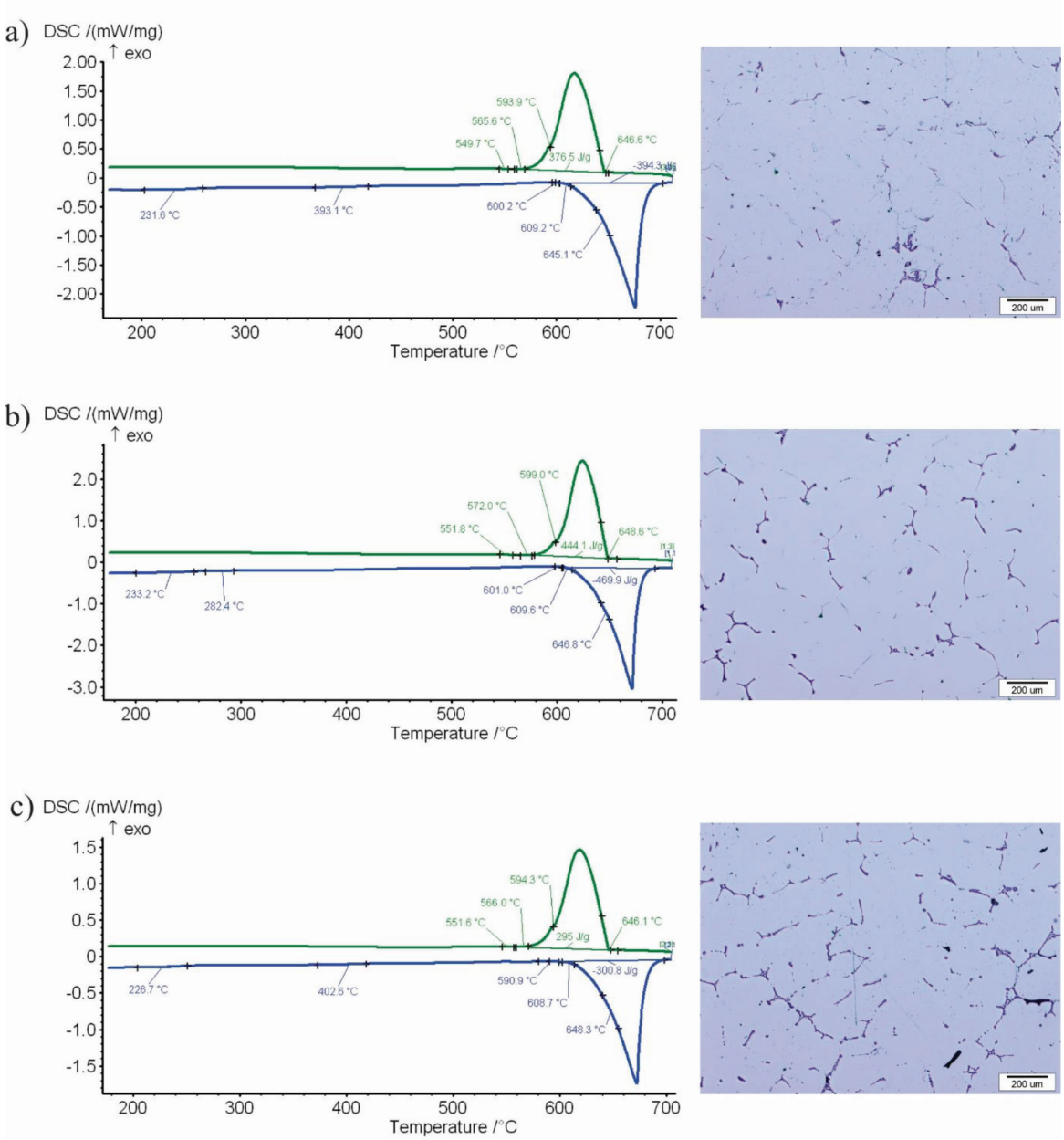

Figure 3: *Heating (blue) and cooling (green) DSC curves of the samples 6008_centre (a), 6008_D/4 (b) and 6008_edge (c) with marked characteristic temperatures and corresponding microstructure images.*

α-Al crystals is observed. During cooling, at a temperature of 648.6°C, the primary α-Al solidifies; at a temperature of 599.0°C, eutectic α-Al + $Al_{15}Si_2M_4$ and at a temperature of 572°C, eutectic α-Al + Al_8Fe_2Si. At 551.8°C, most likely the Si_2V eutectic phase solidifies (named as $CrSi_2$ in the TC calculation).

Similar transitions are also observed on DSC curves of samples taken from the centre and edge of the cross-section of the rod, except that the temperatures slightly differ (Figure 3a and c). When comparing the curves, distinct differences are observed, which probably suggests an inhomogeneous chemical composition in the cross-section of the rod (Figure 4). This is also confirmed by microstructural images after DSC analysis at various sites. The density of microstructural components is much higher

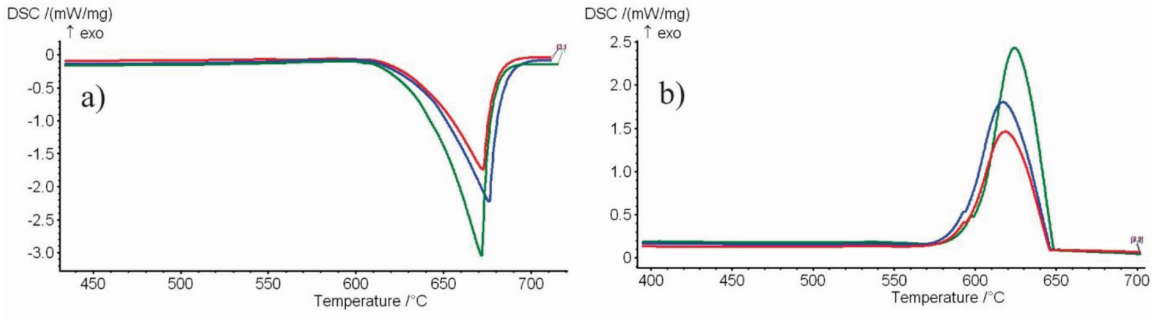

Figure 4: *Comparison of heating (a) and cooling (b) DSC curves of EN AW-6008 alloy from different places of the rod: centre (blue), D/4 (green) and edge (red).*

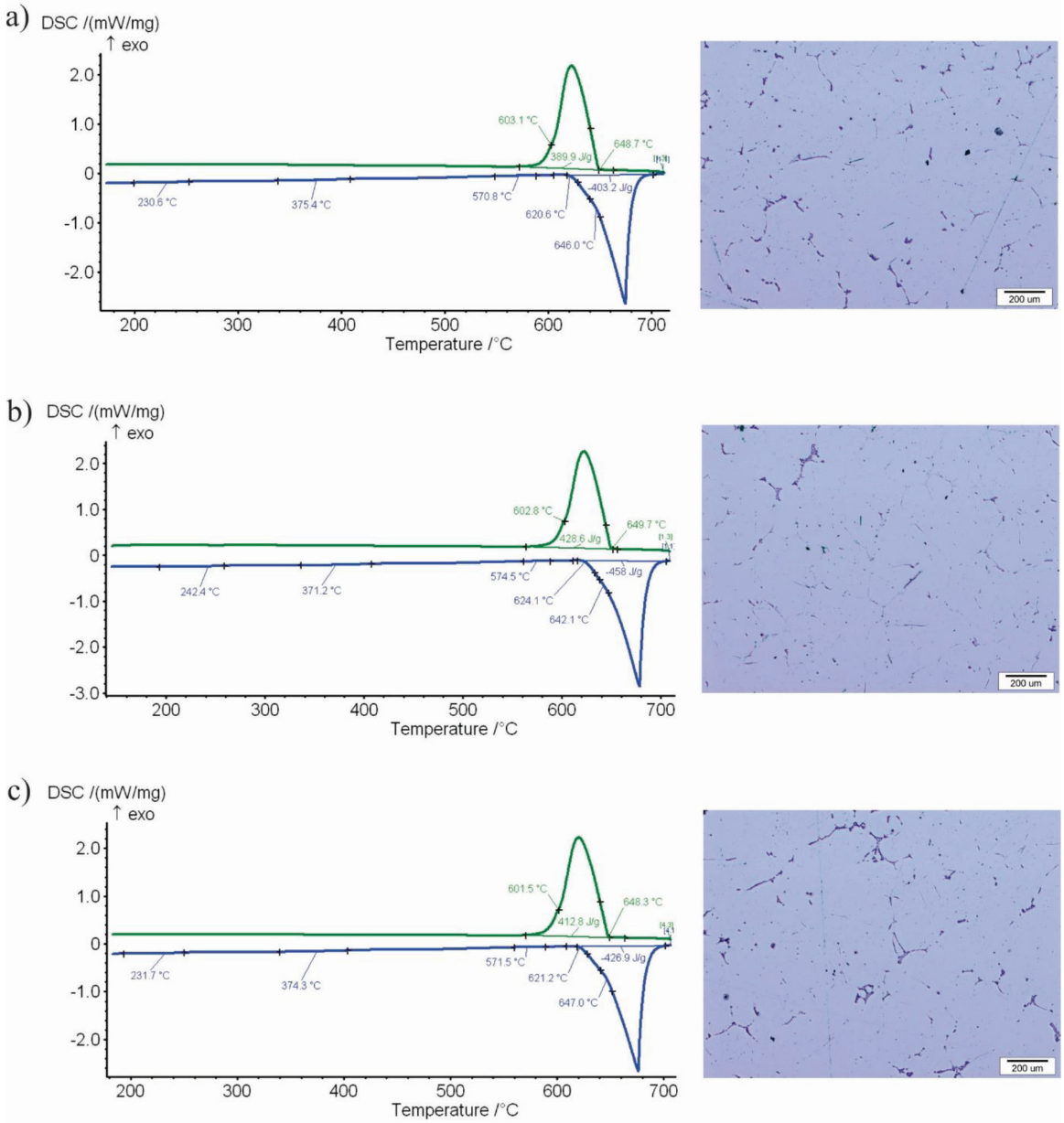

Figure 5: *Heating (blue) and cooling (green) DSC curves of the sample 6060_centre (a), sample 6060_D/4 (b) and sample 6060_edge (c) with marked characteristic temperatures and corresponding microstructure images.*

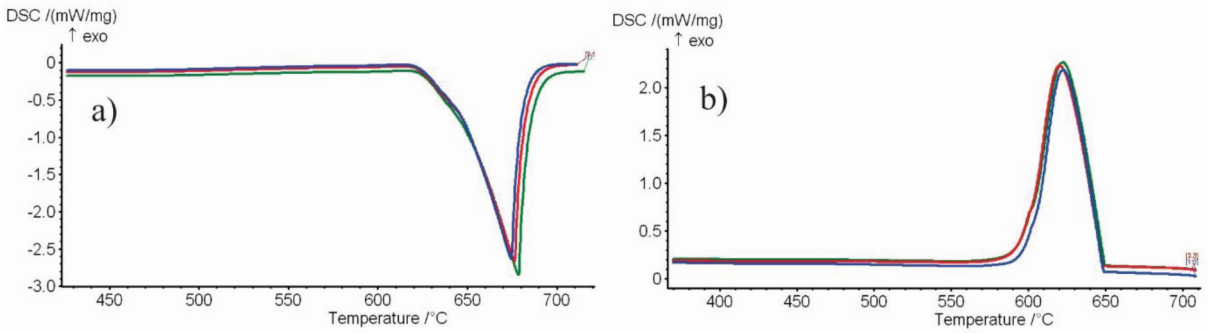

Figure 6: *Comparison of heating (a) and cooling (b) DSC curves of EN AW-6060 alloy from different places of the rod: centre (blue), D/4 (green) and edge (red).*

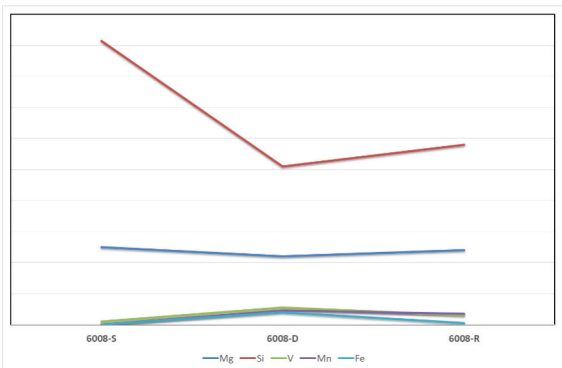

Figure 7: *EDS analysis of samples from the alloy EN AW-6008 taken from the cross-section of the rod at D/4, centre and edge after the DSC analysis.*

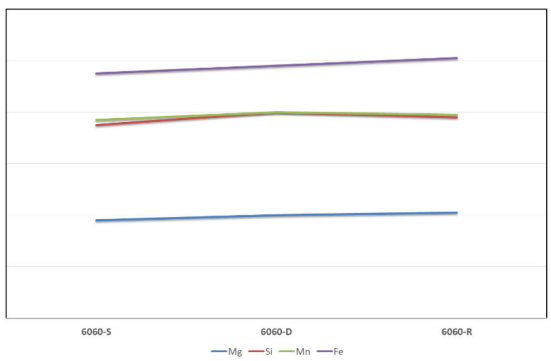

Figure 8: *EDS analysis of samples from the alloy EN AW-6060 taken from the cross-section of the rod at D/4, centre and edge after the DSC analysis.*

in the sample 6008_centre than in the sample 6008_edge, whereas the distribution of microstructure phases is most uniform in the sample 6008_D/4.

Figure 5 shows the heating and cooling DSC curves of samples from the EN AW-6060 alloy taken at three different locations with the accompanying microstructural images. At 574.5°C, the eutectic α-Al + Al_8Fe_2Si begins to melt (according to the Scheil's calculation in Figure 2b), which represents the solidus temperature, and at a temperature of 624.1°C, the eutectic α-Al + $Al_{13}Fe_4$ melts. Furthermore, at 642.1°C, the melting of the primary crystals of α-Al is observed. On the basis of the TC calculations of the equilibrium solidification, it can be concluded that the heating DSC curve leads to the precipitation of the phases $Al_{15}Si_2M_4$ and Mg_2Si at a temperature of 242.4°C and 371.2°C, respectively. During cooling, the primary α-Al (liquidus) solidifies at a temperature of 649.7°C and eutectic with Fe phase ($Al_{13}Fe_4$ or Al_8Fe_2Si) solidifies at a temperature of 602.8°C, depending on the ratio between Fe and Si. Similar changes are also observed on DSC analyses of samples taken from the centre (Figure 5a) and the edge (Figure 5c) of the cross-section of the rod, except that the temperatures differ slightly from one another. When comparing the heating (Figure 6a) and cooling (Figure 6b) of the DSC curves, it is observed that the curves are generally very similar, which indicates better homogeneity of the chemical composition across the cross-section of the rod. The higher homogeneity of the chemical composition and, consequently, of the microstructural components indicated by the results of the DSC analysis was confirmed also by the microstructural images shown next to the corresponding DSC analysis.

Figures 7 and 8 show the results of the EDS analysis on the samples after the DSC experi-

ments confirming the preliminary conclusions; however, only the fluctuation of certain chemical elements is presented since the actual chemical composition of the investigated alloys could not be revealed. It can be seen that the chemical composition is not homogeneous in the cross-section of the cast rod. The largest deviations in the EN AW-6008 alloy are found in a silicon concentration, which varies by more than 0.5 wt.%. Minor deviations are also found in concentrations of magnesium, vanadium, manganese and iron, which can be eliminated by appropriate homogenisation annealing.
Minor fluctuations in the chemical composition are shown by EDS analysis of the alloy EN AW-6060 (Figure 8), which was assumed already after the DSC analysis, where the DSC curves are very similar. The concentrations of magnesium, silicon, manganese and iron are slightly increased from the centre to the edge. EN AW-6060 alloy rods are fairly homogeneous in chemical composition already in the cast state.

Conclusion

The aim of this investigation was analysis of chemical composition homogeneity in the cross-sections of the rods produced from alloys of the 6xxx group. DSC analysis indicated non-homogeneity of the experimental alloys, whereas four reactions in case of EN AW-6008 alloy and two reactions in case of EN AW-6060 alloy could be expected, which corresponds to the Scheil's non-equilibrium calculations, where larger diffusion coefficients of the elements of silicon and magnesium were taken into account.
On the basis of the results presented earlier, it can be concluded that the alloy EN AW-6060 is already quite homogeneous in the cast state through the cross-section of the rod. The concentration of some elements slightly increases from the centre to the edge.
From the results of the analysis of the cross-section of the rod from the EN AW-6008 alloy, it is evident that the chemical composition is not homogeneous in the cross-section of the cast rod. The greatest deviations are observed in the concentration of silicon, which also fluctuates by more than 0.5 wt.%. Minor deviations are also found in concentrations of magnesium, vanadium, manganese and iron, which can be eliminated by appropriate homogenisation annealing.

Acknowledgements

The work was co-financed by the Republic of Slovenia; the Ministry of Education, Science and Sport and the European Regional Development Fund. The work was carried out in the framework of the project Modelling of thermomechAnical pRocessing of The alumINium alloys for high quality products (MARTIN, Grant No.: C3330-18-952012).

References

[1] Zhong, H., Rometsch, P.A., Cao, L., Estrin, Y. (2016): The influence of Mg/Si ratio and Cu content on the stretch formability of 6xxx aluminium alloys. *Materials Science and Engineering: A*, 651, pp. 688–697.
[2] Mukhopadhyay, P. (2012): Alloy Designation, Processing, and Use of AA5XXX Series Aluminium Alloys. *ISRN* Mettalurgy, 2012, pp. 1–16, doi: 10.5402/2012/165082.
[3] Jakobsen, J.V. (2016): *Microstructure and Mechanical Properties of welded AA6082 Aluminum Alloys.* Master Thesis. Trondheim, 89 p.
[4] Sha, G., O'Reilly, K., Cantor, B., Worth, J., Hamerton, R. (2001): Growth related metastable phase selection in a 6xxx series wrought Al alloy. *Materials Science and Engineering: A*, Elsevier, 304–306, pp. 612–616.
[5] Substances and Technologies [online]. SubsTech [cited 7/28/2012]. Available on: *https://www.google.si/#q=SubsTech.+Classification+of.*
[6] Zhong, H., Rometsch, P.A., Estrin, Y. (2014): Effect of alloy composition and heat treatment on mechanical performance of 6xxx aluminum alloys. *Transactions of Nonferrous Metals Society of China*, 24(7), pp. 2174–2178.
[7] Totten, G.E., Mackenzie, D.S. (2016): *ASM Handbook vol. 4E; Heat Treating of Nonferrous Alloys.* ASM International, pp. 32–37.
[8] Kammer, C. (1999): *Aluminium handbook vol. 1: Fundamentals and Materials*. Aluminium-Zentrale e.V.: Germany, 718 p.

[9] Mackenzie, A.S., Totten, G.E. (2003): *Handbook of Aluminium vol. 1: Physical Metallurgy and processes.* Marcel Dekker, Inc.: New York, 1310 p.
[10] Van Horn, K.R. (1967): *Aluminium vol. 1: Properties, physical metallurgy and phase diagrams*. Metals Park: American Society for Metals, 2521p.
[11] Tohru, A., Gordon Baker, M. (1991): *Handbook, A.S.M. Volume 4, Heat Treating.* ASM International, 1960 p.
[12] Zolotorevsky, V.S., Glazoff, M.V., Belov, N.A. (2007): *Casting aluminium alloys.* Elsevier: Oxford, pp. 184–185.
[13] Lise Dons A. (2001): The Alstruc homogenization model for industrial aluminum alloys. *Journal of light Metals 1,* pp. 133–149.
[14] Gale, W.F., Totemeier T.C. (2004): *Smithells Metals Reference Book*: Eighth Edition, Elsevier.
[15] Hood, G.M. (1969): The Diffusion of Iron in Aluminium. *Chalk River Nuclear Laboratories*, pp. 305–328.
[16] Hood, G.M., Schultz, R.J. (1970): The Diffusion of Manganese in Aluminium. *Chalk River Nuclear Laboratories*, pp. 1479–1489.
[17] Paccagnella, A., Ottaviani, G., Fabbri, P., Ferla, G., Queirolo, G. (1985): Silicon Diffusion in Aluminium. *Thin Solid Films*, 128(3–4), pp. 217–232.

Original scientific paper

Received: Sep 12, 2019
Accepted: Dec 10, 2019
DOI: 10.2478/rmzmag-2019-0017

Review of Studies on Corrosion of Steel by CO_2, Focussed on the Behaviour of API Steel in Geological CO_2 Storage Environment

Pregled korozije jekla s CO_2, osredotočen na obnašanja jekel API v okolju geološkega shranjevanja CO_2

Wilmer Emilio García Moreno[1,*], Gabriela Gonçalves Dias Ponzi[1], Ângelo Abel Machado Pereira Henrique[1], Jairo José de Oliveira Andrade[2]

[1] Graduation Programme in Materials Engineering and Technology, Pontifical Catholic University of Rio Grande do Sul (PGTEMA/PUCRS), Brazil

[2] Pontifical Catholic University of Rio Grande do Sul (PGTEMA/PUCRS), Brazil

* wilgm93@gmail.com

Abstract

The world energy demand has become higher with the growing population, which has translated into an increase in emission of greenhouse gases into the atmosphere. For this reason, CO_2 capture and storage has been undertaken to purify the atmosphere. For storing this CO_2, it is necessary to have wells to inject it (deeper than 800 m); moreover, these wells need to have stability over time, and one of the stability aspects is the protection of steel against corrosion. Considering this aspect, the most common steels (focussed on American Petroleum Institute [API] steels) that can be used in an injector well were studied. The best performance was obtained using a high alloy content of Cr and Ni. Furthermore, the most important parameter analysed when corrosion is studied is the test time, which was modelled to stabilise the corrosion rates. The experiments were undertaken after a general review of different studies that investigated the corrosion of steel when in contact with CO_2 in the vapour phase and under supercritical conditions.

Key words: corrosion rate, API steel, CO_2 phase, Cr–Ni–Mo content

Povzetek

Z naraščanjem števila prebivalcev se povečujejo tudi energetske potrebe, kar se odraža na povečanju emisij toplogrednih plinov v atmosfero. Zaradi tega se z namenom čiščenja ozračja izvaja zajem in skladiščenje CO_2. Za skladiščenje CO_2 so potrebne injekcijske vrtine (globlje od 800 m), ki morajo imeti potrebno časovno stabilnost. Eden od stabilnostnih vidikov je ohranjanje jekla proti korozijskim napadom. Zaradi tega so bile opravljene raziskave najbolj pogostih jekel (osredotočeno na API jekla), ki se jih lahko uporablja v injekcijskih vrtinah. Najboljše rezultate so pokazala jekla z visokim deležem Cr in Ni. Pri raziskavah korozije ima pomembno vlogo čas, zato je bil upoštevan pri modelskih analizah. Članek temelji na splošnem pregledu različnih raziskav, v katerih so se avtorji ukvarjali s korozijo jekla v stiku s CO_2 v pari in v superkritičnih pogojih.

Ključne besede: stopnja korozije, API jeklo, faza CO_2, vsebnost Cr-Ni-Mo

Introduction

The economic growth and increasing population have influenced energy demand, causing the latter's cumulative growth, specifically in terms of the use of fossil fuels as a means to supply this demand. This has had repercussion on the global average greenhouse gas concentrations, having CO_2 as the principal component [1]. The biggest challenge in this context is reduction of CO_2 emissions into the atmosphere, with the alternative use of diverse energy sources, such as natural gas, ethanol, nuclear energy, etc. [1].

To reduce the CO_2 level in the atmosphere, CO_2 capture and storage has been planned and used, this CO_2 being stored, mostly, in depleted oil and gas reservoirs; however, some other places have also been considered, such as saline aquifers and coal seams. Some examples of these projects are RECOPOL (coal seam in Poland), Allison Unit (enhanced coal bed methane in Mexico), Selipner (gas field in Norway), Salah gas (project launched by British Petrochemicals and Statoil in Algeria), Ketzin field (enhanced gas recovery in Germany) and some others [2].

According to the Intergovernmental Panel on Climate Change (IPCC) (2007), to have success in CO_2 storage, capacity, injectivity and confinement are required; therefore, well stability is really important, and due to some leakage, a path could be created through the well. Hence, to guarantee the wellbore integrity, some authors have established a lifetime of 1000 years [4–7]. CO_2 is injected in the supercritical condition (>31 °C and 7.38 MPa and stored deeper than 800 m) [2] and reacts with the steel and cement, bringing about damages. When these wells are not designed for injecting CO_2 [3], cement carbonation, microannulus opening and casing corrosion may possibly occur [4]. The objective of this work is to present a general review of the effect of CO_2 corrosion in different kinds of steels used as casing, aiming to know the best options to guarantee the casing stability.

Mechanism of CO_2 Corrosion

Relation Between Corrosion and Well Integrity

When well stability is talked about, an important topic is corrosion (of either steel or cement). However, in this paper, the focus is on steel corrosion. It is important to mention that every completion in wells requires metallic components (wellhead, Christmas tree, tubing, casing, packer, etc.), which – in most of the cases (not always) – are made of some form of steel that have metallic alloy elements, i.e. chromium [5].

A CO_2 injector well can suffer corrosion in every component, from the wellhead to the downhole completion components and, therefore, to achieve large success in the CO_2 storage project, the wells must bear the highest impact of corrosion [2]; thus, to know how to resist corrosion, it is necessary to know how it attacks.

$CO_2$is stable, inert and non-corrosive as a gas; however, when it is in the presence of water (either in the aqueous or vapour CO_2 phase), dissolution occurs, with subsequent hydration, forming H_2CO_3 (carbonic acid), which is the principal agent attacking steels [6]; the principal corrosion products are $FeCO_3$ (iron carbonate) and Fe_3C (iron carbide) [7] but, to understand this mechanism better, analysing how it proceeds step by step is required.

Chemical Reaction of CO_2 and H_2O

Following Table 1, first the CO_2 is hydrated by dissolving in water, forming carbonic acid (H_2CO_3), which is a weak acid because the CO_2 is partly dissociated in water. As carbonic acid is diprotic, it dissociates in two steps, which is considered the main source of acidity. The resulting pH is a function of the CO_2 partial pressure. In the first dissociation of carbonic acid, the bicarbonate is obtained (HCO_3), which, later on, dissociates into carbonate (CO_3) [6, 8].

Chemical Interaction of Fe with Environment

Knowing how CO_2 reacts in the presence of water, we can see that Fe also reacts with its environment (Table 2). Initially, Fe reacts with carbonic acid, yielding ferrous bicarbonate ($Fe(HCO_3)_2$); after this, the precipitation

Table 1: *Reaction of CO_2 and H_2O.*

Reaction name	Reaction
Carbon dioxide hydration	$CO_2 + H_2O \leftrightarrow H_2CO_3$
Carbonic acid dissociation	$H_2CO_3 \leftrightarrow H^+ + HCO_3^-$
Bicarbonate anion dissociation	$HCO_3^- \leftrightarrow H^+ + CO_3^{2-}$

Table 2: *Reaction of Fe with the environment.*

Reaction name	Reaction
Iron–carbonic acid reaction	$Fe + 2H_2CO_3 \rightarrow Fe^{2+} + 2HCO_3^- + H_2$
Iron–bicarbonate reaction	$Fe^{2+} + 2HCO_3^- \rightarrow Fe(HCO_3)_2$
Iron carbonate precipitation	$Fe(HCO_3)_2 \rightarrow FeCO_3 + CO_2 + H_2O$
	$Fe^{2+} + CO_3^{2-} \rightarrow FeCO_3$

of iron carbonate occurs, in two ways. First, when the concentrations of Fe^{2+} and CO_3^{2-} ions reach the maximum solubility limit, they combine forming iron carbonate ($FeCO_3$), with a consequent increase in pH [9]. Second, when the ferrous bicarbonate dissociates, it forms $FeCO_3 + CO_2 + H_2O$; this water could react with the resultant carbon dioxide, yielding, again, carbonic acid and, in this way, it could result in a cycle of corrosion.

The case when CO_2 and water are present has been explained, but, normally, water can have different kinds of ions, such as Cl^-, Na^+, Ca^+, SO_1^{2-}, etc., which can affect the equilibrium of CO_2 and the resulting pH [6]. On the other hand, the presence of $FeCO_3$ could lead to a reduction in the corrosion rate because it is formed on the steel surface [10]. Moreover, this protective film is dependent on low temperatures and high supersaturation of Fe^{2+} and CO_3^{2-}; however, this protective film could grow without having any protective property, but, when it does have the property, it could reduce the corrosion rate between 5 and 100 times [8]. Adversely, even when the iron carbonate is precipitated, if it is not compacted on the surface, it cannot prevent the corrosion [10]. Therefore, some analyses have been performed, showing that at low temperatures, the $FeCO_3$ film gets dissolved continuously and the corrosion rate increases [11]. The precipitation kinetics of FeS is almost two

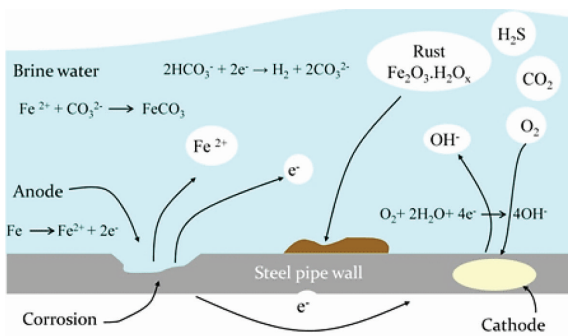

Figure 1: *CO_2 corrosion on a pipe [14].*

orders of magnitude faster than that of $FeCO_3$ at the same conditions [12]; moreover, $FeCO_3$ was formed after 60 days, and even when there was a reduction in corrosion rate, there was still corrosion [13]. In addition, as shown in Figure 1, it is noted that the electrochemical dissociation of iron leads to surface corrosion.

Finally, although the Fe^{2+} ion could react later to form the protective film, this could lead to study the corrosion rate and rate of formation of protective film to know whether $FeCO_3$ is having a positive or negative effect, because as mentioned earlier [11–13], there is still corrosion on steel.

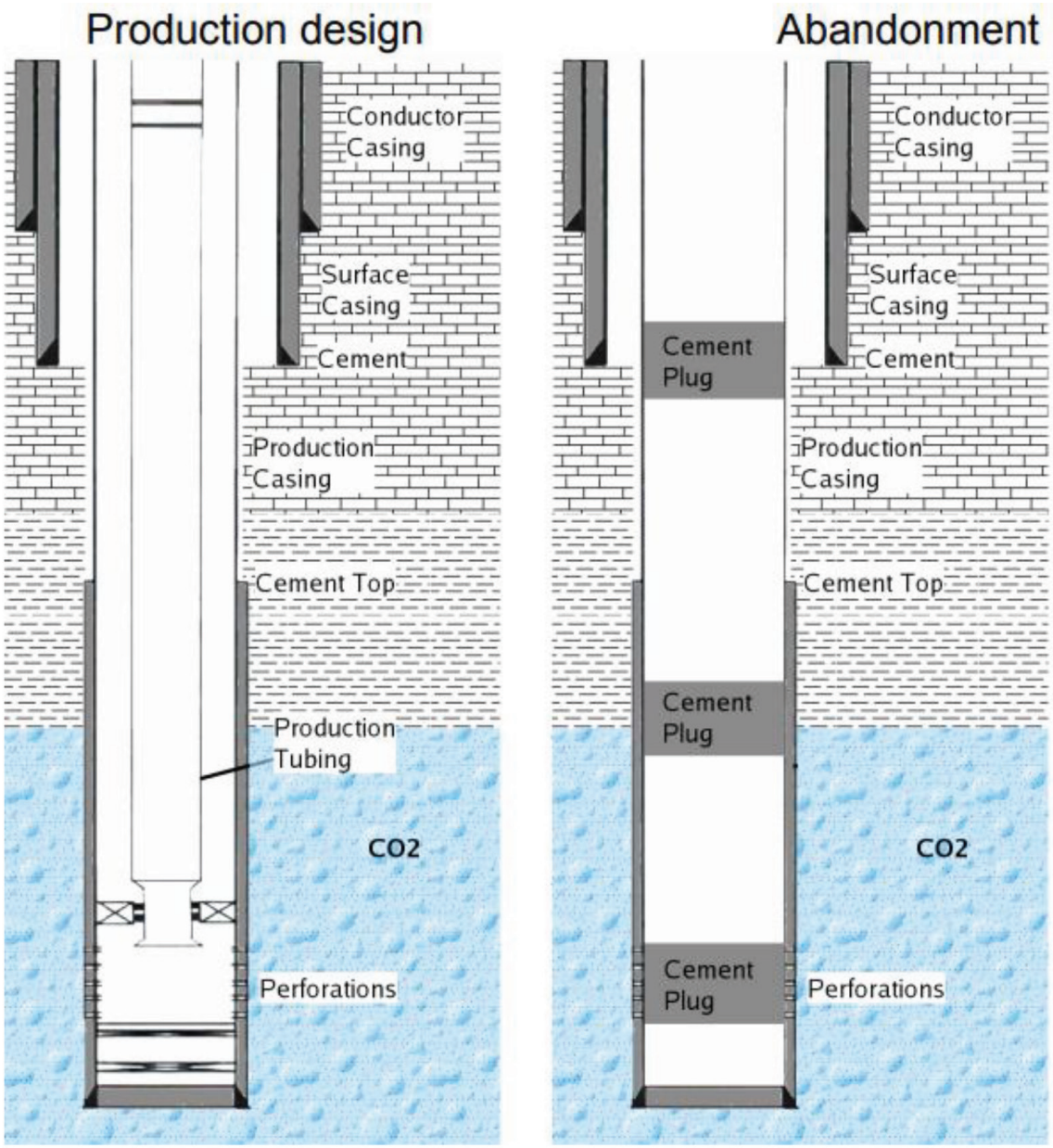

Figure 2: *Well configuration. Taken from [18].*

Different Kinds of Steels

CO_2 can affect the different materials in CO_2 injector wells. Therefore, the metallurgical selection (as well as the type of cement) plays an important role [15] because the casing steel and other parts of the well can be subject to corrosion when they are exposed to CO_2 or formation fluids (or both) (Figure 2). This corrosion can be controlled by using corrosion-resistant alloys (CRAs) [16]. Furthermore, if a CRA is improperly selected, it can lead to mistakes in the future, affecting the performance; hence, taking care of the specific properties of the steels is required because a group of CRAs can be resistant at one temperature; however, this does not guarantee that the CRAs will work with the same performance in a different environment [17].

Casing and tubing play an important role in wells; so, ensuring their integrity is essential. Therefore, the American Petroleum Institute (API) has standardised some grades of steels, which are differentiated by groups, content of

Table 3: *Required chemical composition [21].*

Group	Grade	Type	Chemical composition in mass fraction (%)												
			C		Mn		Mo		Cr		Ni	Cu	P	S	Si
			Min	Max	Min	Max	Min	Max	Min	Max	Max	Max	Max	Max	Max
1	H40	–	–	–	–	–	–	–	–	–	–	–	0.03	0.03	–
	J55	–	–	–	–	–	–	–	–	–	–	–	0.03	0.03	–
	K55	–	–	–	–	–	–	–	–	–	–	–	0.03	0.03	–
	N80	1	–	–	–	–	–	–	–	–	–	–	0.03	0.03	–
	N80	Q	–	–	–	–	–	–	–	–	–	–	0.03	0.03	–
	R95	–	–	0.45	–	1.90	–	–	–	–	–	–	0.03	0.03	0.45
2	M65	–	–	–	–	–	–	–	–	–	–	–	0.03	0.03	–
	L80	1	–	0.43	–	1.90	–	–	–	–	0.25	0.35	0.03	0.03	0.45
	L80	9Cr	–	0.15	0.30	0.60	0.90	1.10	8.00	10.00	0.50	0.25	0.02	0.01	1.00
	L80	13Cr	0.15	0.22	0.25	1.00	–	–	12.00	14.00	0.50	0.25	0.02	0.01	1.00
	C90	1	–	0.35	–	1.20	0.25	0.85	–	1.50	0.99	–	0.02	0.01	–
	T95	1	–	0.35	–	1.20	0.25	0.85	0.40	1.50	0.99	–	0.02	0.01	–
	C110	–	–	0.35	–	1.20	0.25	1.00	0.40	1.50	0.99	–	0.02	0.005	–
3	P110	–	–	–	–	–	–	–	–	–	–	–	0.02	0.03	–
4	Q125	1	–	0.35	–	1.35	–	0.85	–	1.50	0.99	–	0.02	0.01	–

chemical compounds, manufacturing processes and mechanical properties [19], giving the API steel grade; different names are obtained, qualified by a number that represents the minimum yield strength and a letter chosen arbitrarily, without meaning. Therefore, they have been divided into four groups, categorised by resistance to sulphide stress cracking and working pressure [20]:

— Group 1: H-40, J-55, K-55, N-80, R-95;
— Group 2: M-65, L-80, C-90, C-95, T-95, C-110;
— Group 3: P-110;
— Group 4: Q-125.

Furthermore, they can be divided by product specification level (PSL):

— PSL-1: Common application casing (H-40, J-55, K-55, M-65, N-80, R-95);
— PSL-2: Corrosion-resistant casing (L-80, C-90, T-95, C-110);
— PSL-3: Deep well casing (P-110, Q-125).

However, each carbon API steel has the following specific characteristics:

— H40: It is an API steel that is not generally used as tubing, due to its yield strength and the saving in terms of cost is minimum compared to J55 [19],
— J55: This kind of steel is used for most wells if it meets the design criteria. Moreover, when subjected to a CO_2 environment, it is recommended that it is normalised and tempered, as it is used for maximum 9000 ft and 4000 psi in land wells [19].
— N80: It should be either normalised or normalised and tempered [21]. Furthermore, it shows susceptibility to H_2S, and it is recommended for sweet wells [19].
— L80: Tempered at 620 °C, it has 9Cr and 13Cr steels, being anticorrosive in a CO_2 environment; these types should be used at partial pressure of H_2S <1.5 psi [19],
— T95: It is divided into two types, the first one being used in sour facilities [19].
— C110: This C-steel has maximum minimum yield strength. If necessary, the product can be cold-rotated, straightened and subsequently stress-relieved at temperatures between 30 °C and 55 °C below the final specified tempering temperature, or hot-rotated and straightened at temperatures not >165 °C [21].

Table 4: *Required mechanical properties [22].*

Group	Grade	Type	Elongation (%)	Yield strength (MPa)		Minimum tensile strength (MPa)
				Min	Max	
1	H40	–	0.50	276	552	414
	J55	–	0.50	379	552	517
	K55	–	0.50	379	552	655
	N80	1	0.50	552	758	689
	N80	Q	0.50	552	758	689
	R95	–	0.50	655	758	724
2	M65	–	0.50	448	586	586
	L80	1	0.50	552	655	655
	L80	9Cr	0.50	552	655	655
	L80	13Cr	0.50	552	655	655
	C90	1	0.50	621	724	689
	T95	1	0.50	655	758	724
	C110	–	0.70	758	828	793
3	P110	–	0.60	758	965	862
4	Q125	1	0.65	862	1034	931

— P110: This type is restricted to quench-and-tempered heat treatment and is used in deep and sweet wells with high pressures. Even though it has more yielding strength, it is cheaper than C90 and T95 [19].
— Q125: Gag-press straightening or hot-rotating straightening can be performed for straightening, but the temperature at the end of the rotary straightening process should not be <400 °C. However, if this method cannot be used, the product can also be cold-rotated and straightened, but the stress relief must be performed at 510 °C (950 °F) after straightening [21].

These products must comply with the required chemical composition (Table 3), tensile properties and thickness, as presented in Table 4.

Cr-Steel

Onoyama et al. [23] investigated the corrosion resistance of three different compositions of duplex stainless steel. They evaluated the first two in National Association of Corrosion Engineers (NACE) solution at 80 °C for 100 h to get the effect, in percentage, of different compositions of the alloying elements in the steel, finding that it is desirable to reduce the Si percentage (<0.5%), leading to the amount of Ni becoming 10% and increasing the resistance; moreover, Mo and N improve the steel and, Sn and Sb have to be correctly added, neither in excess or nor in lower amount, with the best values being 0.05% Sn and 0.15% Sb. On the other hand, duplex steel was tested in 2.8×10^{-2} mol/L NaCl solution saturated with CO_2 and N_2 at 260 °C for 100 h at 0.10 and 0.05 MPa, obtaining the maximum value around 8.5×10^{-3} mm/yr at 0.10 MPa of pressure and around 3×10^{-3} mm/yr at 0.05 MPa of pressure.

Kimura et al. [24] studied the effect of CO_2 corrosion in 13Cr steel, modifying the chemical composition of Cu, Ni and Mo, at 3 MPa and 180 °C, inside an autoclave with 20% of NaCl solution saturated with CO_2 gas, for 7 days, evaluating the weight loss rate. When there was no addition of Cu, Ni and Mo, the corrosion rate was 1.71 mm/yr, but when these elements were part of the chemical composition, the corrosion rate was <0.3 mm/yr. Moreover, with the increase in Mo content at the same Ni percentage, the corrosion rate decreased. On the other hand, the addition of Cu did not affect the corrosion rate and- the effect of Ni-Cu was not clear.

Another study was carried out by Leth-Olsen [25], which compared carbon-steel, 13Cr and super 13Cr (S13Cr) in a potassium solution with $CO_{2(g)}$ in the liquid and vapour phases, finding an excellent performance of S13Cr, with an average of 0.01 mm/yr, compared to 13Cr, which had a maximum value of 0.7 mm/yr and 0.3 mm/yr (in the liquid phase). Furthermore, the values of maximum corrosion were noted when the dummies were exposed in the liquid phase, the rates of corrosion in the vapour phase being 0.2 mm/yr for carbon-steel and 0.05 mm/yr for 13Cr; no corrosion was seen in S13Cr.

In 2008, the erosion-corrosion of 22Cr steel was analysed, compared with that of an X65 pipeline under the same conditions. This experiment was evaluated using sand grains under three special conditions. First, by varying the temperature from 20 to 70 °C at a sand concentration of 200 ppm and a CO_2 flow of 20 m/s, a constant corrosion rate of around 5 mm/yr was obtained for 22Cr, while X65 showed an increase from 12.25 to 43.5 mm/yr. Second, the solid particle concentration was varied from 30 to 200 ppm, with a temperature of 20 °C and flow velocity of 20 m/s; although having the same tendency, the corrosion rate for 22Cr increased from 0.1 to 2.4 mm/yr approximately, while for X65, it changed from 9 to 12 mm/yr. The last was the variation of velocity from 7 to 20 m/s, maintaining the temperature at 20 °C and concentration of sand particles at 100 ppm; the corrosion rate in 22Cr increased from 0.2 to 0.8 mm/yr, while for X65, it varied from 2.4 to 5.9 mm/yr approximately [26]. Then, it is important to note that an important parameter is considered in this study, namely, the solid particles.

Xu et al. [7] simulated the 3Cr steel used in the well casing in the Huizhou oilfield, with the same formation water composition to get the effect of CO_2 corrosion at different temperatures (45, 65, 85 and 105 °C), measuring every structure in a CO_2 environment, comparing the result in terms of temperature and CO_2 partial pressure (0.5 and 0.2 MPa). They concluded that by increasing the temperature and pressure, it is possible to gain higher corrosion rates. They observed a corrosion rate of 4.5 mm/yr at CO_2 partial pressure of 0.5 MPa and 100 °C; the highest value obtained at CO_2 partial pressure of 0.2 MPa was 1.14 mm/yr at 65 °C and approximately 1 mm/yr at 105 °C.

Group 1 (J-55, K-55, N-80)

Cui et al. [27] evaluated the CO_2 corrosion at supercritical conditions (80 °C and 8.274 MPa) in J55, N80 and P110, at different water cuts (30, 50, 70, 90 and 100%), obtaining an increase in corrosion rate with higher water cut amount. Furthermore, N80 and J55 showed similar behaviour (7 and 4 mm/yr) and, at the same time, were better than P110 (9 mm/yr).

Furthermore, Lin et al. [28] compared the three steels mentioned herein at ion concentrations (g/l) of 19.0 Cl^-, 1.14 SO_4^{2-}, 0.6 HCO_3^-, 1.05 Mg_2^+, 0.39 Ca_2^+, 11.99 Na^+ and 0.12 CO_3^2. First, the pressures (6.89 and 10.34 MPa) were varied at 90 °C; the following values were obtained for the corrosion rate of N80, P110 and J55 steels: 1.752 mm/yr, 2.403 mm/yr, 1.854 mm/yr, 0.922 mm/yr, 1.054 mm/yr and 1.105 mm/yr, respectively. Furthermore, when the pressure was maintained constant (between 1.38 and 2.07 MPa CO_2 partial pressure), the corrosion peak was at 100 °C and, after that, it was lower, the best steels being N80 followed by J55.

Some studies have been carried out to compare J-55 and N-80. One on these studies was by Li et al. [29], who analysed the effect of temperature at 5 MPa of partial pressure and varied the partial pressure at 80 °C over a period of 72 h. Furthermore, these two kinds of steel were compared with carbon steel P110: when pressure is varied, the best result was obtained using J55; however, on varying the temperature, sometimes, the best result was obtained using N80.

When this group of steels is talked about, another important steel item referred to is K55. A study was carried out by Elramady [30], in which a piece was subjected in formation water with CO_2 at 40 psi (0.276 MPa) at ambient temperature, obtaining a rate varying from 0.4 to 0.74 mm/yr. On the other hand, Pehlke [31] used brine, CO_2, H_2S and N at 1000 kPa and 170 °C, obtaining a corrosion rate between 0.188 and 0.243 mm/yr for K55 steel.

Furthermore, when corrosion by CO_2 is studied, there are other acids that can affect the well apart from the carbonic acid. Jingen et al. [32]

analysed the effect of the ratio of CO_2 partial pressure to H_2S partial pressure (10, 100, 200 and 400 MPa) in formation water, for N80 steel, at 90 °C and pCO_2 equal to 0.4 MPa, having a flow rate of 1.7 m/s; they found that when H_2S is not present, the corrosion rate is 1.689 mm/yr, while the ratio is 10; the rate is 0.172 mm/yr, changing to 0.789, 0.621 and 0.511 mm/yr for the subsequent ratios. Additionally, another work studied N80 steel at the same temperature, but at 4 MPa in the present of acetic acid with CO_2 in brine. A value of 0.55 mm/yr was obtained in the absence of the acid, but when solid particle concentration was increased to 1000, 3000 and 5000 ppm, the corrosion rate was 1.25, 3.55 and 4.95 mm/yr approximately [33].

Group 2 (L-80, T-95, C-110)

In this group, one of the most commonly used steels is L80. One of the studies on L80 was by Choi et al. [34], where the temperature was set at 65 and 90 °C and the CO_2 pressures used were 4 MPa (gaseous phase) and 8 and 12 MPa (supercritical phase), in a saline solution of 25% HCl; at 65 °C, the corrosion rate was 8.7, 9.9 and 11 mm/yr, respectively, while at 90 °C, the corrosion rate was 6.1, 3.4 and 4.8 mm/yr, respectively. A similar study was done by Lopes et al. [35], which analysed the steel at 15 and 30 MPa in brine at 50 °C, obtaining 3.534 mm/yr at 15 MPa after 7 days, but 0.375 mm/yr after 30 days and 2.774 mm/yr at 30 MPa after 7 days.

The corrosion process could be affected by other factors, such as sulphur and water. Qiu et al. [36] studied corrosion at three temperatures – 60, 90 and 150 °C – and 0.1 MPa of H_2S partial pressure and 0.5 MPa of CO_2 partial pressure, varying the sulphur content (2 and 4%) and the water content (30 and 70%); the results are shown in Table 5. When the chromium composition of this steel is varied, the corrosion rate changes too, and an example of this is the work by da Silva [37], which used three different CO_2 partial pressures (0.1, 0.3 and 0.65 MPa) at 20 °C with 2, 3 and 5% of NaCl for 72 h, having 0.82% of Cr in twocoupons of L-80 steel (Table 6).

Two other steels in this group are T95 and C110, which were investigated by Elgaddafi [38], where they varied the H_2S concen-

Table 5: *Corrosion rates [36].*

T (°C)	P_{H2S} (MPa)	P_{CO2} (MPa)	Cl^- (g/l)	S (%)	H_2O (%)	Rate (mm/yr)
60	0.1	0.5	0.13	2	30	1.56
90	0.1	0.5	0.13	2	30	1.06
150	0.1	0.5	0.13	2	30	1.39
60	0.1	0.5	0.13	4	30	1.47
90	0.1	0.5	0.13	4	30	0.78
150	0.1	0.5	0.13	4	30	2.08
60	0.1	0.5	0.13	2	60	1.15
90	0.1	0.5	0.13	2	60	0.94
150	0.1	0.5	0.13	2	60	0.98
60	0.1	0.5	0.13	4	60	1.10
90	0.1	0.5	0.13	4	60	0.68
150	0.1	0.5	0.13	4	60	1.00

Table 6: *Corrosion rates [37].*

P (bar)	NaCl (%)	Rate (mm/yr)	
		CQ1	CQ2
1.0	2	0.56	0.49
	3	0.45	0.52
	5	8.89	0.29
3.0	2	1.29	0.71
	3	1.26	0.80
	5	1.13	0.82
6.5	2	1.66	1.11
	3	1.57	0.96
	5	1.61	0.92

tration (0, 10, 50 and 150 ppm) at 38 °C and 41.37 MPa; for T95, the CO_2 corrosion rate was 15, 20, 17 and 17.5 mm/yr, while for C110, the values were 13, 14.5 and 9 mm/yr (there was no test for 150 ppm of H_2S).

Groups 3 and 4 (P-110, Q-125)

The last two groups contain only two steels, which are used for deep well casing. Regarding the studies on P110, the first corresponds to analysis at 100 and 160 °C with a pressure of 4 MPa in a brine solution for 120 h, obtaining a marked contrast in corrosion rate, with values of 6.1843 and 0.8754 mm/yr [39]. Similarly, Guan [40] – at 90 °C and 4 MPa – obtained a corrosion rate around 0.8261 mm/yr; at 110 °C with the same pressure, the rate was 0.2489 mm/yr. On the other hand, if the pressure was varied (0.1, 2, 4 and 6 MPa), maintaining the same temperature (100 °C) for 168 h, the results were 0.64, 0.76, 0.91 and 0.83 mm/yr, respectively [41].

The other steel is Q125. This steel was studied in a CO_2 environment, in a brine solution simulated from the Jinlin Oil Field at 1 MPa and 30 °C and a flow of 1 m/s having a corrosion rate of 1.012 mm/yr [42]. Furthermore, varying the temperature (30, 60, 90 and 120 °C) and keeping the pressure at 2 MPa, using formation water from an oilfield, the values obtained were 0.9, 2.8, 3.6 and 2.4 mm/yr [43]. Giving continuity to the investigation from Elgaddafi [38], increasing the H_2S concentration, the corrosion rates were approximately 3.2, 9.5, 10 and 10 mm/yr.

Analysis of CO_2 Corrosion Studies

In this section, the corrosion rates in different kinds of API steels obtained by different studies are analysed. The principal objective was gathering not only the corrosion rate but also data on the chemical composition of chromium, nickel and molybdenum, pressure, temperature, duration of experiment, the phase of CO_2 and the kind of steel. Every detail was collected and summarised in the Appendix.

Dependency of Corrosion Rates on the Test Time

The different values of corrosion rates indicate that corrosion could be dependent on the test time. Hence, these values were plotted against the days on linear (Figure 3) and semi-log (Figure 4) scales to get better information. There is

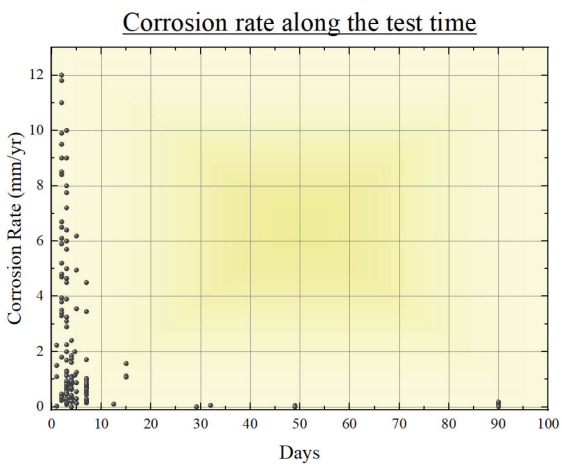

Figure 3: *Corrosion rate against time on a linear scale.*

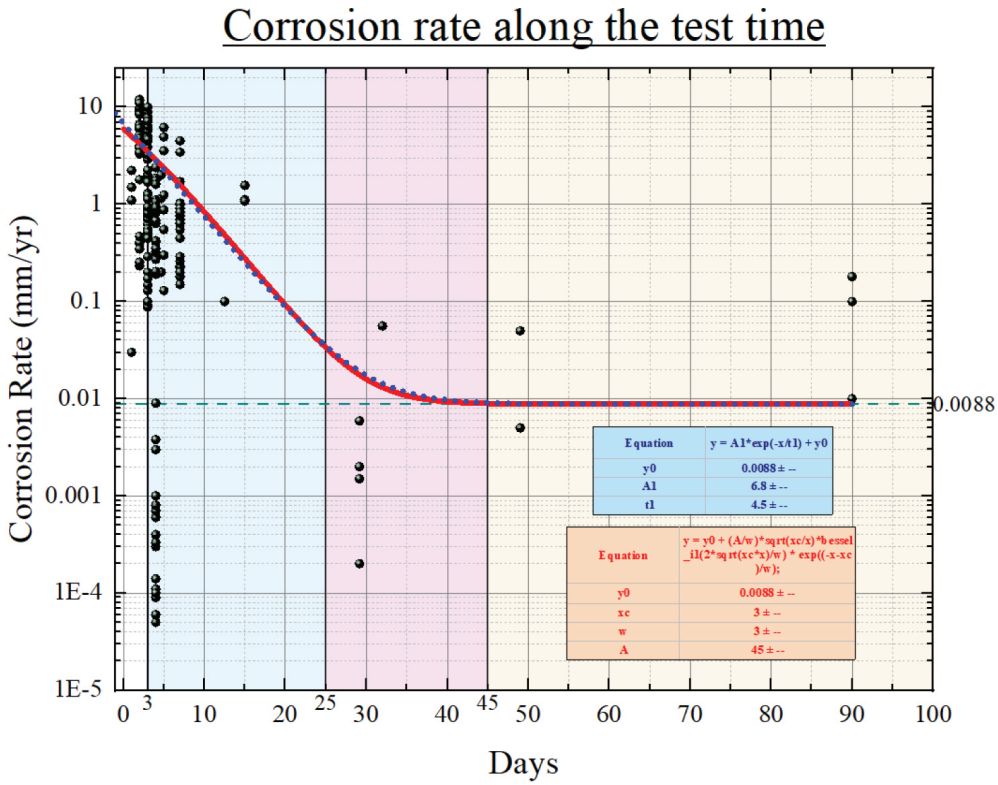

Figure 4: *Corrosion rate against time on a semi-log scale.*

a clear tendency versus the time in the graphs; in Figure 4, four regions were identified:

- From 0 to 3 days, which could be fast growth in corrosion rate, which could be produced by the formation of $FeCO_3$ film.
- From 3 to 25 days, in which there is a continuous reduction of the corrosion rate.
- From 25 to 45 days, stabilisation of the corrosion rates is initiated, with observation of exponentially reducing rates.
- From 45 days onwards, the rates of corrosion are stabilised; there is a plateau, with a corrosion rate of 0.008 mm/yr; however, this value is only an approximation.

With the already-identified four zones of the corrosion mechanism, the tendency was modelled, yielding two curves; the first equation shows a slightly better fit in the initial region, and the second equation is the best simplified tendency approximation along time (blue dotted curve).

$$y = 0.0088 + \frac{45}{3}\sqrt{\frac{3}{\text{time}}}\left(\frac{2\sqrt{x_0\,\text{time}}}{3}\right)e^{\frac{-\text{time}-x_0}{3}} \quad (1)\text{: } \textit{Better curve fit}$$

$$y = 0.0088 + 6.8e^{-\frac{\text{time}}{4.5}} \quad (2)\text{: } \textit{The best simplified curve approximation}$$

Stabilised Corrosion Rates

To analyse the long-term corrosion rates, these have to be in their plateau; it means, they have to be stabilised. Therefore, every rate with a test time below 45 days was stabilised by the mean of the tendency in Eq. (2) (because it is simpler and well fitted). Furthermore, they were separated by the CO_2 phase (vapour and supercrit-

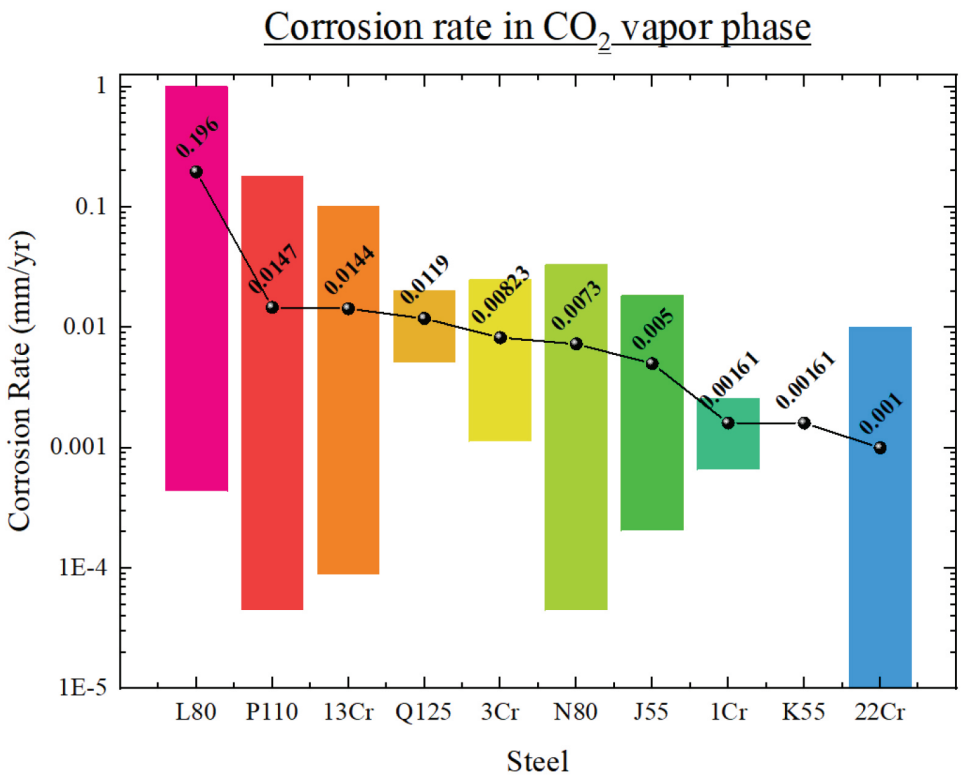

Figure 5: *Stabilised corrosion rates for different kinds of steels in the CO_2 vapour phase.*

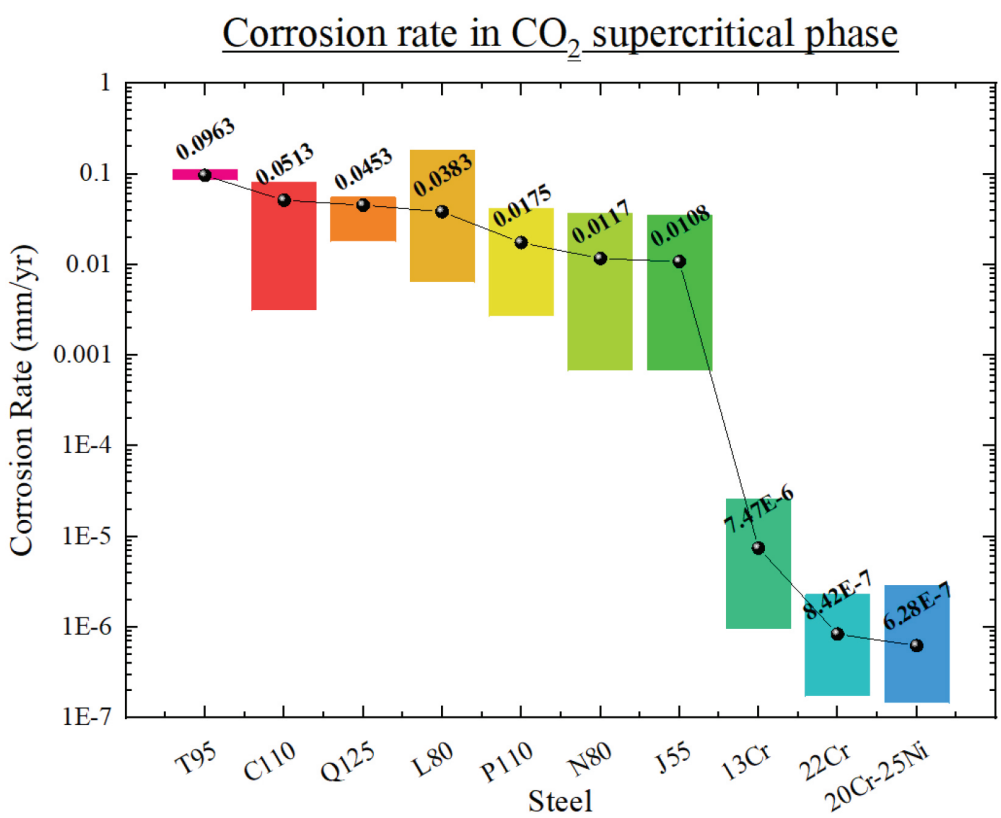

Figure 6: *Stabilised corrosion rates for different kinds of steels in the CO_2 supercritical phase.*

Table 7: *Classification of corrosion rates by steels.*

Category	Steels in CO_2 vapour phase	Steels in CO_2 supercritical phase
Low	P110, 13Cr, Q125, 3Cr, N80, J55, 1Cr, K55 and 22Cr	P110, N80, J55, 13Cr, 22Cr and 20Cr-25Ni
Moderate	–	T95, C110, Q125 and L80
High	L80	–

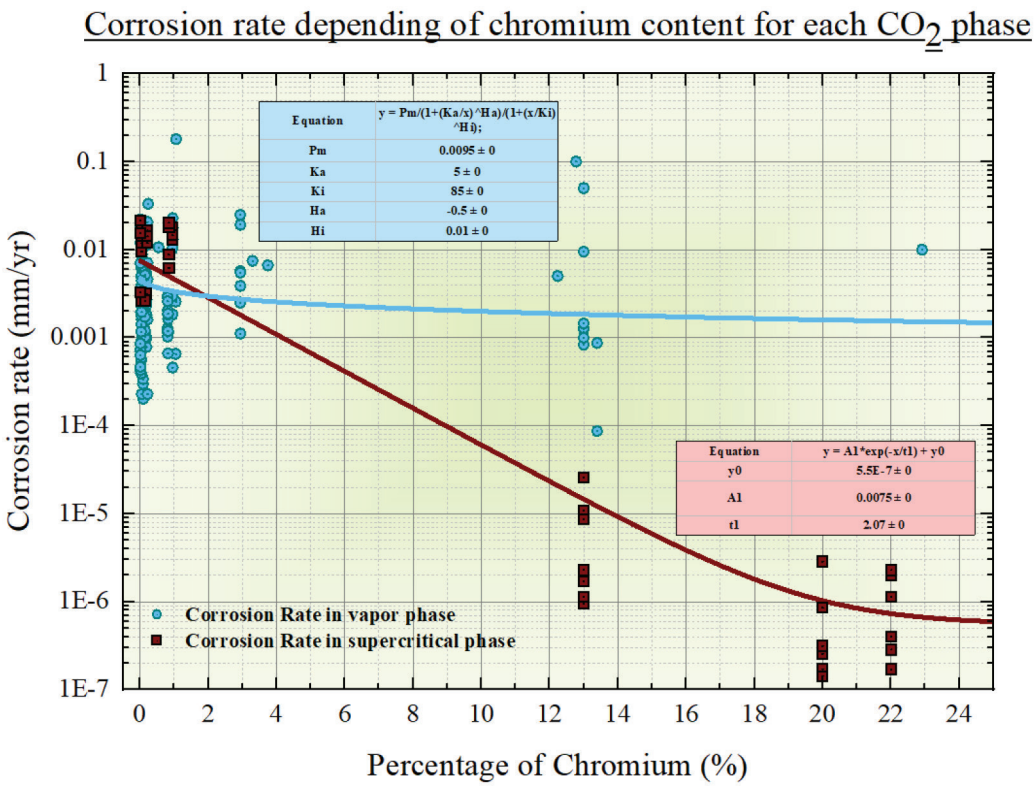

Figure 7: *Effect of chromium content in steels, for each CO_2 phase.*

ical). Then, to conclude the results observed in both graphs (Figures 5 and 6), it is necessary to refer to the NACE corrosion category, which defines the corrosion rate as low if the value is <0.025 mm/yr, moderate if it ranges between 0.025 and 0.15 mm/yr and high if the value is from 0.16 to 0.25 mm/yr. Thus, the steels could be classified as in Table 7, and in general, the corrosion rate is lower in the supercritical condition, which is the phase of CO_2 when it is injected, and higher in the vapour when it goes through the cement paste.

Effect of Chemical Composition of Steels

Addition of chemicals to form steel alloys permit better response against corrosion, especially when chromium is added (it forms stainless steel) and, furthermore, the quantity of nickel and molybdenum could help to prevent CO_2 corrosion. The effect of these elements when they are added to steels was analysed (Figures 7–9). There is a clear effect of chromium as a corrosion-protective element. Only its presence in steel reduces corrosion significantly, and at a percentage >20%, it presents a plateau but has a very low corrosion rate. When nickel is added, the rate reduces faster, helping the chro-

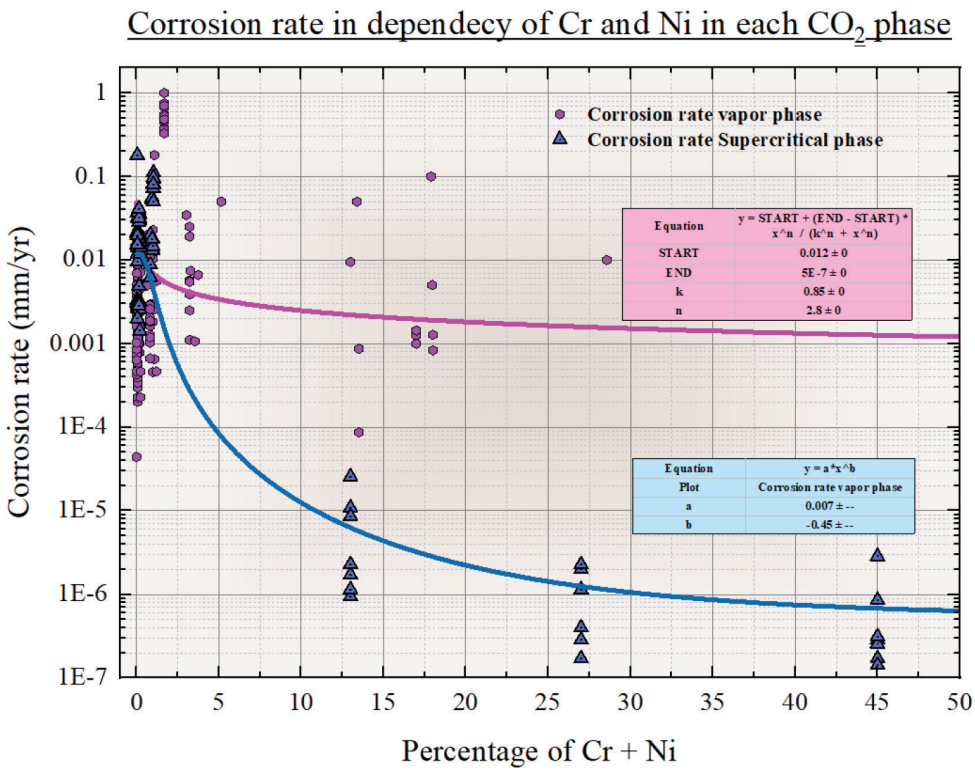

Figure 8: *Effect of chromium and nickel content in steels, for each CO_2 phase.*

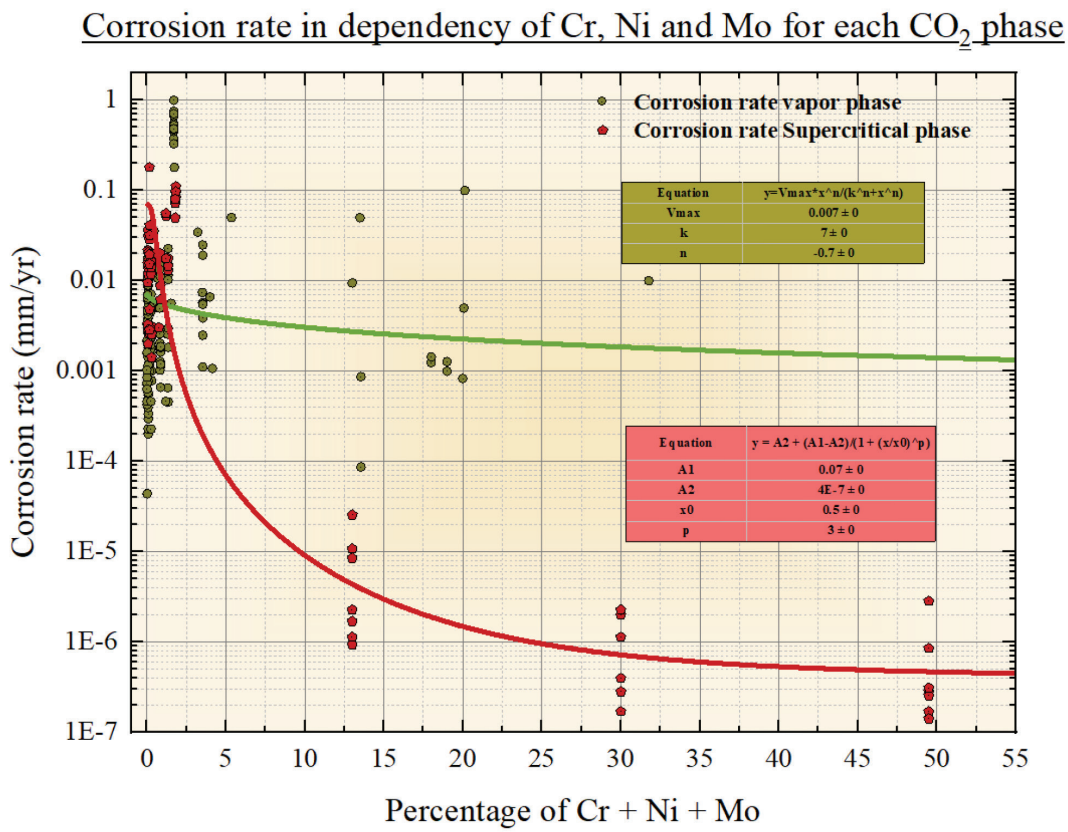

Figure 9: *Effect of chromium, nickel and molybdenum content in steels, for each CO_2 phase.*

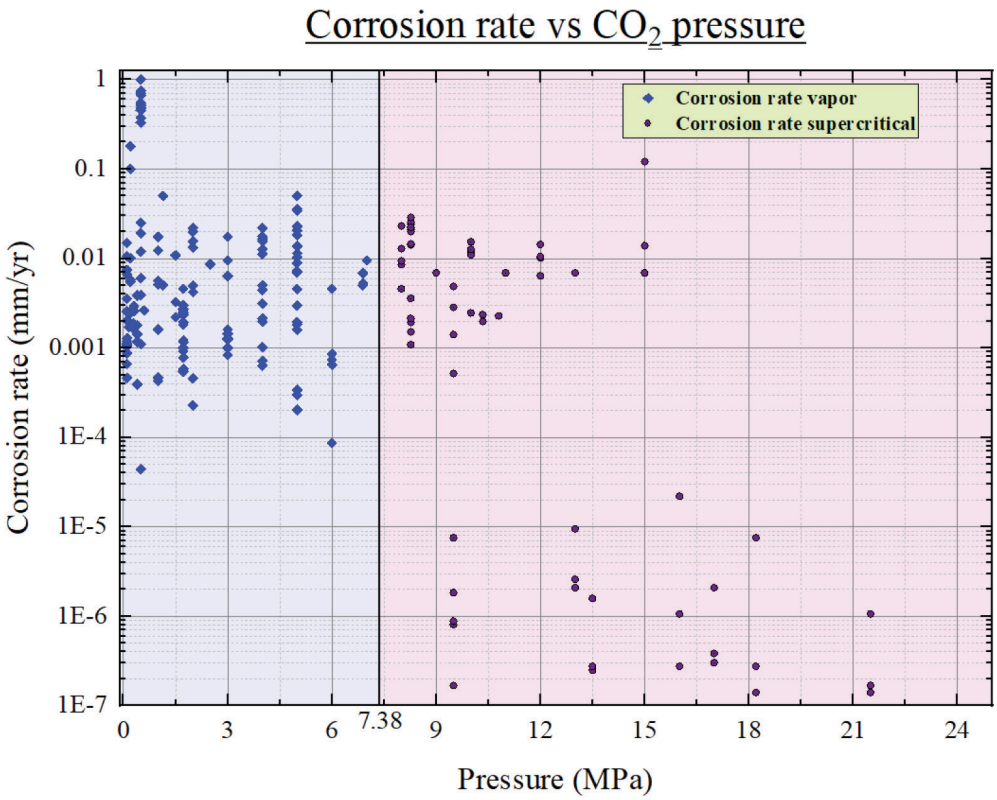

Figure 10: *Corrosion rate against the pressure.*

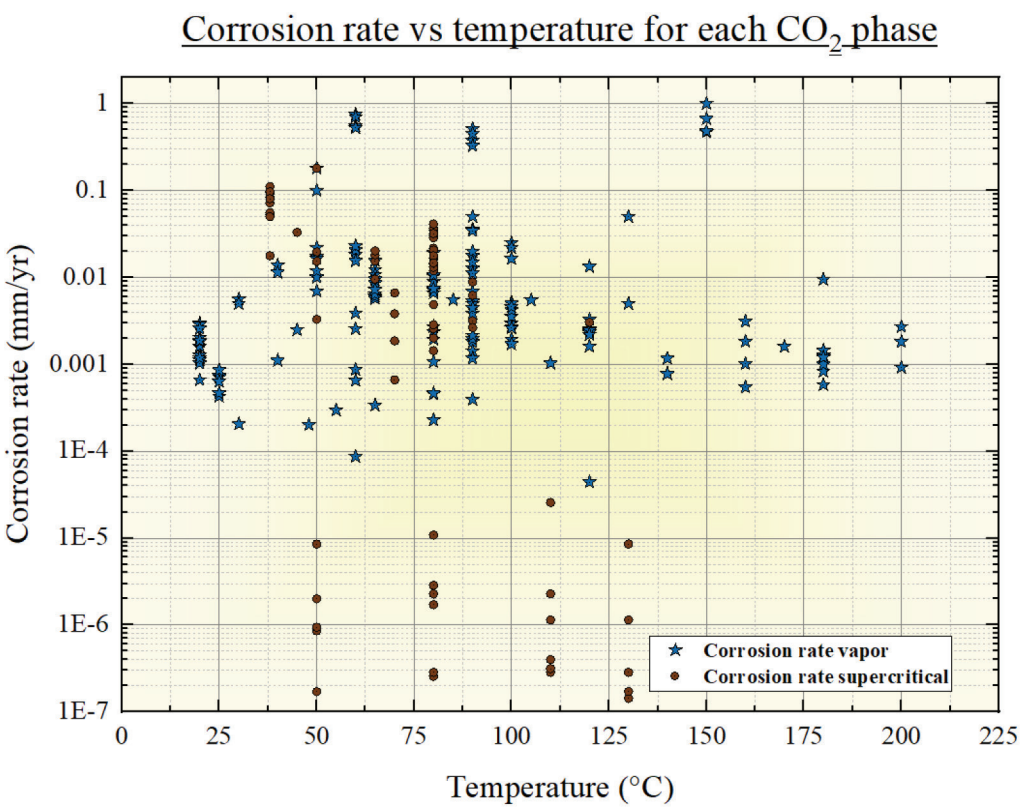

Figure 11: *Corrosion rate versus the temperature.*

mium as a protective element; however, the molybdenum has no significant effect, showing the same tendency as when it is not added. This is in the supercritical condition, because when the vapour phase is observed, the effect is not as high as in the supercritical condition.

Effect of Pressure and Temperature

Studying the effect of these two factors is difficult, because the idea is to analyse by varying one of them and maintaining the other one constant; to observe the effect, however, it was decided to graphically represent them as separate parameters (Figures 10 and 11). Then, varying the pressure (>7.38 MPa is supercritical condition), the lowest corrosion rates are found in the supercritical conditions, and as the pressure becomes higher, lower rates are obtained. However, when the temperature is evaluated, it is difficult to get a tendency probably because different values of pressure could be studied at one temperature.

Conclusion

It is known that different factors could affect the corrosion rates. First, the time of tests has to be considered because a test spreading over 3 days should not be used for determining awell's stability in CO_2–rich conditions, because, as earlier mentioned, for a warranty of stability for >100 years, the corrosion rates must be the lowest as possible. On the other hand, the wall thickness is a factor to be considered in the front side corrosion rates, because the walls could be as thick as 12 mm to >25 mm. Thus, a corrosion rate of 0.06 mm/yr could corrode half the thickness of a wall of 12 mm in 100 years; hence, warrantying the lowest corrosion rates is extremely important and required.

Alternatively, having a steel with high yield strength, such as C110, T95 or P110, is not a warranty for having good corrosion protection, but the chemical elements can help. Furthermore, ensuring good corrosion protection during the injection of CO_2 can have the highest effect on the life of the casing and tubing along the well, because, besides the corrosion, the steel can be affected by erosion due to the flow of CO_2 along the tubing. Additionally, if the well presents good stability along its injection path, the next important section has to be the cement paste stability, which will be the wall between the casing and the stored CO_2. Furthermore, the only steel that presented a relatively worse behaviour was L80, but in the vapour phase of CO_2. Finally, by ensuring a corrosion rate around 0.01 mm/yr, in 1000 years, it will corrode 10 mm; but for this to happen, the CO_2 has to be in contact with the casing. It means an injectivity spanning 1000 years or breaking through the cement paste after storing.

Acknowledgements

First, thanks are due to the Pontifical Catholic University of Rio Grande do Sul (PUCRS) because without the university, this work could not have been completed. Furthermore, we thank CAPES and Petrobras, for the award of scholarships, which let us work at PUCRS.

References

[1] M. Zhang and S. Bachu, "Review of integrity of existing wells in relation to CO2 geological storage: What do we know?," *International Journal of Greenhouse Gas Control,* vol. 5, pp. 826–840, 2011.

[2] M. Bai, Z. Zhang and X. Fu, "A review on well integrity issues for CO2 geological storage and enhanced gas recovery," *Renewable and Sustainable Energy Reviews,* vol. 59, pp. 920–926, 2016.

[3] S. Bachu and T.L. Watson, "Review of failures for wells used for CO2 and acid gas injection in Alberta, Canada," *Energy Procedia,* vol. 1, no. 1, 2009.

[4] S. Asamoto, Y.L. Guen, O. Poupard and B. Capra, "Well integrity assessment for CO2 injection – A numerical case study on thermo-mechanical behavior in downhole CO2 environments," *Engineering Computations,* vol. 30, no. 6, pp. 842–853, 2013.

[5] J. Bellarby, "Material Selection," in *Well Completion Design,* vol. 56, Developments in Petroleum Science, 2009, pp. 433–472.

[6] A. Kahyarian, M. Achour and S. Nešić, "CO2 corrosion of mild steel," in *Trends in Oil and Gas Corrosion Research and Technologies*, Woodhead Publishing Series in Energy, 2017, pp. 149–190.

[7] L. Xu, J. Xu, M.-b. Xu, S.-y. Li, S. Liu, Y. Huang and F.-c. You, "Corrosion Behavior of 3% Cr Casing Steel in CO2-Containing Environment: A Case Study," *The Open Petroleum Engineering Journal,* vol. 11, pp. 1–13, 2018.

[8] A. Dugstad, "Fundamental Aspects of CO2 Metal Loss Corrosion – Part I: Mechanism," 2006.

[9] M. Nordsveen, S. Nešić, R. Nyborg and A. Stangeland, "A Mechanistic Model for Carbon Dioxide Corrosion of Mild Steel in the Presence of Protective Iron Carbonate Films—Part 1: Theory and Verification," *Corrosion,* vol. 59, no. 5, pp. 443–456, 2003.

[10] T. Li, Y. Yang, K. Gao and M. Lu, "Mechanism of protective film formation during CO2 corrosion of X65 pipeline steel," *Journal of University of Science and Technology Beijing,* vol. 15, no. 6, 2008.

[11] J. Hernandez, A. Muñoz and J. Genesca, "Formation of iron-carbonate scale-layer and corrosion mechanism of API X70 pipeline steel in carbon dioxide-saturated 3% sodium chloride," *Afinidad IQS,* vol. 69, 2012.

[12] Z. Ma, Y. Yang, B. Brown, S. Nesic and M. Singer, "Investigation of FeCO3 and FeS Precipitation Kinetics by EQCM," in *NACE International 2018*, 2018.

[13] T. Berntsen, M. Seiersten and T. Hemmingsen, "Effect of FeCO3 Supersaturation and Carbide Exposure on the CO2 Corrosion Rate of Carbon Steel," *Corrosion Sciences,* vol. 69, no. 6, 2013.

[14] S. Ibrahim, "isalama," [Online]. Available: https://isalama.wordpress.com/article/corrosion-inhibitors-in-the-oilfield-3uf3kbfllnswt-4/. [Accessed 7 December 2019].

[15] M. Haigh, "Well Design Differentiators for CO2 Sequestration in Depleted Reservoirs," *Society of Petroleum Engineers,* 2009.

[16] T. Syed and T. Cutler, "Well Integrity Technical and Regulatory Considerations for CO2 Injection Wells," *Society of Petroleum Engineers,* 2010.

[17] B.D. Craig and L. Smith, Corrosion Resistant Alloys (CRAs) in the oil and gas industry, Nickel Institute, 2011.

[18] B. Carey, "IEA Greenhouse Gas," [Online]. Available: https://ieaghg.org/docs/General_Docs/Summer_School/CAREY%20Wellbore%20Integrity_Tues_secured.pdf. [Accessed 12 December 2019].

[19] Equip Outlet Inc, "API Steel Grade Category and Color," 2017. [Online]. Available: http://www.equipoutlet.com/api-steel-grade-category.html. [Accessed 28 April 2019].

[20] OEA Consulting, "The API Casing Steel Grades... How Are They Defined?," OEA Consulting, 2018. [Online]. Available: https://www.oea-consulting.ca/our-blog/13-the-api-casing-steel-grades-how-are-they-defined. [Accessed 28 April 2019].

[21] OCTAL Steel, "API 5CT Casing and Tubing Specification," OCTAL Steel, 31 January 2019. [Online]. Available: https://www.octalsteel.com/api-5ct-specification. [Accessed 28 April 2019].

[22] API, "API Specification 5CT 9th Edition," API, 2011.

[23] M. Onoyama, N. Hayashi, K. Shitani and T. Suehiro, "Evaluation of Corrosion Resistance of a Duplex Stainless Steel in H2S-CO2-Chloride Environments," *Material for energy systems,* vol. 5, no. 2, 1983.

[24] M. Kimura, Y. Miyata, Y. Yamane, T. Toyooka, Y. Nakano and F. Murase, "Corrosion Resistance of High-Strength Modified 13% Cr Steel," *Corrosion Science,* 1999.

[25] H. Leth-Olsen, "CO2 Corrosion of Steel in Formate Brines for Well Applications," in *Corrosion 2004*, 2004.

[26] X. Hu and A. Neville, "Erosion-corrosion of Pipeline Steel X65 and 22Cr Duplex Stainless Steel in CO2 Saturated Environment," in *SPE International Oilfield Corrosion Conference*, Aberdeen, 2008.

[27] Z. Cui, S. Wu, C. Li, S. Zhu and X. Yang, "Corrosion behavior of oil tube steels under conditions of multiphase flow saturated with super-critical carbon dioxide," *Materials Letters,* vol. 58, no. 6, pp. 1035–1040, 2004.

[28] G. Lin, M. Zheng, Z. Bai and X. Zhao, "Effect of Temperature and Pressure on the Morphology of Carbon Dioxide Corrosion Scales," *Corrosion Science,* vol. 62, no. 6, June 2006.

[29] N. Li, D. Xu, W. Ma, P. Ma and J. Li, "CO2 Corrosion Behaviors of Tubing and Casing Steels in Simulation Produced Water for Deep Natural Gas Wells," in *5th International Conference on Advanced Engineering Materials and Technology (AEMT 2015)*, 2015.

[30] A.G. Elramady, "The Effect of various deformation processes on the corrosion behavior of casing and tubing carbon steels in sweet environment," 2015.

[31] T. Pehlke, "Studies of Aqueous Hydrogen Sulfide Corrosion in Producing SAGD Wells," University of Calgary, Calgary, 2017.

[32] D. Jingen, Y. Wei, L. Xiaorong and D. Xiaoqin, "Influence of H2S Content on CO2 Corrosion Behaviors of N80 Tubing Steel," *Petroleum Science and Technology,* pp. 1387–1396, 2011.

[33] S. Zh, A. Fu, J. Miao, Z. Yin and J. Wei, "Corrosion of N80 carbon steel in oil field formation water containing CO2 in the absence and presence of acetic acid," *Corrosion Science,* vol. 53, no. 53, pp. 3156–3165, 2011.

[34] Y.-S. Choi, F. Farelas, S. Nešić, A.A.O. Magalhães and C. d. A. Andrade, "Corrosion Behavior of Deep Water Oil Production Tubing Material Under Supercritical CO2 Environment: Part 1—Effect of Pressure and Temperature," *Corrosion Science,* vol. 70, no. 1, pp. 38–47, 2014.

[35] N.F. Lopes, E.M. da Costa and J.S. Fernandes, "Desempenho do aço API L80 frente à corrosão por CO2 em meio similar ao pré-sal," in *22º CBECiMat - Congresso Brasileiro de Engenharia e Ciência dos Materiais*, Natal, 2016.

[36] Z. Qiu, C. Xiong, R. Yi and Z. Ye, "Corrosion Behavior of L80Steel in Different Temperature and Sulfur Content," *IOP Conference Series: Materials Science and Engineering,* 2017.

[37] P. da Silva Neto, "Desenvolvimento de Tubo de Aço API 5CT Grau L80 com 1% Cromo Soldado por ERW/HFIW," UFRJ, Rio de Janeiro, 2016.

[38] R. Elgaddafi, R. Ahmed and S. Shah, "Modeling and experimental studies on CO2-H2S corrosion of API carbon steels under high-pressure," *Journal of Petroleum Science and Engineering,* vol. 156, pp. 682–696, 2017.

[39] Z. Yin, W. Zhao, Z. Bai and Y. Feng, "Characteristics of CO2 corrosion scale formed on P110 steel in simulant solution with saturated CO2," *Surface and Interface Analysis,* vol. 40, no. 9, pp. 1231–1236, 2008.

[40] Z. Guan, Y. Ren, Z. Cui, J. Zhang and M. Du, "Evaluation of Corrosion Inhibitors for P110 Steel in Simulated Oilfield Produced Waters Using EFM and CMAS Techniques," *Corrosion Science and Protetion Technology,* vol. 28, no. 2, pp. 139–143, 2016.

[41] J. Li, H. Ma, S. Zhu, C. Qü and Z. Yin, "Erosion resistance of CO2 corrosion scales formed on API P110 carbon steel," *Corrosion Science,* vol. 86, pp. 101–107, 2014.

[42] L. Wang, F. Liu, Q. Zhao and H.-b. Wu, "CO2 Corrosion and Grooving Corrosion Behavior of the ERW Joint of the Q125 Grade Tube Steel," *Journal of Iron and Steel Research, International,* vol. 22, no. 10, pp. 943–948, 1015.

[43] D. Tang, L. Wang, H. Wu and i. Liang, "Mechanical Properties and CO2 Corrosion Behavior of Q125 Grade Oil Tube Steel Used in Deep Oil Well," *Advanced Materials Research,* Vols. 524–527, pp. 1471–1479, 2012.

[44] Y. Zhang, K. Gao and G. Schmitt, "Water Effect On Steel Under Supercritical CO2 Condition," in *Corrosion Conference 2011*, Texas, 2011.

[45] A. Pfennig and R. Bäßler, "Effect of CO2 on the stability of steels with 1% and 13% Cr in saline water," *Corrosion Science,* vol. 51, pp. 931–940, 2009.

[46] W. Yan, P. Zhu and J. Deng, "Corrosion behaviors of SMSS 13Cr and DSS 22Cr in H2S/CO2-oil-water environment," *International journal of electrochemical science,* vol. 11, no. 11, pp. 9542–9558, 2016.

[47] S. Azuma, H. Kato, Y. Yamashita, K. Miyashiro and S. Saito, "The Long-term Corrosion Behaviour of Abandoned Wells Under CO2 Geological Storage Conditions: (2) Experimental Results for Corrosion of Casing Steel," *Energy Procedia,* vol. 37, pp. 5793–5803, 2013.

[48] H. Bai, Y. Wang, Y. Ma, Q. Zhang and N. Zhang, "Effect of CO2 Partial Pressure on the Corrosion Behavior of J55 Carbon Steel in 30% Crude Oil/Brine Mixture," *Materials,* vol. 11, no. 9, 2018.

[49] X.Z. Wang, Z.G. Yang, Z.F. Yin, Z.Q. Gao, J.D. Li and K. Wang, "Corrosion investigation of J55 steel under simulated enhanced oil recovery conditions using CO2 flooding," *Corrosion Engineering, Science and Technology,* vol. 49, no. 4, pp. 275–282, 2014.

[50] Y. Ma, Q. Zhang and H. Bai, "N80 Oil Tube Steel Corrosion Behavior in Different CO2 Saturated Brine," *Ekoloji,* no. 106, pp. 113–121, 2018.

[51] H. Li, D. Li, L. Zhang, Y. Bai, Y. Wanga and M. Lua, "Fundamental aspects of the corrosion of N80 steel in a formation water system under high CO2 partial pressure at 100 °C," *RSC Advances,* no. 21, 2019.

[52] M. Escalante, N. Ochoa, C. Sequera and J. Jaspe, "Evaluación de la resistencia a la corrosión por CO2 de nuevos aceros de bajo cromo utilizados en tubulares de pozo mediante tecnicas electroquímicas," *Revista Latinoamericana Met. Mat,* vol. 34, no. 1, 2014.

[53] X. Zhang, J.F. Zevenbergen and T. Benedictus, "Corrosion Studies on Casing Steel in CO2 Storage Environments," *Energy Procedia,* vol. 37, pp. 5816–5822, 2013.

[54] M.N. Hazman bin Mansor, *Study on C02 Corrosion in Oil Producing Well,* 2009.

[55] L.C. Lozada, *Corrosion performance of L80, L80Cr1% and L80Cr3% steel grades in simulant solution with carbon dioxide and scaling,* Manchester, 2015.

[56] C. Ren, D. Zeng, J. Lin, T. Shi and W. Chen, "Sour Corrosion of C110 Steel and Its Influence by Galvanic Couple and Stress," *Industrial and Engineering Chemistry Research,* vol. 51, no. 13, p. 4894–4904, 2012.

[57] J. Sun, C. Sun, X. Lin, X. Cheng and H. Liu, "Effect of Chromium on Corrosion Behavior of P110 Steels in

CO2-H2S Environment with High Pressure and High Temperature," *Materials,* vol. 9, no. 3, 2016.

[58] Y.D. Cai, P.C. Guo, D.M. Liu, S.Y. Chen and J.L. Liu, "Comparative study on CO2 corrosion behavior of N80, P110, X52 and 13Cr pipe lines in simulated stratum water," *Science China Technological Sciences,* vol. 53, no. 9, p. 2342–2349, 2010.

[59] R. Xie, Z. Gu, Y. Yao, H. Xu, K. Deng and Y. Liu, "Electrochemical Study on Corrosion Behaviors of P110 Casing Steel in a Carbon Dioxide-Saturated Oilfield Formation Water," *International journal of electrochemical science,* vol. 10, no. 7, pp. 5756–5769, 2015.

[60] IPCC, "Climate Change 2014 Synthesis Report Summary for Policymakers," 2014.

[61] B.G. Kutchko, B.R. Strazisar, D.A. Dzombak, G.V. Lowry and N. Thaulow, "Degradation of Well Cement by CO2 under Geologic Sequestration Conditions," *Environmental and Science Technology,* p. 4787–4792, 7 May 2007.

[62] V. Barlet-Gouédard, G. Rimmelé, O. Porcherie, N. Quisel and J. Desroches, "A solution against well cement degradation under CO2 geological storage environment," *International Journal of Greenhouse Gas Control,* vol. 3, no. 2, pp. 206–216, March 2009.

[63] Y. Kohei, S. Satoko, K. Hiroyasu, M.J. Stenhouse, Z. Wei, P. Alexandros, Y. Yuji, M. Kazutoshi and S. Shigeru, "The Long-term Corrosion Behavior of Abandoned Wells Under CO2 Geological Storage Conditions: (3) Assessment of Long-term (1,000-year) Performance of Abandoned Wells for Geological CO2 Storage," *Energy Procedia,* vol. 13, pp. 5804–5815, 2013.

[64] R. Beckwith, "Carbon Capture and Storage: A Mixed Review," *Journal of Petroleum Technology,* 2011.

Appendix

Steel	CO_2 phase	P (MPa)	T (°C)	Rate (mm/yr)	Reference	Time (days)	C	Cr	Ni	Mo
3Cr	Vapour	0.2	45	0.45	[7]	7	0.22	2.94	0.3	0.3
3Cr	Vapour	0.2	65	1.03	[7]	7	0.22	2.94	0.3	0.3
3Cr	Vapour	0.2	85	1	[7]	7	0.22	2.94	0.3	0.3
3Cr	Vapour	0.2	105	0.99	[7]	7	0.22	2.94	0.3	0.3
3Cr	Vapour	0.5	40	0.2	[7]	7	0.22	2.94	0.3	0.3
3Cr	Vapour	0.5	60	0.7	[7]	7	0.22	2.94	0.3	0.3
3Cr	Vapour	0.5	80	3.45	[7]	7	0.22	2.94	0.3	0.3
3Cr	Vapour	0.5	100	4.5	[7]	7	0.22	2.94	0.3	0.3
13Cr	Vapour	3	180	1.71	[24]	7	0.025	13		
13Cr	Vapour	3	180	0.225	[24]	7	0.025	13	4	1
13Cr	Vapour	3	180	0.18	[24]	7	0.025	13	4	2
13Cr	Vapour	3	180	0.23	[24]	7	0.025	13	5	1
13Cr	Vapour	3	180	0.15	[24]	7	0.025	13	5	2
13Cr	Vapour	3	180	0.26	[24]	7	0.025	13	4	1
13Cr	Vapour	3	180	0.18	[24]	7	0.025	13	4	2
13Cr	Vapour	1.14	130	0.05	[25]	49	0.02	13	0.4	0.09
13Cr	Vapour	1.14	130	0.005	[25]	49	0.02	12.24	5.73	2.1
J55	Supercritical	8.274	80	0.5	[27]	4	0.19	0.19	0.017	0.092
J55	Supercritical	8.274	80	0.9	[27]	4	0.19	0.19	0.017	0.092
J55	Supercritical	8.274	80	7	[27]	4	0.19	0.19	0.017	0.092
J55	Supercritical	8.274	80	10.5	[27]	4	0.19	0.19	0.017	0.092
J55	Supercritical	8.274	80	12.2	[27]	4	0.19	0.19	0.017	0.092
N80	Supercritical	8.274	80	0.7	[27]	4	0.24	0.036	0.028	0.021
N80	Supercritical	8.274	80	1	[27]	4	0.24	0.036	0.028	0.021
N80	Supercritical	8.274	80	7.2	[27]	4	0.24	0.036	0.028	0.021
N80	Supercritical	8.274	80	11	[27]	4	0.24	0.036	0.028	0.021
N80	Supercritical	8.274	80	12.8	[27]	4	0.24	0.036	0.028	0.021
P110	Supercritical	8.274	80	1	[27]	4	0.26	0.15	0.012	0.01
P110	Supercritical	8.274	80	1.7	[27]	4	0.26	0.15	0.012	0.01
P110	Supercritical	8.274	80	10	[27]	4	0.26	0.15	0.012	0.01
P110	Supercritical	8.274	80	11.2	[27]	4	0.26	0.15	0.012	0.01
P110	Supercritical	8.274	80	14.4	[27]	4	0.26	0.15	0.012	0.01
J55	Vapour	6.89	90	1.854	[28]	4	0.19	0.19	0.017	0.092
J55	Vapour	1.725	80	0.827	[28]	4	0.19	0.19	0.017	0.092
J55	Vapour	1.725	100	0.949	[28]	4	0.19	0.19	0.017	0.092
J55	Vapour	1.725	120	0.894	[28]	4	0.19	0.19	0.017	0.092
J55	Vapour	1.725	140	0.275	[28]	4	0.19	0.19	0.017	0.092
J55	Vapour	1.725	160	0.64	[28]	4	0.19	0.19	0.017	0.092
J55	Vapour	1.725	180	0.351	[28]	4	0.19	0.19	0.017	0.092
J55	Vapour	1.725	200	0.636	[28]	4	0.19	0.19	0.017	0.092

J55	Supercritical	10.34	90	1.105	[28]	4	0.19	0.19	0.017	0.092
N80	Vapour	6.89	90	1.752	[28]	4	0.24	0.036	0.028	0.021
N80	Vapour	1.725	80	0.681	[28]	4	0.24	0.036	0.028	0.021
N80	Vapour	1.725	100	1.053	[28]	4	0.24	0.036	0.028	0.021
N80	Vapour	1.725	120	0.814	[28]	4	0.24	0.036	0.028	0.021
N80	Vapour	1.725	140	0.272	[28]	4	0.24	0.036	0.028	0.021
N80	Vapour	1.725	160	0.191	[28]	4	0.24	0.036	0.028	0.021
N80	Vapour	1.725	200	0.322	[28]	4	0.24	0.036	0.028	0.021
N80	Vapour	1.725	180	0.204	[28]	4	0.24	0.036	0.028	0.021
N80	Supercritical	10.34	90	0.922	[28]	4	0.24	0.036	0.028	0.021
P110	Vapour	6.89	90	2.403	[28]	4	0.26	0.15	0.012	0.01
P110	Vapour	1.725	80	0.948	[28]	4	0.26	0.15	0.012	0.01
P110	Vapour	1.725	100	1.609	[28]	4	0.26	0.15	0.012	0.01
P110	Vapour	1.725	120	0.862	[28]	4	0.26	0.15	0.012	0.01
P110	Vapour	1.725	140	0.41	[28]	4	0.26	0.15	0.012	0.01
P110	Vapour	1.725	160	0.353	[28]	4	0.26	0.15	0.012	0.01
P110	Vapour	1.725	180	0.422	[28]	4	0.26	0.15	0.012	0.01
P110	Vapour	1.725	200	0.95	[28]	4	0.26	0.15	0.012	0.01
P110	Supercritical	10.34	90	0.922	[28]	4	0.26	0.15	0.012	0.01
J55	Vapour	5	20	0.7	[29]	3	0.19	0.049	0.026	0.007
J55	Vapour	5	40	6	[29]	3	0.19	0.049	0.026	0.007
J55	Vapour	5	60	8	[29]	3	0.19	0.049	0.026	0.007
J55	Vapour	5	80	3.9	[29]	3	0.19	0.049	0.026	0.007
J55	Vapour	5	100	0.85	[29]	3	0.19	0.049	0.026	0.007
J55	Vapour	2	80	0.1	[29]	3	0.19	0.049	0.026	0.007
J55	Supercritical	8	80	5.2	[29]	3	0.19	0.049	0.026	0.007
J55	Supercritical	10	80	7.2	[29]	3	0.19	0.049	0.026	0.007
J55	Supercritical	12	80	6.2	[29]	3	0.19	0.049	0.026	0.007
N80	Vapour	5	20	0.7	[29]	3	0.24	0.22	0.028	0.018
N80	Vapour	5	40	5	[29]	3	0.24	0.22	0.028	0.018
N80	Vapour	5	60	9	[29]	3	0.24	0.22	0.028	0.018
N80	Vapour	5	80	3.1	[29]	3	0.24	0.22	0.028	0.018
N80	Vapour	5	100	2	[29]	3	0.24	0.22	0.028	0.018
N80	Vapour	2	80	0.1	[29]	3	0.24	0.22	0.028	0.018
N80	Supercritical	8	80	5.2	[29]	3	0.24	0.22	0.028	0.018
N80	Supercritical	10	80	7.2	[29]	3	0.24	0.22	0.028	0.018
N80	Supercritical	12	80	6.2	[29]	3	0.24	0.22	0.028	0.018
P110	Vapour	5	20	0.8	[29]	3	0.265	0.958	0.042	0.35
P110	Vapour	5	40	5	[29]	3	0.265	0.958	0.042	0.35
P110	Vapour	5	60	10	[29]	3	0.265	0.958	0.042	0.35
P110	Vapour	5	80	4.5	[29]	3	0.265	0.958	0.042	0.35
P110	Vapour	5	100	1.3	[29]	3	0.265	0.958	0.042	0.35
P110	Vapour	2	80	0.2	[29]	3	0.265	0.958	0.042	0.35

P110	Vapour	8	80	5.7	[29]	3	0.265	0.958	0.042	0.35
P110	Vapour	10	80	7.75	[29]	3	0.265	0.958	0.042	0.35
P110	Vapour	12	80	6.4	[29]	3	0.265	0.958	0.042	0.35
P110	Supercritical	8	80	5.7	[29]	3	0.265	0.958	0.042	0.35
P110	Supercritical	10	80	7.75	[29]	3	0.265	0.958	0.042	0.35
P110	Supercritical	12	80	6.4	[29]	3	0.265	0.958	0.042	0.35
K55	Vapour	1	170	0.29	[31]	7				
N80	Vapour	0.4	90	1.689	[32]	3	0.24	0.036	0.028	0.021
N80	Vapour	0.4	90	0.172	[32]	3	0.24	0.036	0.028	0.021
N80	Vapour	0.4	90	0.789	[32]	3	0.24	0.036	0.028	0.021
N80	Vapour	0.4	90	0.621	[32]	3	0.24	0.036	0.028	0.021
N80	Vapour	0.4	90	0.511	[32]	3	0.24	0.036	0.028	0.021
N80	Vapour	4	90	0.55	[36]	5	0.42	0.051	0.005	0.18
N80	Vapour	4	90	1.25	[36]	5	0.42	0.051	0.005	0.18
N80	Vapour	4	90	3.55	[36]	5	0.42	0.051	0.005	0.18
N80	Vapour	4	90	4.95	[36]	5	0.42	0.051	0.005	0.18
L80	Vapour	4	65	8.5	[34]	2	0.3	0.85		
L80	Supercritical	8	65	9.9	[34]	2	0.3	0.85		
L80	Supercritical	12	65	11	[34]	2	0.3	0.85		
L80	Vapour	4	90	6.1	[34]	2	0.3	0.85		
L80	Supercritical	8	90	3.4	[34]	2	0.3	0.85		
L80	Supercritical	12	90	4.8	[34]	2	0.3	0.85		
L80	Supercritical	15	50	0.375	[35]	30	0.315	0.04	0.01	0.11
L80	Supercritical	15	50	3.534	[35]	7	0.315	0.04	0.01	0.11
L80	Supercritical	30	50	2.774	[35]	7	0.315	0.04	0.01	0.11
L80	Vapour	0.5	60	1.5568	[36]	30	0.22	1.2	0.5	
L80	Vapour	0.5	90	1.0627	[36]	30	0.22	1.2	0.5	
L80	Vapour	0.5	150	1.3941	[36]	30	0.22	1.2	0.5	
L80	Vapour	0.5	60	1.467	[36]	30	0.22	1.2	0.5	
L80	Vapour	0.5	90	0.7794	[36]	30	0.22	1.2	0.5	
L80	Vapour	0.5	150	2.0835	[36]	30	0.22	1.2	0.5	
L80	Vapour	0.5	60	1.1466	[36]	30	0.22	1.2	0.5	
L80	Vapour	0.5	90	0.9401	[36]	30	0.22	1.2	0.5	
L80	Vapour	0.5	150	0.9807	[36]	30	0.22	1.2	0.5	
L80	Vapour	0.5	60	1.0967	[36]	30	0.22	1.2	0.5	
L80	Vapour	0.5	90	0.6833	[36]	30	0.22	1.2	0.5	
L80	Vapour	0.5	150	1.0032	[36]	30	0.22	1.2	0.5	
L80	Vapour	0.1	20	0.56	[37]	3	0.17	0.81	0.014	0.003
L80	Vapour	0.1	20	0.49	[37]	3	0.21	0.82	0.015	0.031
L80	Vapour	0.1	20	0.45	[37]	3	0.17	0.81	0.014	0.003
L80	Vapour	0.1	20	0.52	[37]	3	0.21	0.82	0.015	0.031
L80	Vapour	0.1	20	0.89	[37]	3	0.17	0.81	0.014	0.003
L80	Vapour	0.1	20	0.29	[37]	3	0.21	0.82	0.015	0.031

L80	Vapour	0.3	20	1.29	[37]	3	0.17	0.81	0.014	0.003
L80	Vapour	0.3	20	0.71	[37]	3	0.21	0.82	0.015	0.031
L80	Vapour	0.3	20	1.26	[37]	3	0.17	0.81	0.014	0.003
L80	Vapour	0.3	20	0.8	[37]	3	0.21	0.82	0.015	0.031
L80	Vapour	0.3	20	1.13	[37]	3	0.17	0.81	0.014	0.003
L80	Vapour	0.3	20	0.82	[37]	3	0.21	0.82	0.015	0.031
T95	Supercritical	41.37	38	15	[38]	7	0.33	1.01	0.03	0.79
T95	Supercritical	41.37	38	20	[38]	7	0.33	1.01	0.03	0.79
T95	Supercritical	41.37	38	17	[38]	7	0.33	1.01	0.03	0.79
T95	Supercritical	41.37	38	17.5	[38]	7	0.33	1.01	0.03	0.79
Q125	Supercritical	41.37	38	3.2	[38]	7	0.26	0.91	0.04	0.26
Q125	Supercritical	41.37	38	9.5	[38]	7	0.26	0.91	0.04	0.26
Q125	Supercritical	41.37	38	10	[38]	7	0.26	0.91	0.04	0.26
Q125	Supercritical	41.37	38	10	[38]	7	0.26	0.91	0.04	0.26
C110	Supercritical	41.37	38	13	[38]	7	0.3	1.01	0.01	0.78
C110	Supercritical	41.37	38	14.5	[38]	7	0.3	1.01	0.01	0.78
C110	Supercritical	41.37	38	9	[38]	7	0.3	1.01	0.01	0.78
P110	Vapour	4	100	6.1843	[39]	5	0.19		0.028	0.028
P110	Vapour	4	160	0.8754	[39]	5	0.19		0.028	0.028
P110	Vapour	4	90	0.9394	[40]	3				
P110	Vapour	4	110	0.4491	[40]	3				
P110	Vapour	0.1	100	0.64	[41]	7	0.26		0.028	0.028
P110	Vapour	2	100	0.76	[41]	7	0.26		0.028	0.028
P110	Vapour	4	100	0.91	[41]	7	0.26		0.028	0.028
P110	Vapour	6	100	0.83	[41]	7	0.26		0.028	0.028
Q125	Vapour	1	30	1.012	[42]	7	0.2	1.03	0.2	0.3
Q125	Vapour	2	30	0.9	[43]	7	0.15	0.46	0.2	0.15
Q125	Vapour	2	60	2.8	[43]	7	0.15	0.46	0.2	0.15
Q125	Vapour	2	90	3.6	[43]	7	0.15	0.46	0.2	0.15
Q125	Vapour	2	120	2.4	[43]	7	0.15	0.46	0.2	0.15
20Cr-25Ni	Supercritical	9.5	50	0.0003	[44]	4	0.02	20	25	4.5
20Cr-25Ni	Supercritical	13	80	0.001	[44]	4	0.02	20	25	4.5
20Cr-25Ni	Supercritical	16	110	0.0001	[44]	4	0.02	20	25	4.5
20Cr-25Ni	Supercritical	18.2	130	0.00005	[44]	4	0.02	20	25	4.5
20Cr-25Ni	Supercritical	9.5	50	0.00006	[44]	4	0.02	20	25	4.5
20Cr-25Ni	Supercritical	13.5	80	0.00009	[44]	4	0.02	20	25	4.5
20Cr-25Ni	Supercritical	17	110	0.00011	[44]	4	0.02	20	25	4.5
20Cr-25Ni	Supercritical	21.5	130	0.00005	[44]	4	0.02	20	25	4.5
13Cr	Supercritical	9.5	50	0.003	[44]	4	0.195	13		

13Cr	Supercritical	13	80	0.0038	[44]	4	0.195	13		
13Cr	Supercritical	16	110	0.009	[44]	4	0.195	13		
13Cr	Supercritical	18.2	130	0.003	[44]	4	0.195	13		
13Cr	Supercritical	9.5	50	0.00033	[44]	4	0.195	13		
13Cr	Supercritical	13.5	80	0.0006	[44]	4	0.195	13		
13Cr	Supercritical	17	110	0.0008	[44]	4	0.195	13		
13Cr	Supercritical	21.5	130	0.0004	[44]	4	0.195	13		
22Cr	Supercritical	9.5	50	0.0007	[44]	4	0.03	22	5	3
22Cr	Supercritical	13	80	0.0008	[44]	4	0.03	22	5	3
22Cr	Supercritical	16	110	0.0004	[44]	4	0.03	22	5	3
22Cr	Supercritical	18.2	130	0.0001	[44]	4	0.03	22	5	3
22Cr	Supercritical	9.5	50	0.00006	[44]	4	0.03	22	5	3
22Cr	Supercritical	13.5	80	0.0001	[44]	4	0.03	22	5	3
22Cr	Supercritical	17	110	0.00014	[44]	4	0.03	22	5	3
22Cr	Supercritical	21.5	130	0.00006	[44]	4	0.03	22	5	3
13Cr	Vapour	0.1	60	0.002	[45]	29.167	0.46	13.39	0.13	0.03
13Cr	Vapour	6	60	0.0002	[45]	29.167	0.46	13.39	0.13	0.03
1Cr	Vapour	0.1	60	0.0059	[45]	29.167	0.43	1.05	0.04	0.22
1Cr	Vapour	6	60	0.0015	[45]	29.167	0.43	1.05	0.04	0.22
13Cr	Vapour	0.2	50	0.1	[46]	90	0.029	12.78	5.12	2.23
22Cr	Vapour	0.2	50	0.01	[46]	90	0.23	22.91	5.65	3.21
P110	Vapour	0.2	50	0.18	[46]	90	0.25	1.06	0.025	0.65
J55	Supercritical	9.5	70	0.1	[47]	12.5				
J55	Supercritical	9.5	70	0.1	[47]	12.5				
N80	Supercritical	9.5	70	0.1	[47]	12.5				
N80	Supercritical	9.5	70	0.1	[47]	12.5				
J55	Supercritical	9.5	70	2	[47]	4.67				
J55	Supercritical	9.5	70	0.2	[47]	4.67				
N80	Supercritical	9.5	70	1.15	[47]	4.67				
N80	Supercritical	9.5	70	0.2	[47]	4.67				
J55	Vapour	0.5	65	3.3	[48]	2	0.36	0.051	0.009	
J55	Vapour	1	65	6.7	[48]	2	0.36	0.051	0.009	
J55	Vapour	1.5	65	5.9	[48]	2	0.36	0.051	0.009	
J55	Vapour	2.5	65	4.7	[48]	2	0.36	0.051	0.009	
J55	Vapour	3	65	3.5	[48]	2	0.36	0.051	0.009	
J55	Vapour	5	65	3.95	[48]	2	0.36	0.051	0.009	
J55	Vapour	7	65	5.2	[48]	2	0.36	0.051	0.009	
J55	Supercritical	9	65	5.2	[48]	2	0.36	0.051	0.009	
J55	Supercritical	11	65	5.2	[48]	2	0.36	0.051	0.009	
J55	Supercritical	13	65	5.2	[48]	2	0.36	0.051	0.009	
J55	Supercritical	15	65	5.2	[48]	2	0.36	0.051	0.009	
J55	Vapour	5	30	0.09	[49]	3	0.38	0.09		
J55	Vapour	5	48	0.088	[49]	3	0.38	0.09		

J55	Vapour	5	55	0.13	[49]	3	0.38	0.09		
J55	Vapour	5	65	0.148	[49]	3	0.38	0.09		
N80	Vapour	0.5	50	6.5	[50]	2	0.33	0.013	0.026	0.016
N80	Vapour	1	50	9.5	[50]	2	0.33	0.013	0.026	0.016
N80	Vapour	2	50	12	[50]	2	0.33	0.013	0.026	0.016
N80	Vapour	3	50	9.5	[50]	2	0.33	0.013	0.026	0.016
N80	Vapour	4	50	9	[50]	2	0.33	0.013	0.026	0.016
N80	Vapour	5	50	3.8	[50]	2	0.33	0.013	0.026	0.016
N80	Supercritical	10	50	1.8	[50]	2	0.33	0.013	0.026	0.016
N80	Supercritical	10	65	8.4	[50]	2	0.33	0.013	0.026	0.016
N80	Supercritical	10	80	11.8	[50]	2	0.33	0.013	0.026	0.016
N80	Vapour	0.15	100	0.75	[51]	3	0.26	0.148	0.028	0.028
N80	Vapour	0.6	100	1.15	[51]	3	0.26	0.148	0.028	0.028
N80	Vapour	1	100	2.25	[51]	3	0.26	0.148	0.028	0.028
N80	Vapour	4	100	7.2	[51]	3	0.26	0.148	0.028	0.028
N80	Vapour	0.1	80	4.65	[52]	3	0.19	0.55		0.14
3Cr	Vapour	0.1	80	2.9	[52]	3	0.1	3.75		0.25
3Cr	Vapour	0.1	80	3.25	[52]	3	0.11	3.3		0.21
N80	Vapour	8	45	0.056	[53]	32	0.29	0.24	0.08	0.09
L80	Vapour	1	25	0.2334	[54]	2	0.22	0.013		
L80	Vapour	4	25	0.3905	[54]	2	0.22	0.013		
L80	Vapour	6	25	0.4044	[54]	2	0.22	0.013		
L80	Vapour	1	25	0.254	[54]	2	0.22	0.013		
L80	Vapour	4	25	0.347	[54]	2	0.22	0.013		
L80	Vapour	6	25	0.4681	[54]	2	0.22	0.013		
L80	Vapour	0.1	80	0.13	[55]	5	0.43		0.25	
L80	Vapour	0.1	80	0.13	[55]	5	0.43	0.95	0.25	
L80	Vapour	0.1	80	0.3	[55]	5	0.11	3.4	0.15	0.6
C110	Supercritical	10.8	120	0.55	[56]	7	0.27		0.04	0.72
P110	Vapour	5	90	1.12	[57]	15	0.25	0.15	0.032	0.27
P110	Vapour	5	90	1.08	[57]	15	0.26	2.99	0.043	0.19
P110	Vapour	5	90	1.57	[57]	15	0.25	5.11	0.041	0.21
P110	Vapour	0.5	120	0.03	[58]	1	0.26			0.01
P110	Vapour	1.5	120	2.23	[58]	1	0.26			0.01
P110	Vapour	3	120	1.1	[58]	1	0.26			0.01
N80	Vapour	0.5	120	0.03	[58]	1	0.24			0.021
N80	Vapour	1.5	120	1.5	[58]	1	0.24			0.021
P110	Vapour	0.1	90	4.2	[59]	5	0.22	0.18	0.01	0.03

Original scientific paper

Received: Nov 14, 2019
Accepted: Dec 09, 2019
DOI: 10.2478/rmzmag-2019-0036

Petrochemistry and petrogenesis of the Precambrian Basement Complex rocks around Akungba-Akoko, southwestern Nigeria

Petrokemija in petrogeneza predkambrijskih kamnin podlage na območju Akungba-Akoko, JZ Nigerij

Abimbola Chris Ogunyele*, Oladotun Afolabi Oluwajana, Iyanuoluwa Queen Ehinola, Blessing Ene Ameh, Toheeb Akande Salaudeen

Department of Earth Sciences, Adekunle Ajasin University, PMB 001 Akungba-Akoko, Ondo State, Nigeria
* abimbola.ogunyele@aaua.edu.ng

Abstract

Field, mineralogical and petrochemical studies of the Precambrian Basement Complex rocks around Akungba-Akoko were carried out with the aim of determining their petrology, petrochemical characteristics and petrogenesis. The petrology of Akungba-Akoko area comprises migmatite, granite gneiss and biotite gneiss intruded by biotite granite, charnockite and minor felsic and basic rocks. Seventeen representative samples of the granite gneiss, biotite gneiss, biotite granite and charnockite were collected during field geological mapping of the area for petrographic and geochemical analyses. Modal mineralogy revealed that the granite gneiss, biotite gneiss and granite have assemblages of quartz + feldspar + mica ± hornblende + opaques and are granitic in composition. The charnockite is characterized by anhydrous mineral assemblage of quartz + feldspar + biotite + hornblende + pyroxene + opaques. Petrochemical data of the rocks revealed that they are moderately to highly enrich in SiO_2, sub-alkaline, peraluminous, magnesian to ferroan and calcic and have K/Rb < 283. The geochemical characteristics and discrimination of the rocks indicated that the granite gneiss and biotite gneiss are orthogneisses formed by metamorphism of igneous protoliths of granitic composition and the biotite granite and charnockite are of igneous/magmatic origin. The biotite granite, charnockite and the igneous protoliths of the biotite gneiss are I-type granitoids formed from crustal igneous-sourced melt(s), while the igneous protoliths of the granite gneiss is a S-type granitoid probably derived

Povzetek

Z namenom določitve petrologije, petrokemičnih značilnosti in petrogeneze so bile na območju Akungba-Akoko izvedene terenske, mineraloške in petrokemične raziskave predkambrijskih kamnin podlage. Petrologijo območja Akungba-Akoko sestavljajo migmatit, granitni gnajs in biotitni gnajs, intrudirani z biotitnim granitom, charnokitom in manjšimi felsičnimi in bazičnimi kamninami. Med terenskim geološkim kartiranjem območja je bilo zbranih sedemnajst reprezentativnih vzorcev granitnega gnajsa, biotitnega gnajsa, biotitnega granita in charnokita za petrografske in geokemične analize. Modalne mineraloške preiskave so pokazale da granitni gnajs, biotitni gnajs in granit vsebujejo kremen + glinence + sljudo ± rogovačo + neprozorne minerale in so granitni v kompoziciji. Charnokit je karakteriziran kot nehidriran mineral sestavljen iz kremena + glinavca + biotita + rogovače + piroksena + neprozornega minerala. Petrokemični podatki kamnin kažejo, da so srednje do visoko bogate z SiO_2, sub-alkalne, peraluminaste, magnezijske do železove, kalcijske in imajo razmerje K/Rb < 283. Geokemične karakteristike in diskriminacije kamnin kažejo, da so granitni gnajsi in biotitni gnajsi ortognajsi, nastali s preobrazbo magmatskih protolitov granitne kompozicije in da so biotitni graniti in charnokiti magmatskega nastanka. Biotitni granit, charnokit in magmatski protoliti biotitnih gnajsov so granitoidi I-tipa, nastali s taljenjem skorje, medtem ko so magmatski protoliti granitnih gnajsov granitoidi S-tipa, verjetno nastali iz taljenja plitve skorje ali sedimentov. Tektonska diskriminacija kamnin prikazuje, da

from shallow crustal or sedimentary-sourced melt(s). Tectonic discrimination of the rocks indicated that they were formed during a phase of magmatic activity related to collision and subduction.

Keywords: granitoids, mineralogy, orthogneisses, petrogenesis, petrochemistry

so nastale med stopnjo vulkanske aktivnosti povezane s trkom in subdukcijo.

Ključne besede: granitoidi, mineralogija, ortognajsi, petrogeneza, petrokemija

Introduction

The Precambrian Basement Complex rocks of Akungba-Akoko area form a part of the southwestern Nigerian Basement Complex (Figure 1). The Nigerian Basement Complex lies within the reactivated Pan-African mobile belt extending between the West African Craton in the west and the Congo Craton in the southeast [1, 2]. It comprises three major lithological units: the Migmatite–Gneiss Complex, the Schist Belts and the Older Granites, which intrude the former two units [3].

The petrology, mineralogy, geochemical characteristics, structure, petrogenesis (origin) and other features of the Basement Complex rocks of Nigeria, particularly the Schist Belts, have been studied to considerable details by several researchers [4–10]. However, there are still more work to be done, particularly on the Migmatite–Gneiss Complex and the Pan-African granitoids (Older Granite suite and charnockitic rocks), in order to determine their petrogenesis (origin) and possible evolutionary models, tectonics, ages and correlation with similar rock groups in other parts of the world [1, 11, 12].

In view of the above, this paper presents field, mineralogical and petrochemical data of the Migmatite–Gneiss Complex rocks and granitoids around Akungba-Akoko and discusses their petrology, mineralogy and petrochemical characteristics and petrogenesis.

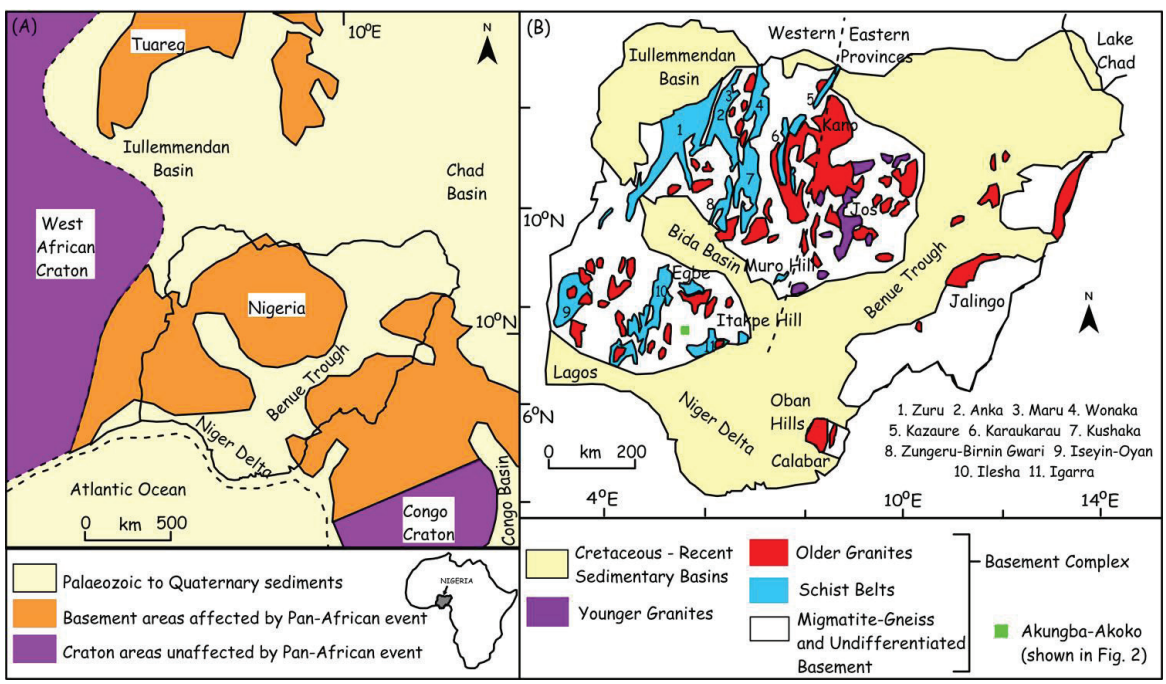

Figure 1: *(a) Regional geological map of Nigeria within the Pan-African mobile belt between the West African and Congo Cratons and (b) outline geological map of Nigeria showing Akungba-Akoko in the southwestern Nigerian Basement Complex (modified after [3]).*

Methods

Geological mapping of Akungba-Akoko area on a scale of 1:20,000 was carried out to determine the rock types occurring in the area and their structural relationships. Seventeen fresh representative rock samples comprising five granite gneiss, four biotite gneiss, four biotite granite and four charnockite were collected for petrographic and geochemical analyses. Thin sections of seven samples were prepared and studied, and modal compositions were determined using a transmitted light microscope at the Department of Geology, University of Ibadan, Nigeria. Major and trace element geochemical analyses of ten rock samples were

carried out using the Energy Dispersive X-Ray Fluorescence (ED-XRF) machine (PANalytical model) at the National Geosciences Research Laboratory, Kaduna, Nigeria. The samples were crushed and pulverised to <63 μm. About 15 g of the pulverised samples were used to make glass beads and pressed pellets, which were slotted into the computerised ED-XRF spectrometer for major and trace elemental analyses, respectively. The laboratory results were interpreted using discrimination diagrams to determine their petrochemical characteristics and petrogenesis.

Results and Discussion

Petrology and Mineralogy

The petrology of Akungba-Akoko area comprises mainly Migmatite–Gneiss Complex rocks intruded by Pan-African granitoids (Figure 2). The Migmatite–Gneiss Complex rocks occurring in the area are migmatite, granite gneiss and biotite gneiss. Granite gneiss is the predominant rock type covering more than 85% of the area. The granite gneiss is intruded by biotite granite, which trends NE–SW from the central to the northeastern end of the area. In the north-central part of the area, a core of charnockite and

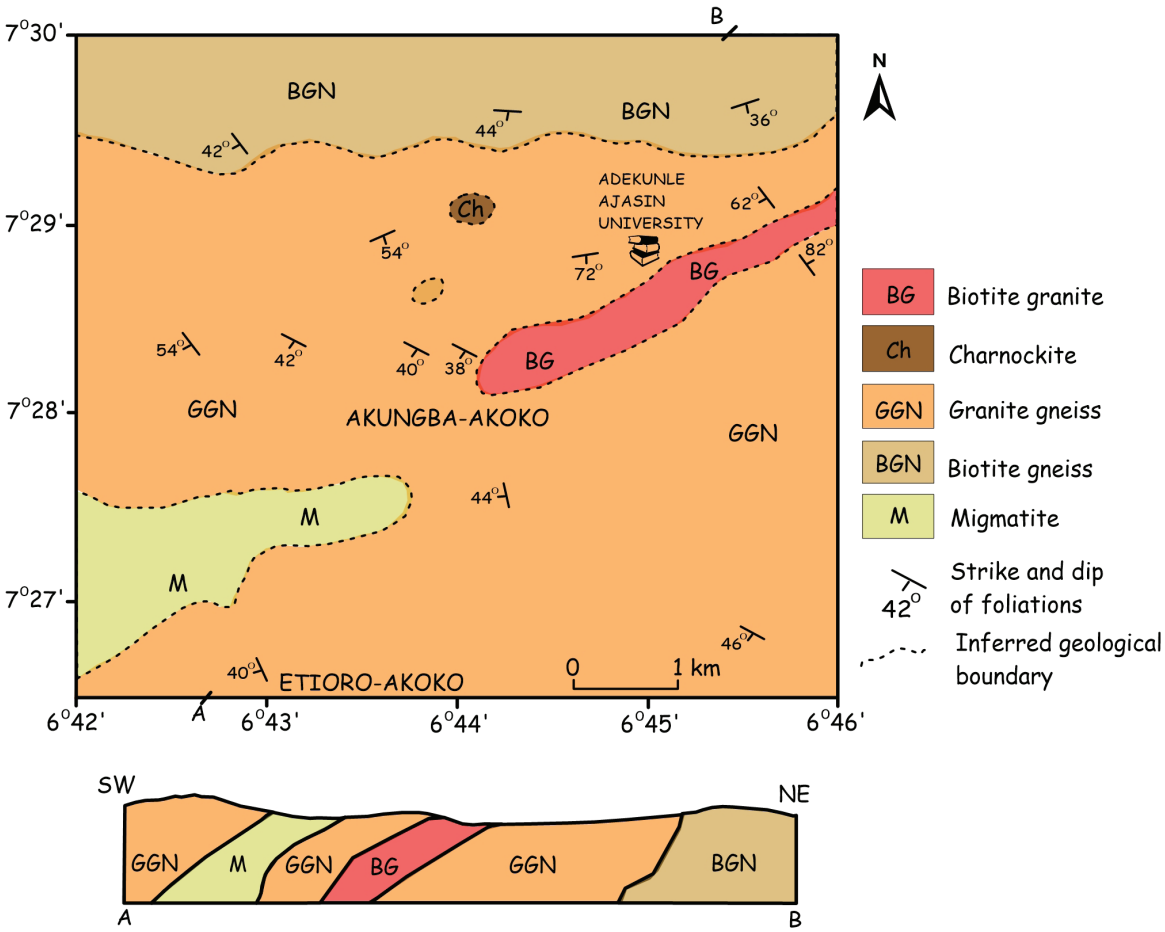

Figure 2: *Geological map and schematic cross-section of Akungba-Akoko area, southwestern Nigeria.*

an enclave (large xenolith) of biotite gneiss occur within the granite gneiss. This lithologic association suggests that the charnockite is intrusive into the granite gneiss; hence, it is younger than the latter and the biotite gneiss is probably older than the granite gneiss. Field photographs and modal compositions of the various lithologies are shown in Figure 3 and Table 1, respectively.

Figure 3: *Field photographs showing (a) granite gneiss intruded by pegmatites (folded and faulted), (b) folded biotite gneiss, (c) biotite granite containing massive melanocratic segregations and (d) boulders of charnockite in Akungba-Akoko.*

Table 1: *Average modal mineralogical compositions of Akungba-Akoko Basement Complex rocks.*

Minerals (vol.%)	GGN1b	GGN2b	BGN1b	BGN2b	BG1b	BG2b	Ch1b
Quartz	29.40	26.60	26.40	26.40	25.30	21.40	22.30
K-feldspar	28.60	23.30	21.60	23.40	22.30	18.00	18.30
Plagioclase feldspar	34.50	35.20	31.00	33.20	32.00	28.30	32.30
Biotite	6.10	8.40	10.10	10.20	14.90	25.40	8.40
Hornblende	-	3.30	8.50	5.10	3.20	5.10	6.00
Muscovite	0.90	2.50	1.40	1.20	2.00	1.00	5.30
Opaque	0.60	0.70	0.90	0.60	0.80	0.90	0.40
Pyroxene	-	-	-	-	-	-	7.70
Total	100.10	100.00	99.90	100.10	100.50	100.10	100.70

GGN – granite gneiss, BGN – biotite gneiss, BG – biotite granite, Ch – charnockite.

The granite gneiss of Akungba-Akoko area (Figure 3a) is weakly to moderately foliated, light grey and medium to coarse grained with a megacrystic (blastoporphyritic to porphyroblastic) fabric. It is composed of alternating bands of light- and dark-coloured minerals, most of which are folded. The light-coloured bands are quartz and feldspar rich, while the dark-coloured bands are rich in biotite, hornblende and other ferromagnesian minerals. Quartz and feldspar are the porphyroblasts in the gneiss, and they often have an augen

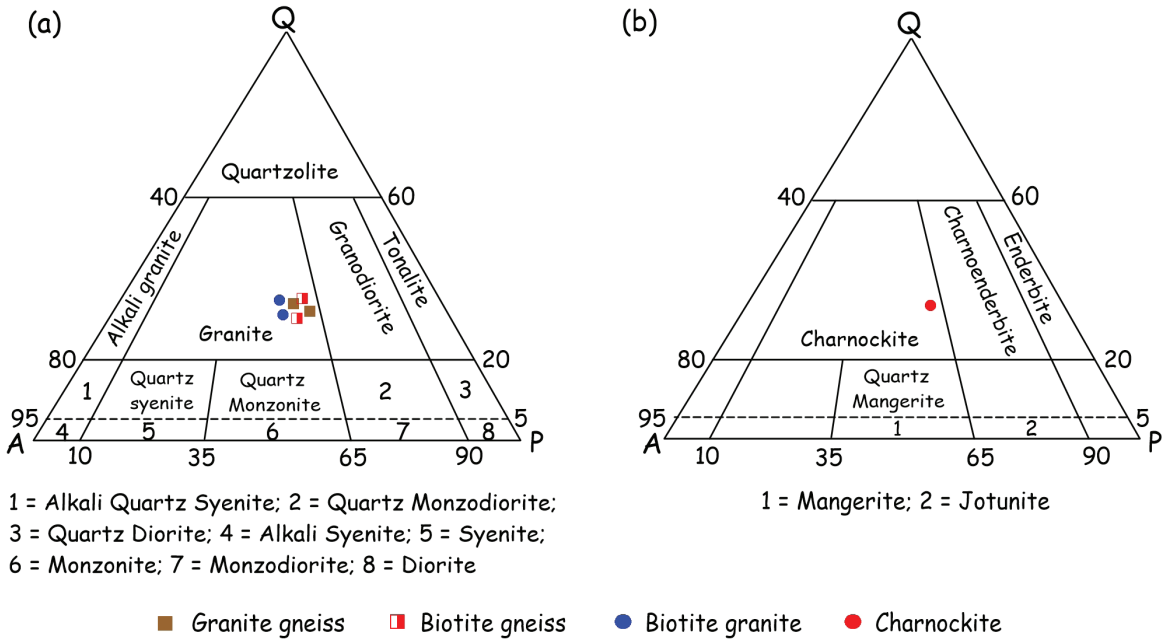

Figure 4: *QAP diagrams for classifying (a) the gneisses and biotite granite (after [14]) and (b) charnockite (after [15]) of Akungba-Akoko.*

(eye-like) shape. The granite gneiss, in some locations, contains garnets and quartzitic inclusions. The rock mainly trends WNW-ESE to ENE-WSW with moderate to steep dips to the south. Pegmatites, vein quartz, quartz lenses, basic dykes and sills are abundant in the granite gneiss, sometimes giving the gneiss a migmatitic appearance.

Biotite gneiss occurs in the northern part of the area forming mountains/ridges, which extends northwards to Ikare-Akoko area and beyond. [5, 13] referred to this rock as grey gneiss. The rock is composed essentially of quartz, feldspar and biotite (Table 1) and is dark grey, medium grained and strongly foliated with thin alternating bands of light- and dark-coloured minerals (Figure 3b). A ridge of migmatite composed of granite gneiss, biotite gneiss, granite, aplite, pegmatite and vein quartz extends from the southwestern part of Akungba to Supare-Akoko area in the ENE–WSW direction. The rock is highly deformed with the component rocks being intricately mixed and folded. Ptygmatic folds, faults and joints trending in different directions are abundant in this rock.

The biotite granite intruding granite gneiss in Akungba-Akoko is very rich in biotite and hornblende giving it a very dark colour. The granite is medium to coarse grained; rich in quartz, feldspar, biotite and hornblende (Table 1) and contains massive melanocratic segregations of biotite, hornblende and iron (Figure 3c). The coarse-grained, dark-coloured charnockite (Figure 3d) with a shining appearance occurring in the granite gneiss is pyroxene-bearing (Table 1) and rich in quartz, feldspar, biotite and muscovite. The charnockite occurs as boulders, some of which are weathered. Minor rocks occurring in the area include pegmatite, vein quartz, aplite, and basic dykes and sills are often found as intrusives within the gneisses and migmatite. The QAP diagrams of [14, 15] revealed that the granite gneiss, biotite gneiss and biotite granite are granitic in composition (Figure 4a) and the charnockite is a true charnockite (Figure 4b).

Petrochemistry and Petrogenesis

Petrochemical data of the basement rocks around Akungba-Akoko (Tables 2 and 3) revealed that the rocks have moderate to high SiO_2 contents: granite gneiss (73.86–74.58 wt.%), biotite gneiss (67.80–73.62 wt.%), biotite granite (59.83–60.06 wt.%) and charnockite (57.50–59.70 wt.%). Based on silica contents, the gneisses are classified as acidic rocks, while

Table 2: *Major element compositions (in wt.%) of the Basement Complex rocks of Akungba-Akoko.*

Major oxides	Granite gneiss			Biotite gneiss		Biotite granite		Charnockite		
	GGN1	GGN2	GGN3	BGN1	BGN2	BG1	BG2	Ch1	Ch2	Ch3
SiO_2	74.40	73.86	74.58	73.62	67.80	60.06	59.83	57.50	58.72	59.70
TiO_2	0.18	0.23	0.32	0.50	0.69	1.00	1.03	1.09	0.98	0.88
Al_2O_3	13.40	13.84	13.52	12.60	14.63	16.77	17.04	17.90	16.78	15.20
Fe_2O_3	3.26	3.83	3.68	3.58	5.33	6.66	6.68	6.70	6.68	6.73
MnO	0.03	0.06	0.04	0.05	0.04	0.13	0.15	0.25	0.26	0.13
MgO	0.27	0.32	0.21	0.76	1.00	3.02	2.92	2.41	3.02	3.11
CaO	3.00	2.89	2.04	3.01	4.18	5.54	6.05	7.11	6.93	7.02
Na_2O	2.01	1.75	1.80	1.62	2.06	0.84	0.67	0.86	0.72	0.70
K_2O	2.40	2.59	3.00	3.63	2.54	2.29	2.39	2.35	2.37	3.03
P_2O_5	ND	ND	ND	ND	ND	ND	ND	0.01	ND	0.01
LOI	0.51	0.58	0.71	0.90	1.40	3.25	3.03	2.86	3.15	2.45
TOTAL	99.46	99.95	99.90	100.27	99.67	99.56	99.79	99.04	99.61	98.96

GGN – granite gneiss, BGN – biotite gneiss, BG – biotite granite, Ch – charnockite.

Table 3: *Trace element compositions (in ppm) of the Basement Complex rocks of Akungba-Akoko.*

Trace elements	Granite gneiss			Biotite gneiss		Biotite granite		Charnockite		
	GGN1	GGN2	GGN3	BGN1	BGN2	BG1	BG2	Ch1	Ch2	Ch3
Ba	300	470	310	510	240	580	684	815	722	814
Co	5	6	4.9	3	1	3	4	3.8	4	2
Cr	0.38	0.3	0.28	0.2	0.27	1	2	2	2	1
Nb	7	5	4	2	2	1	2	3	3	2
Ni	8	7	6	3	12	6	9	7	5	4
Rb	82	90	122	100	130	120	100	98	120	116
Sc	2	3	3	1	1	1	1	3	1	-
Sr	110	90	116	88	40	138	150	14	167	132
Th	18	12	22	16	24	12	13	12	14	10
V	1	12.5	17	2	3	13.7	13	10	12	16
Y	27	14	32	40	14	31	42	40	38	26
Zr	100	66	80	122	70	119	130	110	120	116
K/Rb	242.89	238.82	204.07	301.25	162.15	158.37	198.34	199.00	163.90	216.77

GGN – granite gneiss, BGN – biotite gneiss, BG – biotite granite, Ch – charnockite.

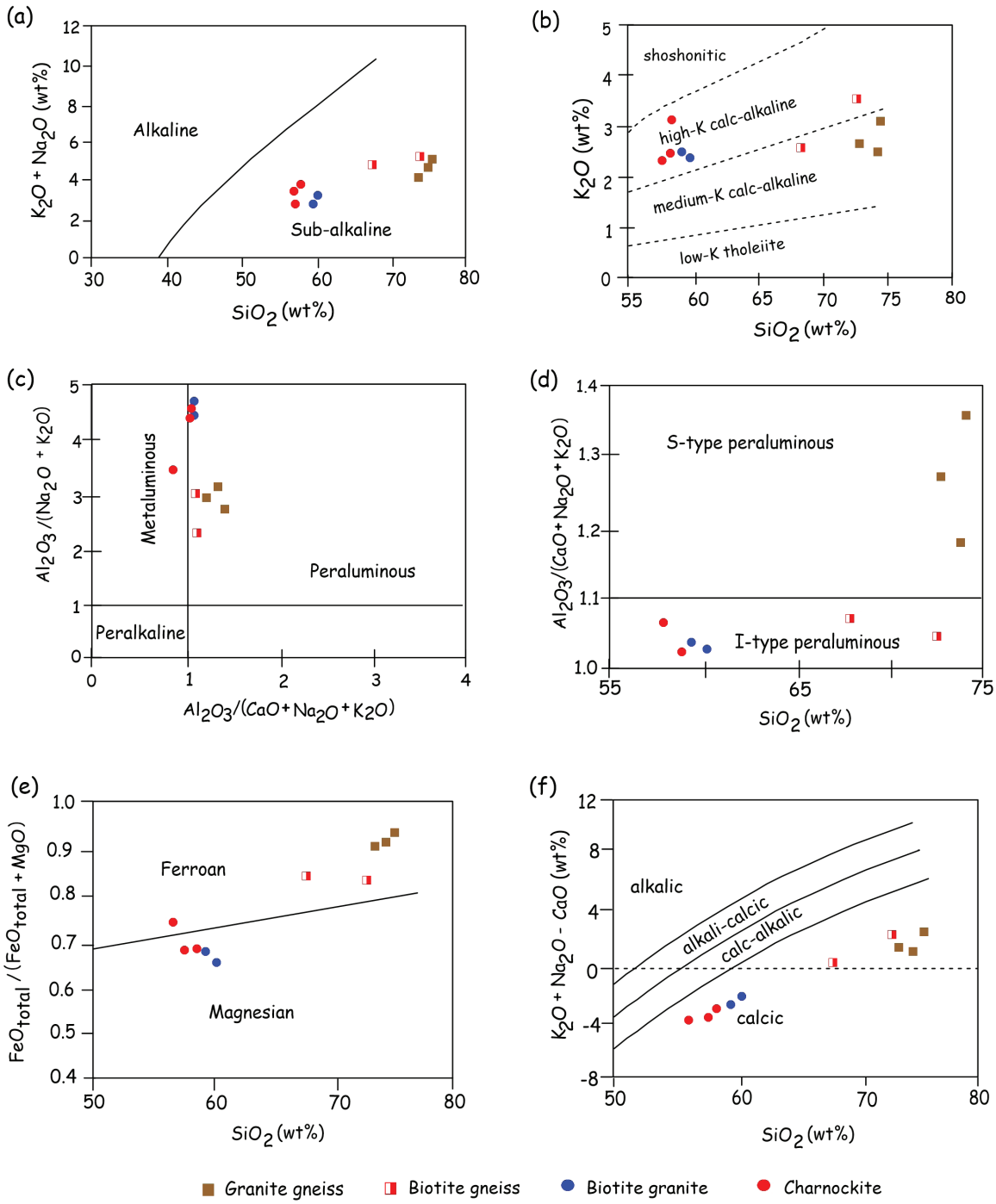

Figure 5: *Petrochemical diagrams for discriminating Akungba-Akoko granite gneiss, biotite gneiss, biotite granite and charnockite. (a) $K_2O + Na_2O$ versus SiO_2 plot (after [17]), (b) K_2O versus SiO_2 plot (after [18]), (c) $Al_2O_3/(Na_2O + K_2O)$ versus $Al_2O_3/(CaO + Na_2O + K_2O)$ molecular plot (after [19]), (d) $Al_2O_3/(CaO + Na_2O + K_2O)$ versus SiO_2 (after [20]), (e) $FeO_{total}/(FeO_{total} + MgO)$ versus SiO_2 (after [21]) and (f) $K_2O + Na_2O - CaO$ versus SiO_2 plot (after [21]).*

the biotite granite and charnockite are classified as intermediate rocks. Al_2O_3 in the rocks range from 12.60 to 17.90 wt.%. The moderate to high silica and alumina contents of these rocks are correlatable with their high quartz and feldspar contents (Table 1). Fe_2O_3 and MgO are relatively higher in the charnockite (Fe_2O_3: 6.68–6.73 wt.%; MgO: 2.41–3.11 wt.%),

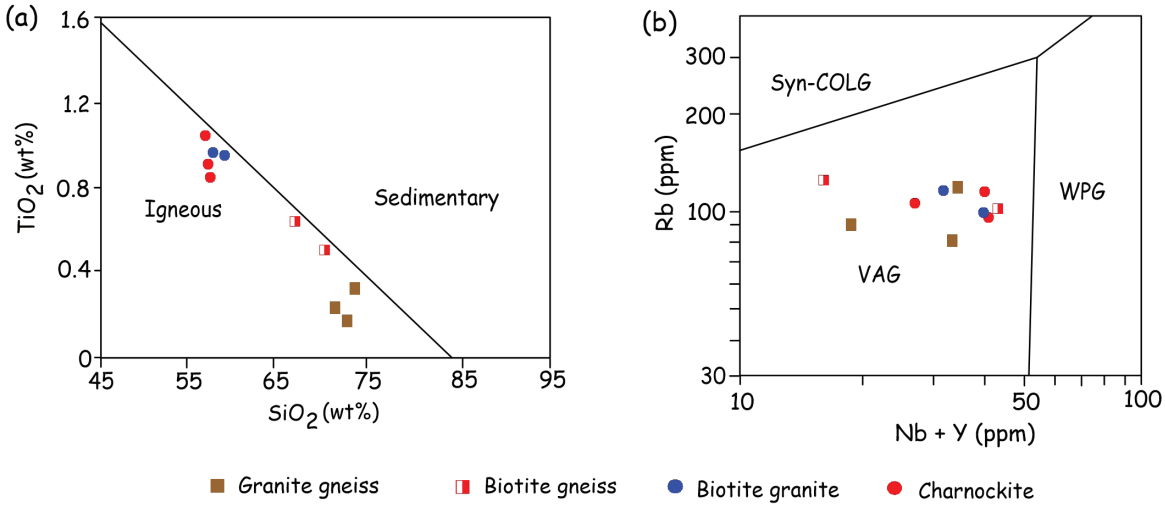

Figure 6: *Petrochemical diagrams of (a) TiO_2 versus SiO_2 (after [22]) and (b) Rb versus Nb + Y (after [25]) for determining the petrogenesis and tectonic settings of Akungba-Akoko granite gneiss, biotite gneiss, biotite granite and charnockite.*

biotite granite (Fe_2O_3: 6.66–6.68 wt.%; MgO: 2.92–3.02 wt.%) and biotite gneiss (Fe_2O_3: 3.58–5.33 wt.%; MgO: 0.76–1.00 wt.%) compared to the granite gneiss (Fe_2O_3: 3.26–3.83 wt.%; MgO: 0.21–0.32 wt.%). This is as a result of the higher amount of mafic minerals (biotite + hornblende + pyroxene + opaques) in the charnockite, biotite granite and biotite gneiss relative to the granite gneiss. CaO is relatively higher than Na_2O and K_2O in almost all the rocks. All the rocks are also characterized by low to moderate Ba and low Cr, Nb and V contents pointing to a felsic to intermediate composition. The average K/Rb ratios of the rocks (granite gneiss: 228.59, biotite gneiss: 231.70, biotite granite: 178.35 and charnockite: 193.22) are less than that of crustal rocks (283) [16], therefore suggesting crustal sources of the rocks.

Geochemical discrimination of the rocks in the area using the $Na_2O + K_2O$ versus SiO_2 plot [17] revealed that they are sub-alkaline rocks (Figure 5a). On the K_2O versus SiO_2 plot [18], the biotite and granite gneisses are essentially medium-K calc-alkaline rocks, while the biotite granite and charnockite are high-K calc-alkaline rocks (Figure 5b). All the rock samples except one charnockite sample are plotted within the peraluminous field of the $Al_2O_3/(Na_2O + K_2O)$ versus $Al_2O_3/(CaO + Na_2O + K_2O)$ molecular plot of [19] (Figure 5c). The $Al_2O_3/(CaO + Na_2O + K_2O)$ versus SiO_2 plot [20] further distinguished the granite gneiss as S-type peraluminous granitoid and the biotite gneiss, biotite granite and charnockite as I-type peraluminous granitoids (Figure 5d). The biotite and granite gneisses are ferroan, while the biotite granite and charnockite are essentially magnesian (Figure 5e). The magnesian nature of the biotite granite and charnockite is due to low $FeO_{total}/(FeO_{total} + MgO)$ and SiO_2 relative to the gneisses. All the rocks are calcic as shown by the $K_2O + Na_2O - CaO$ versus SiO_2 plot ([21]) (Figure 5f).

The granite gneiss, biotite gneiss, biotite granite and charnockite of the Akungba-Akoko area plot within the igneous field on the TiO_2 versus SiO_2 discrimination diagram [22] (Figure 6a). This suggests that the granite gneiss and biotite gneiss of the area are orthogneisses and are formed by metamorphism of igneous protoliths, and the biotite granite and charnockite are of igneous origin. The moderate to high silica contents, K/Rb values (<283), sub-alkalinity and I-type peraluminous nature of the biotite granite, charnockite and biotite gneiss indicate that they are I-type granitoids. This suggests that the biotite granite, the charnockite and the igneous protoliths of the biotite gneiss are formed from crustal igneous-sourced melt(s) [21, 23, 24]. The igneous protoliths of the granite gneiss were probably formed from shallow crustal or sedimentary-sourced melt(s) as indicated by its S-type peraluminous character, occasional appearance of garnets and other

Al-silicate (especially muscovite) in its mineralogy as well as presence of quartzite inclusions in the rock at some locations.
Tectonic discrimination of Akungba-Akoko rocks revealed that they are all volcanic arc granitoids (Figure 6b) suggestive of rocks formed during a phase of magmatic activity related to collision and subduction [20, 25].

Conclusion

This study discussed the petrology, mineralogy, petrochemistry and petrogenesis of the Basement Complex rocks around Akungba-Akoko. The area is underlain mainly by migmatite, granite gneiss, biotite gneiss, biotite granite and charnockite. The gneisses in the area are orthogneisses formed by metamorphism of igneous protoliths of granitic composition. The biotite granite and charnockite are of igneous/magmatic origin. The biotite granite, charnockite and the igneous protoliths of the biotite gneiss were formed from crustal igneous-sourced melt(s), while the igneous protoliths of the granite gneiss were probably derived from shallow crustal or sedimentary-sourced melt(s). These basement rocks are volcanic arc granitoids formed during a phase of magmatic activity related to collision and subduction.

Acknowledgements

The authors wish to thank Mr. Adedibu Sunny Akingboye for his field assistance and comments on the manuscript of this paper. The National Geosciences Research Laboratory, Kaduna, Nigeria, and the Department of Geology, University of Ibadan, Nigeria, are also appreciated for facilitating ED-XRF and petrographic analyses of the samples, respectively.

References

[1] Kroner, A., Ekwueme, B.N., Pidgeon, R.T. (2001): The Oldest Rocks in West Africa: SHRIMP Zircon Age for Early Archean Migmatitic Orthogneiss at Kaduna, Northern Nigeria. *The Journal of Geology*, 109, pp. 399–406.

[2] Ukwang, E., Ekwueme, B.N. (2009): Geochemistry and geotectonic study of granitic rocks southwest Obudu plateau, southeastern Nigeria. *Journal of Mining and Geology*, 45(1), pp. 73–81.

[3] Woakes, M., Rahaman, M.A., Ajibade, A.C. (1987): Some Metallogenetic Features of the Nigerian Basement. *Journal of African Earth Sciences*, 6(5), pp. 655–664.

[4] Oyawoye, M.O. (1964): The Geology of the Nigerian Basement Complex. *Journal of Nigerian Mining, Geology and Metallurgical Society*, 1(2), pp. 87–103.

[5] Rahaman, M.A. (1976): Review of the Basement Geology of Southwestern Nigeria. In: *Geology of Nigeria*, Kogbe, C.A. (ed.). Elizabethan Publ. Co.: Lagos, pp. 41–48.

[6] Rahaman, M.A. (1988): Recent advances in the study of the Basement Complex of Nigeria. In: *Precambrian Geology of Nigeria*, Oluyide, P.O., Mbonu, W.C., Ogezi, A.E.O., Egbuniwe, I.G., Ajibade, A.C., Umeji, A.C. (eds.). Geological Survey of Nigeria Publication: Kaduna, pp. 11–43.

[7] Odeyemi, I.B. (1981): A review of the Orogenic Events in the Basement Complex of Nigeria, West Africa. *Geologische Rundschau.*, 70(3), pp. 897–909.

[8] Elueze, A.A. (1986): Petrology and gold mineralisation of the amphibolite belt, Ilesha area, SW Nigeria. *Geology en Mgnbouw*, 65, pp. 189–195.

[9] Obiora, S.C. (2012): Chemical Characterization and Tectonic Evolution of Hornblende-Biotite Granitoids from the Precambrian Basement Complex around Ityowanye and Katsina-Ala, Southeastern Nigeria. *Journal of Mining and Geology*, 48(1), pp. 13–29.

[10] Jimoh, O.A., Ariffin, K.S., Hussin, H.B., Habeeb, A.A. (2016): Characterization and Assessment of Okpella Metacarbonate deposit in Nigeria. *Carbonates Evaporites*, pp. 1–12.

[11] Ekwueme, B.N. (1990): The nature and distribution of Archaean in Nigeria. In: *Third International Archaean Symposium*, Perth, Australia, pp. 99–101.

[12] Dada, S.S. (2016): Challenges of unresolved issues of Mapping, Nomenclature, Dating, Mineralization Settings and Characterization of Nigeria's Basement Geology. In: *52nd Ann. Int. Conf. Nig. Min. Geosci. Soc.*, Ilorin, Nigeria.

[13] Rahaman, M.A., Ocan, O. (1988): The nature of granulite facies metamorphism in Ikare area, southwestern Nigeria. In: *Precambrian Geology of Nigeria*, Oluyide, P.O., Mbonu, W.C., Ogezi, A.E.O., Egbuniwe, I.G., Ajibade, A.C., Umeji, A.C. (eds.). Geological Survey of Nigeria Publication: Kaduna, pp. 157–163.

[14] Streckeisen, A.L. (1976): To each Plutonic Rock its proper Name. *Earth Sciences Review*, 12 p.

[15] Streckeisen, A.L. (1974): How should charnockitic rocks be named? In: *Geologie des Domaines Cristallins*, Belliere, J., Duchesne, J.C. (eds.). Vol. Centenary Societe Geologique de Belgique: Liege. pp. 349–360.

[16] Rudnick, R.L., Gao, S. (2005): Composition of the continental crust. In: *The Crust. vol. 3, Treatise on Geochemistry,* Holland, H.D., Turekian, K.K. (eds.). Oxford, Elsevier: Pergamon.

[17] Irvine, T.N., Baragar, W.R.A. (1971): A guide to the chemical classifications of the common volcanic rocks. *Canadian Journal of Earth Sciences*, 8, pp. 523–548.

[18] Richwood, P.C. (1989): Boundary lines within petrologic diagrams which use oxides of major and minor elements. *Lithos*, 22, pp. 247–263.

[19] Maniar, P.D., Piccoli, P.M. (1989): Tectonic discrimination of granitoids. *Geological Society of America Bulletin*, 101, pp. 635–643.

[20] Dombrowski, A., Henjes-Kunst, F., Hohndorf, A., Kroner, A., Okrusch, M., Richter, P. (1995): Orthogneisses in the Sperssart Crystalline Complex, north-west Bavaria: Silurian granitoid magmatism at an active continental margin. *Geologische Rundschau*, 84, pp. 399–411.

[21] Frost, B.R., Barnes, C.G., Collins, W.J., Arculus, R.J., Ellis, D.J., Frost, C.D. (2001): A geochemical classification for granitic rocks. *Journal of Petrology*, 42, pp. 2033–2048.

[22] Tarney, J. (1972): Petrology, Mineralogy and Geochemistry of the Farkland Plateau Basement Rocks. *Site 330 Deep Sea Drilling Project Initial Report*, 36, pp. 893–921.

[23] Taylor, S.R., McLennan, S.M. (1981): The composition and evolution of the continental crust: rare earth elements evidence from sedimentary rocks. *Philosophical Transactions of the Royal Society of London*, 301, pp. 381–399.

[24] Adegbuyi, O., Ogunyele, A.C., Odindu, M., Erinfolami, T.G. (2017): Geochemical Characteristics and Petrogenesis of Basement Rocks in Idoani Area, Ondo State, Southwestern Nigeria. *International Journal of Advanced Geosciences*, 5(2), pp. 102–108.

[25] Pearce, J.A., Harris, N.B., Tindle, A.G. (1984): Trace element discrimination for the tectonic interpretation of granitic rocks. *Journal of Petrology*, 25, pp. 956–983.

Original scientific paper

Received: Dec 31, 2018
Accepted: Feb 26, 2019
DOI: 10.2478/rmzmag-2019-0011

Heavy Mineral Distribution in the Lokoja and Patti Formations, Southern Bida Basin, Nigeria: Implications for Provenance, Maturity and Transport History

Razširjenost težkih mineralov v formacijah Lokoja in Patti: poreklo, zrelost in zgodovina transporta

Bankole, S. I.*, Akinmosin, A., Omeru, T. and Ibrahim, H. E.
University of Lagos, Faculty of Science, Department of Geosciences, Akoka, Lagos, Nigeria
*sbankole@unilag.edu.ng

Abstract

Heavy mineral component of 13 samples from the Lokoja and Patti Formations, Bida Basin have been studied for their textural characteristics, compositional abundance, maturity and provenance determinations. The suite of heavy minerals encountered is classified as opaque and non-opaque constituents. The non-opaque components include zircon, tourmaline, rutile, garnet, staurolite, epidote, kyanite, titanite, lawsonite, cassiterite, sillimanite, hornblende, hypersthene and andalusite. The assemblage is generally dominated by zircon and tourmaline in the two formations. The constituent heavy minerals identified are dominated by ultra-stable and stable classes, whereas the ZTR indices indicate mineralogical immaturity coupled with textural immaturity of the constituent grains. This suggests the possible dominance of chemical weathering of the source rock. The suites of minerals recovered have been linked to both metamorphic and non-metamorphic crystalline rock origins.

Key words: heavy mineral, zircon, tourmaline, mineralogical analysis

Povzetek

Komponente težkih mineralov trinajstih vzorcev iz formacij Lokoja in Patti v bazenu Bida so bile preiskovane glede na teksturne lastnosti, pogostost, zrelost in določitve porekla. Nabor proučevanih težkih mineralov je razvrščen na neprozorne in prozorne sestavne dele. Prozorne komponente vključujejo cirkon, turmalin, rutil, granat, stavrolit, epidot, kianit, titanit, lavsonit, kasiterit, silimanit, rogovačo, hipersten in andaluzit. V sestavi formacij večinoma prevladujeta cirkon in turmalin. Med težkimi minerali prevladujejo ultra stabilni in stabilni razredi, medtem ko indeksi ZRC izkazujejo mineraloško nezrelost, povezano s teksturno nezrelostjo sestavnih zrn. To nakazuje na mogočo prevlado kemijskega preperevanja matične kamnine. Pridobljeni minerali so povezani tako z metamorfnim kot ne metamorfnim kristalnim nastankom.

Ključne besede: težki minerali, cirkon, turmalin, mineraloška analiza

Introduction

The Intracratonic Bida Basin (Nupe or Middle Niger Basin) is one of the inland sedimentary basins of Nigeria [1], located roughly at the mid-central Nigeria (Figure 1). It is a northwest-southeast trending basin contiguous with the Anambra Basin. It extends from Kontagora, Niger State to Dekina, Benue State with a length of about 400 km and a width approximating 160 km [2]. Sediment accumulation in the basin commenced from Campanian and continued through the Maastrichtian [3] with fills ranging between 3.5 and 4.5 km thickness [4, 5] at the central part of the basin. Several research papers have been published on the evolution and stratigraphy of the basin.

Rift origin in connection with the aulacogen Benue Trough of Nigeria consequence to the separation of the South American and African continents in the Late Jurassic has been suggested for the Bida Basin [6–8]. This rifting resulted in the generation of series of horst and graben structures that characterizes the floor of the Bida Basin.

On the basis of geographical and lateral facies variation, the basin has been divided into the northern and southern sub-basins (Figure 1). In the southern Bida sub-basin, the oldest sedimentary unit, lying non-conformably on the Precambrian to Lower Paleozoic crystalline basement complex is the fluviatile Lokoja Formation (Figure 2). Patti Formation conformably overlies the Lokoja Formation (Figure 3). Observations at the base of Agbaja Plateau and also at the Ahoko Village mine indicate mixed marine and continental deposition environments for the Patti Formation. Literature accounts revealed that the formation consists of sandstones, siltstones, mudstones and shale in intercalation with bioturbated ironstones [9, 10]. The marine series of the Patti Formation is exposed at an abandoned mine in Ahoko Village along Lokoja-Abuja Highway. This unit, which constitutes part of the shale member of the Patti Formation has been extensively reviewed, described and reported by several authors [8, 10, 11–13]. The Agbaja Ironstone Formation caps the sequence of sediments in the southern Bida Sub-basin. Agbaja Formation is an intercalation of claystones, sandstones and oolitic/massive ironstones. Ladipo et al. [14] interpreted the sequence of the formation as abandoned channel sands and overbank deposits with marine influence resulting in the formation of the massive concretionary and oolitic ironstones.

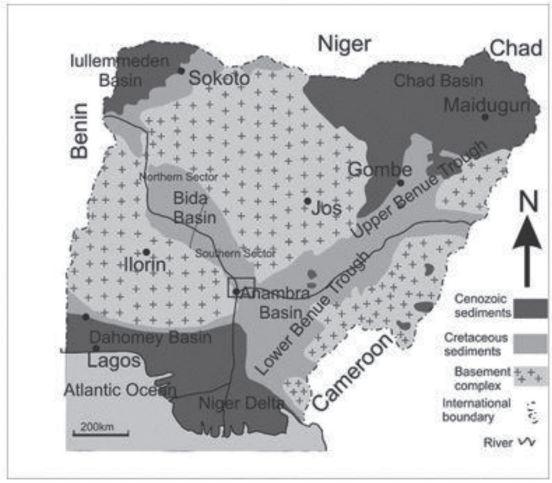

Figure 1: *Geological map of Nigeria. Box indicates the study area.*

Figure 2: *Section of the Lokoja Formation exposed at Okumi, along the Lokoja-Abuja Highway.*

In the present study, we report on the distribution and concentration of heavy minerals in the Lokoja and Patti Formations. On the basis of these, attempt is made to infer the provenance, maturity and transport history of the sediments of the formations. Detrital sediments are products of pre-existing igneous, metamorphic and also sedimentary rocks. These rocks are composed of diverse detrital minerals with some being classified as placer minerals. The latter are generally highly mechanically resistant and survive the usual complex transportation processes from source areas to the depocen-

Figure 3: *Section of the Patti Formation exposed near the Agbaja Plateau along Lokoja – Agbaja road. The capping rock (uppermost section) in this outcrop is the lower unit of Agbaja Ironstone Formation.*

ters. These characteristics have allowed the use of heavy minerals in the study of sediment provenance, maturity and transport history. This method has been widely applied in fluvial [15, 16], coastal-shallow marine [17, 18], deep marine [19] depositional environments.

Materials and Methods

Materials

In total, 13 sediment samples (six from Lokoja Formation and seven from Patti Formation) were subjected to heavy mineral analysis. The analysis was carried out at the Sedimentological Laboratory, Department of Geosciences, University of Lagos, Nigeria.

Methods

Heavy mineral analysis in this study followed the procedure of Suzuki [20] and Mange and Maurer [21] for heavy mineral separation. The heavy liquid, Bromoform (CHBr3) with a density of 2.9 g/cc and viscosity of 0.068 poises was used. The samples were air-dried for a week to dispel any moisture as they were collected during the rainy season. Thereafter, the sediments were gently disaggregated by squeezing between fingers and filter paper or mortar and pestle in the case of hard samples to liberate individual grains. Each sample of 70 g was weighed and sieved to obtain 62.5–500 microns size grains. The individual sample was then poured into the bromoform and stirred thoroughly to free the samples of air bubbles. The particles were allowed to settle for about 20 minutes, stirring periodically to prevent the particles from adhering to funnel wall. The heavy crop was repeatedly washed in excess acetone and distilled water and air-dried and labelled. In all, 13 permanent mounts were made on slides using coupled resin. Mineral identification on the basis of their optical properties as proposed by Mange and Maurer [21] and Lindholm [22] was conducted on the samples.

More than 100 grains were counted from each slide for statistical analysis. Rock fragments, unidentifiable grains as well as authigenic and opaque minerals were excluded from the total sum to obtain uniform, comparable data on transparent assemblages for the characterization of mineralogical provinces. The sum of transparent minerals was recalculated to a value of 100% and the abundance of each heavy mineral species was scaled accordingly. The "ZTR" index which is the combined percentage of zircon, tourmaline and rutile among the non-opaque heavy minerals, omitting micas and authigenic species was calculated using [23] formula below:

$$ZRT\ index = \frac{Zircon + Tourmaline + Rutile}{Non - opaque} \times 100$$

ZTR index was calculated for the samples to ascertain their mineralogical maturity. According to Hubert [23], ZTR index <75% implies immature to sub-mature sediments and ZTR >75% indicates mineralogically matured sediments.

Results and Discussions

Results

Heavy mineral concentration in the Lokoja and Patti Formations is classified into opaque and

non-opaque constituents. The opaque components generally referred to as iron stained heavy minerals require further chemical analysis to allow investigation under petrographic microscope. This chemical analysis, however, is beyond the scope of the present investigation and no further serious attention apart from statistical consideration is accorded to this class of heavy minerals herein. The recovered non-opaque components common to the two formations include the following: zircon, tourmaline, rutile, garnet, staurolite, epidote, kyanite, titanite, lawsonite, cassiterite, sillimanite, hornblende, hypersthene and andalusite (Plates 1–14). Kyanite, cassiterite, hypersthene, staurolite, hornblende and lawsonite show rare occurrences in the Lokoja Formation, except in a sample (Lok2 S6) that has significant amount of hornblende. Also, Kyanite, titanite, hornblende and garnet show rare occurrences in the Patti Formation, kyanite occurs only in PAT S7 sample. The proportion of heavy mineral recovered to the volume of sediment analysed is generally low and may not support any significant economic prospect. Information on the proportion of the heavy minerals recovered from the two formations is provided in Tables 1 and 2. Also, Tables 3 and 4 show the calculated ZRT% index results.

The summary of the identification/classification criteria and the significant characteristics of each of the recovered heavy mineral are as follow:

***Zircon*:** Zircon grains (Plates 2, 3 and 6) are prismatic, rounded to sub-rounded and sometimes contains fluid and mineral inclusions. Prismatic grains frequently showed zonation identified by fine bands parallel to the crystal boundary (Plate 2). The colourless varieties are more in abundance than the coloured varieties. The grains are easily identifiable owing to their very high relief and they are surrounded by black halo (Plates 2, 3 and 6). They show weak pleochroism and strong birefringence.

***Tourmaline*:** Tourmaline grains (Plates 1, 2, 4 and 5) are prismatic, elongated, oval-shaped, spherical, euhedral, sub-hedral to irregular in shapes, with terminations at one or both ends of prismatic variety. Moderate relief, mineral inclusions (Plate 9) and overgrowths were frequently observed (Plate 1). Colours vary from pale to pink, dark green (Plate 4), pale yellowish, dark brown (Plate 4), very dark (almost opaque, may be iron bearing; Plates 1 and 5) and sometimes colourless. Colour zoning is frequent, pleochroism sharp and distinctive. Varicoloured varieties were also present (one portion of the grain displays striking different shades to the other).

***Rutile*:** Rutiles (Plate 7) appeared as small and sub-rounded slender prisms with well-developed terminations or breakage patterns. A thick halo surrounds the grains because of their extremely high refractive indices. Grains are mostly brownish red to brownish black in colours and show distinct pleochroism (Plate 7).

***Kyanite*:** Kyanite grains (Plates 8 and 12) are angular, or prismatic, dominantly colourless, weakly pleochroic (uneven coloured pleochroism) and exhibit characteristic cross-fractures and step-like features (Plates 8 and 12). The step-like uneven thickness resulted in a spectacular arrangement of the interference colours appearing in blue and grey on thicker and thinner parts, respectively.

***Sillimanites*:** Sillimanites (Plates 9, 11 and 13) are long, slender, prismatic or irregular in shapes. Sillimanites show distinct cleavage, pleochroic (pale brown to pale yellow), parallel extinction, shows brilliant second- and third-order interference colours with yellow, green and pink as a dominant shades; slight twinkling is noticeable on rotation.

Andalusite: Andalusite (Plates 2–4, 6 and 7), mostly colourless and frequently enclose carbonaceous impurities. The rare manganoan variety, viridine which is green in colour was observed (Plate 4). They occur as prismatic, sub-rounded to angular or of irregular morphology; cleavage traces are poorly displayed. Some grains are non-pleochroic, whereas others display inhomogeneous pattern of pleochroism. Due to their irregular shape and uneven thickness, they display disorderly patterned interference colours. Weak interference colours are second-order orange and greenish blue (Plates 2–4, 6, and 7).

***Garnet*:** Garnets (Plates 1, 3–6), easily identifiable because of their high relief and isotropic nature are euhedral, rounded, sub-rounded or irregular grains with uneven or conchoidal

Table 1: *Proportion (number of grains) of heavy minerals concentration in the sediments of Lokoja Formation.*

Sample Name	S/N	Zrn	Tur	Rt	Grt	St	Ep	Sil	Tt	And	Ky	M	Cst	Hbl	Hyp	Lws	Opq
LOK1 S1	1	4	3	1	4	-	4	-	4	-	-	4	-	-	-	-	22
LOK1 S2B	2	5	13	1	1	-	8	11	2	7	3	9	-	-	-	3	236
LOK1 S4B	3	5	4	3	4	1	2	2	-	5	-	4	-	-	-	-	142
LOK2 S2	4	11	9	3	8	1	5	3	3	1	-	6	-	1	1	-	253
LOK2 S6	5	6	3	4	2	-	3	-	-	3	-	-	4	7	1	-	245
LOK2 S8	6	69	5	12	10	2	10	8	-	3	-	2	-	-	-	3	1560
TOTAL		100	37	24	29	4	32	24	9	19	3	25	4	8	2	6	2458

Note: Zrn = Zircon; Tur = Tourmaline; Grt = Garnet; St = Staurolite; Ep = Epidote; Sil = Sillimanite; Tt = Titanite; And = Andalusite; Ky = Kyanite; Opq = Opaque, Hbl = Hornblende; Hyp = Hypersthene; Cst= Cassiterite; Lst = Lawsonite; M= Mica. S/N: Serial Number.

Table 2: *Proportion (number of grains) of heavy minerals concentrations in the sediment samples from Patti Formation.*

CODE	S/N	Zrn	Tur	Rt	Grt	St	Ep	Sil	Tt	And	Ky	M	Hbl	Opq
PAT S1B	1	27	10	1	-	4	2	1	1	3	-	-	1	303
PAT S2B	2	13	11	2	-	-	4	-	3	-	-	8	3	54
PAT S5B	3	4	4	2	1	6	-	2	-	3	-	4	-	201
PAT S7	4	10	9	2	4	13	10	8	4	8	2	-	4	1352
PAT S13	5	-	-	-	-	-	-	-	-	-	-	-	-	-
PAT S16	6	-	-	-	-	-	-	-	-	-	-	-	-	-
PAT S17B	7	3	4	8	1	-	-	2	-	4	-	-	-	2420
TOTAL		57	38	15	6	23	16	13	8	18	2	12	8	4330

fractures. Colours vary from pinkish brown, pale red, pale pink to colourless.

***Titanite*:** Titanite (Plate 12) grain has a high resinous lustre. Relief shows a slight twinkling on rotation of the stage. The grain has a weak pleochroism and good cleavage. High-order interference colours in golden yellow and yellowish white.

***Staurolite*:** Staurolite (Plates 4, 11 and 14) occurs as irregular or angular grains. Colour ranges from pale yellow, golden yellow to dark yellowish brown. They exhibit distinct pleochroism (colourless to different shades of yellow).

***Epidote*:** Epidote (Plates 2, 6 and 8) occurs as irregularly shaped grains, yellowish green to green coloured with fairly high relief. They exhibit distinct pleochroism (colourless, pale yellow, yellowish green).

Table 3: *ZTR maturity index and individual percentage mineral of the sediment samples of Lokoja Formation.*

CODE	Zrn	Tur	Rt	Grt	St	Ep	Sil	Tt	And	Ky	M	Cst	Hbl	Hyp	Lst	TOTAL NON-OPAQUE	Z+T+R	ZTR% INDEX
LOK1 S1	4	3	1	4	-	4	-	4	-	-	4	-	-	-	-	24	8	33.3
LOK1 S2B	5	13	1	1	-	8	11	2	7	3	9	-	-	-	3	63	19	30.2
LOK1 S4B	5	4	3	4	1	2	2	-	5	-	4	-	-	-	-	30	12	40.0
LOK2 S2	11	9	3	8	1	5	3	3	1	-	6	-	1	1	-	52	23	44.2
LOK2 S6	6	3	4	2	-	3	-	-	3	-	-	4	7	1	-	33	13	39.4
LOK2 S8	69	5	12	10	2	10	8	-	3	-	2	-	-	-	3	124	86	69.4
TOTAL	100	37	24	29	4	32	24	9	19	3	25	4	8	2	6	326	161	49.4
%	30.7	11.3	7.4	8.9	1.2	9.8	7.4	2.8	5.8	0.9	7.7	1.2	2.5	0.6	1.8	Individual mineral% abundance		

Average ZTR% Index = 42.8%
Total Opaque = 2458
Total Non-opaque = 326
Total Non-opaque excluding micas = 301

Table 4: *ZTR maturity index and individual percentage mineral of the sediment samples of Patti Formation.*

CODE	Zrn	Tur	Rt	Grt	St	Ep	Sil	Tt	And	Ky	M	Cst	Hbl	Hyp	Lst	TOTAL NON-OPAQUE	Z+T+R	ZTR% INDEX
PAT S1B	27	10	1	-	4	2	1	1	3	-	-	-	1	-	-	50	38	76.0
PAT S2B	13	11	2	-	-	4	-	3	-	-	8	-	3	-	-	44	26	59.1
PAT S5B	4	4	2	1	6	-	2	-	3	-	4	-	-	-	-	26	10	38.5
PAT S7	10	9	2	4	13	10	8	4	8	2	-	-	4	-	-	74	21	28.4
PAT S17B	3	4	8	1	-	-	2	-	4	-	-	-	-	-	-	22	15	68.2
TOTAL	57	38	15	6	23	16	13	8	18	2	12	-	8	-	-	216	110	50.9
%	26.4	17.6	6.9	2.8	10.6	7.4	6.0	3.7	8.3	0.9	5.6	-	3.7	-	-	Individual mineral% abundance		

Average ZTR% Index = 54.0%
Total Opaque = 4330
Total Non-opaque = 216
Total Non-opaque excluding micas = 204

Discussion

The percentage proportions of the non-opaque heavy mineral constituents (Figures 4 and 5) in Lokoja and Patti Formations show the dominance of zircon. Tourmaline is the second most abundant of the recovered minerals. Epidote comes next in the Lokoja Formation with staurolite in the Patti Formation. Epidote is present

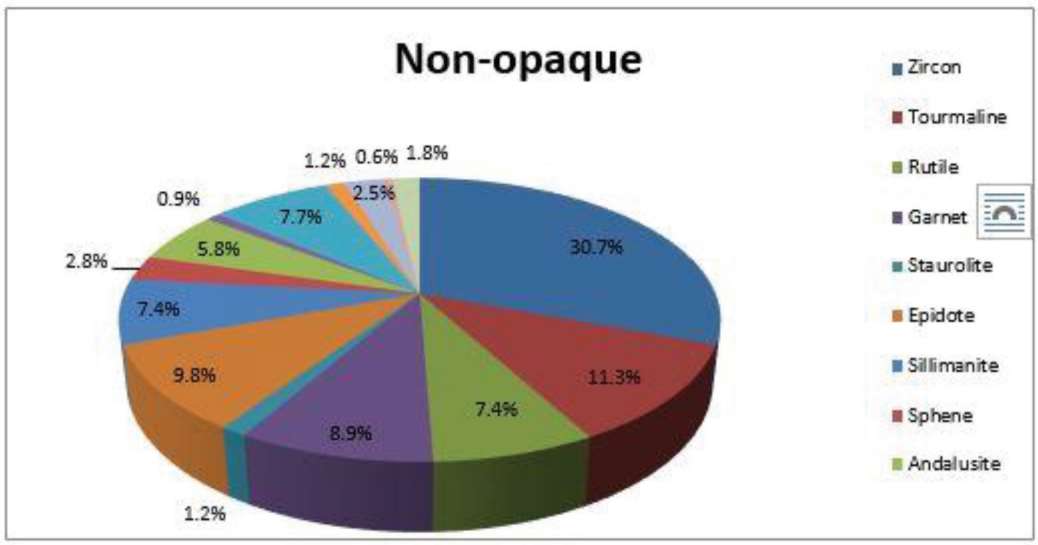

Figure 4: *Overall percentage proportion of each non-opaque heavy mineral in the Lokoja Formation.*

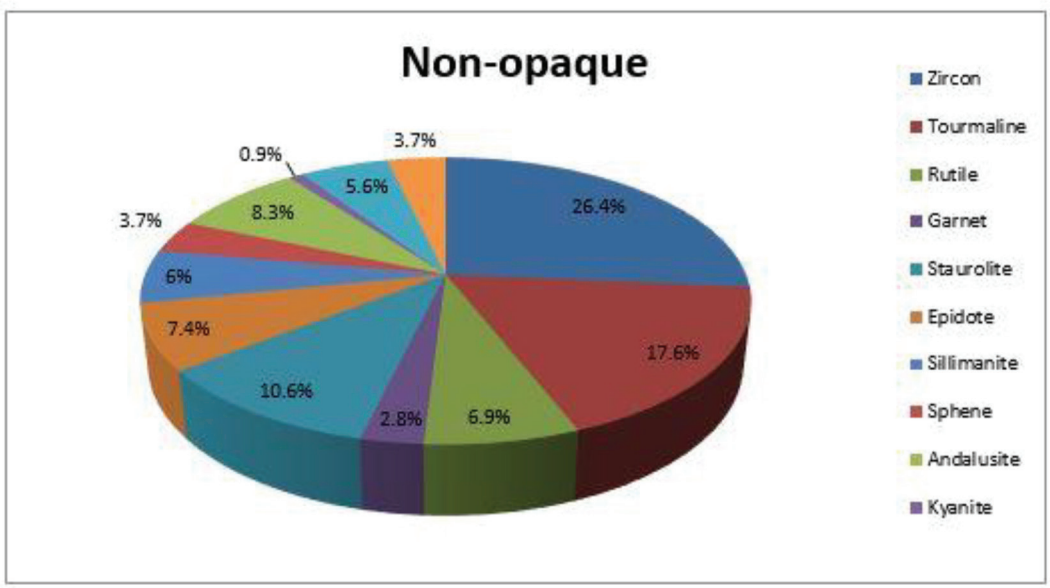

Figure 5: *Overall percentage proportion of each non-opaque heavy mineral in the Patti Formation.*

in all the samples of the Lokoja Formation but only in three (3) samples of the Patti Formation. Staurolite was recovered in three (3) samples each of the Lokoja and Patti Formations. The minerals with the lowest percentage proportion are cassiterite, staurolite, kyanite and hypersthene in the Lokoja Formation, whereas the lowest in the Patti Formation is kyanite. Cassiterite, lawsonite and hypersthene are totally absent in the Patti Formation. In the heavy mineral stability index of [24,25], hornblende, hypersthene and andalusite are classified as unstable, epidote, kyanite, garnet, sillimanite, titanite, lawsonite, cassiterite as moderately stable, garnet, staurolite as stable and zircon, tourmaline, rutile as ultra-stable minerals. Consequent to the proportion of the constituent heavy mineral in the studied sections, the sediments of the Lokoja and Patti Formations are considered generally stable as they are dominated by ultra-stable and stable minerals.

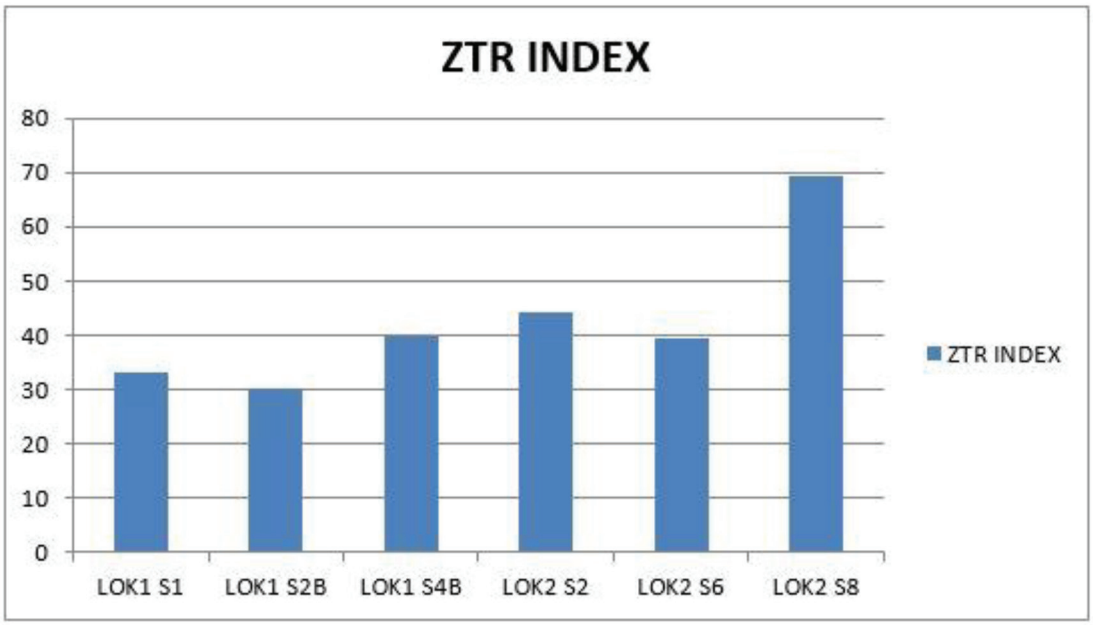

Figure 6: *Bar chart of ZTR index of each selected samples of Lokoja Formation.*

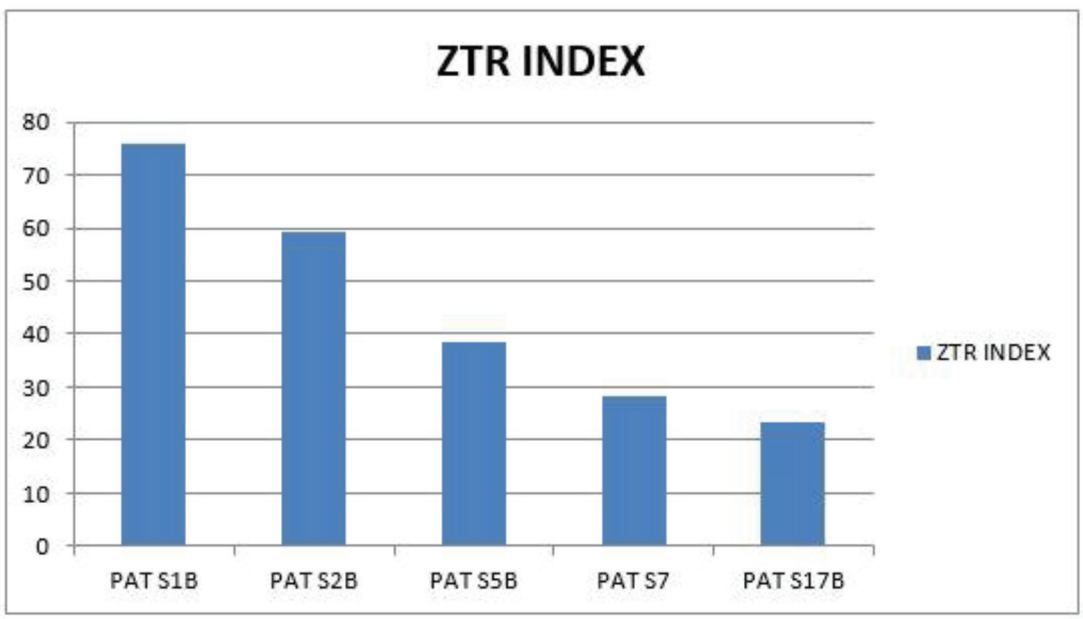

Figure *7: Bar chart of ZTR index of each selected samples of Patti Formation.*

The calculated ZTR% index for the two formations ranges from 30.2% to 69.4% in the Lokoja Formation (Figure 6), whereas in the Patti Formation, it ranges from 28.4% to 76.0% (Figure 7). All, except one sample from the Lokoja Formation, have ZTR% index of <50%. This low ZTR index indicates that the samples of the Lokoja Formation are mineralogically immature. The ZTR index of the Patti Formation shows only slight improvement with two samples having ZTR >50% and three having ZTR% index of <50%. The mean percentage of ZTR index for Lokoja Formation is 42.8%, whereas that of Patti Formation is 54.0%. These show the comparative mineralogical maturity advan-

tage of the sediments of the Patti Formation over their Lokoja counterparts.

Generally, very few rounded grains were encountered in all the samples studied (Plates 1–14). Most of the grains are either angular or sub-angular, suggesting that the sediments are from nearby sources and may not have been transported far away from weathering location. Hence, indicating textural immaturity of the sediments of both formations.

The abundance of ultra-stable and stable heavy minerals in an assemblage of texturally immature sediments grains (angular to sub-angular) is suggestive of the prevalence of chemical weathering of the source rocks contributing the heavy minerals to the studied formations.

Based on the constituent minerals in the studied sediments, mixed source ranging from high- to low-grade metamorphic and non-metamorphic sources is suggested. The possibility of contribution from low-grade metamorphic and non-metamorphic sources is indicated with dominance of zircon and tourmaline [26] in the two formations. Mange and Maurer [21] have linked the presence of lawsonite, hypersthene, hornblende, cassiterite, kyanite, andalusite, sillimanite, titanite, epidote, staurolite, garnet to high-grade metamorphic terrain. Also, Diekmann and Kuhn [27] attributed the dominance of low maturity heavy mineral such as green hornblende and garnet to high-grade metamorphic source. Rutile is generally linked to high-grade metamorphic source.

Conclusion

Heavy mineral analysis of both Lokoja and Patti Formations shows the predominance of non-rounded heavy minerals suites indicating short transport history from the sediment source, probably the southwest and north central Basement Complex terrains. The ZTR indices gave a general evidence of immature sediment suites for the Lokoja and Patti Formations with the latter being more matured than the former. Furthermore, the sediments of both formations are stable as they are dominated by ultra-stable and stable minerals. An assemblage of stable heavy minerals in a suite of texturally immature sediments validates the prevalence of chemical weathering of the source rocks which contributed to Lokoja and Patti Formations. The source of the sediments from both formations is interpreted to be of igneous and metamorphic terrain as indicated by the dominance of zircon, tourmaline, rutile, mica and opaque components.

References

[1] Obaje, N.G., Moumouni, A., Goki, N.G., Chaanda, M.S. (2011): Stratigraphy, Paleogeography and hydrocarbon resource potentials of the Bida Basin in north-central Nigeria. *Journal of Mining and Geology*, 47(2), pp. 97–114.

[2] Nwajide, C.S. (2013): *Geology of Nigerian Sedimentary Basins*. Awka: CSS Bookshop, pp. 227–340.

[3] Wright, J.B., Hastings, D., Jones, W.B., Williams H.R. (1985): *Geology and Mineral Resources of West Africa*. London: George Allen and Urwin, pp. 90–120.

[4] Udensi, E.E., Osasuwa, I.B. (2004): Spectra determination of depths to magnetic rocks under the Nupe Basin, Nigeria. *Nigeria Association of Petroleum Explorationists Bulletin*, 17, pp. 22–37.

[5] Ojo, S.B. (1984): Middle Niger Basin revisited: magnetic constraints on gravity interpretations. In: *20th Conference of the Nigeria Mining and Geosciences Society*, Nsukka, pp. 52–53.

[6] King, L.C. (1950): Outline and distribution of Gondwanaland. *Geological Magazine*, 87, pp. 353–359.

[7] Kogbe, C.A. (1981): Geological interpretation of landsat imagery of part of central Nigeria. *Journal of Mining and Geology*, 28, pp. 66–69.

[8] Braide, S.K. (1992): Syntectonic fluvial sedimentation in the Central Bida Basin. *Journal Mining Geology*, 28, pp. 55–64.

[9] Olugbemiro, R.O., Nwajide, C.S. (1997): Grain size distribution and particle morphogenesis as signatures of depositional environments of Cretaceous (non-ferruginous) Facies in the Bida Basin, Nigeria. *Journal of Mining and Geology*, 33, pp. 89–101.

[10] Akande, S.O., Ojo O.J., Erdtmann B.D., Hetenyi, M. (2005): Paleoenvironments, organic petrology and rock-eval studies on source rock facies of the Lower Maastrichtian Patti Formation, Southern Bida Basin, Nigeria. *Journal of African Earth Sciences*, 41, pp. 394–406.

[11] Idowu, J.O., Enu, E.I. (1992): Petroleum geochemistry of some late Cretaceous shales from the Lokoja Sand-

stone of Middle Niger Basin, Nigeria. *Journal of African Earth Sciences*, 14, pp. 443–455.

[12] Ojo, O.J., Akande, S.O. (2006): Sedimentological palynological studies of the Patti Formation, southeastern Bida Basin, Nigeria: Implications for palaeoenvironment and palaeogeography. *Nigerian Association of Petroleum Explorationists Bulletin*, 19(1), pp. 61–77.

[13] Ojo, O.J., Akande, S.O. (2009): Sedimentology and depositional environments of the Maastrichtian Patti Formation, southeastern Bida Basin, Nigeria. *Cretaceous Research*, 30, pp. 1415–1425.

[14] Ladipo, O., Akande, S.O., Mucke, A. (1994): Genesis of ironstones from middle Niger sedimentary basin, evidence from sedimentological, ore microscopic and geochemical studies. *Journal of Mining Geology*, 30, pp. 161–168.

[15] Joshua, E.O., Oyebanjo, O.A. (2009): Distribution of heavy minerals in sediments of Osun River Basin, Southwestern Nigeria. *Research Journal of Earth Sciences*, 1(2), pp. 74–80.

[16] Sarma, J.N., Chutia, A. (2013): Petrography and heavy mineral analysis of Tipam Sandstones exposed on the Tipam Hill of Sita Kunda area, Upper Assam, India. *South East Asian Journal of Sedimentary Basin Research*, 1, pp. 28–34.

[17] Ramasamy, P., Karikalan, R. (2010): Distribution and percentage of heavy minerals in coastal geomorphological landforms in Palk Strait, southeast Coast of India. *Middle-east Journal of Scientific Research*, 5(1), pp. 49–53.

[18] Achab, M., Gutierrez Mas, J.M. (2009): Heavy minerals in modern sediments of the Bay Of Cadiz and the adjacent Continental Shelf (Southwestern Spain): Nature and Origin, *Journal of Marine Sciences*, 25(2), pp. 27–40.

[19] Grzebyk, J., Leszczynski, S. (2006): New data on heavy minerals from the Upper Cretaceous-Paleogene Flysch of the Beskid Slaski Mts. (Polish Carpathians). *Geological Quarterly*, 50, pp. 265–280.

[20] Suzuki, T. (1975): *Heavy minerals composition of the recent sediments in three different environments in geological survey of Japan*, part 1, 501 p.

[21] Mange, M.A., Maurer, H.F.W. (1992): *Heavy Minerals in Colour*. London: Chapman and Hall, 147 p.

[22] Lindholm, R.C. (1987): *A Practical Approach to Sedimentology*. London: Allen and Unwin, 279 p.

[23] Hubert J.T. (1962): A Zircon-tourmaline-rutile maturity index and interdependence of the composition of heavy minerals assemblages with the gross composition and texture of sediments. *Journal of Sedimentary Petrology*, 32, pp. 440–450.

[24] Pettijohn, F.J., Potter, P.E., Siever, R. (1973): *Sand and Sandstone*. New York: Springer Verlag, 618 p.

[25] Morton, A.C. (1985): *Heavy Minerals in Provenance Studies*. In: Provenance of Arenites, Zuffa, G.G (ed.). Dordrecht: Reidel, pp. 77–249.

[26] Deer, W.A., Howie, R.A., Zussman, J. (1992): *An Introduction to the Rock-Forming Minerals* (2nd edition). Essex: Longman, 696 p.

[27] Diekmann, B., Kuhn, G. (1999): Provenance and dispersal of glacial-marine surface sediments in the Weddell Sea and adjoining areas, Antarctica: ice-rafting versus current transport. *Marine Geology*, 158(1–4), pp. 209–231.

Appendix 1a

Plates 1-6

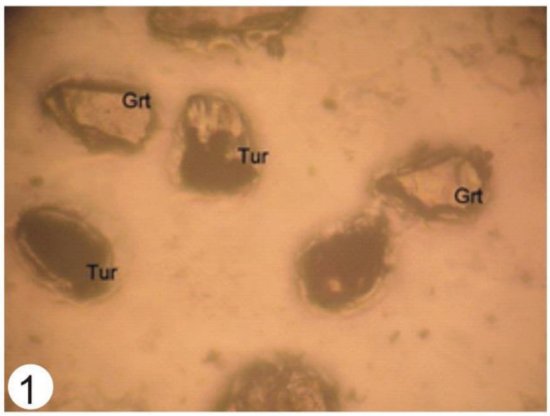

Sample LOK1 S1: Tourmaline (Tur) grains, the lower grain showing secondary growth (overgrowth), Garnet (Grt), Mag. X40

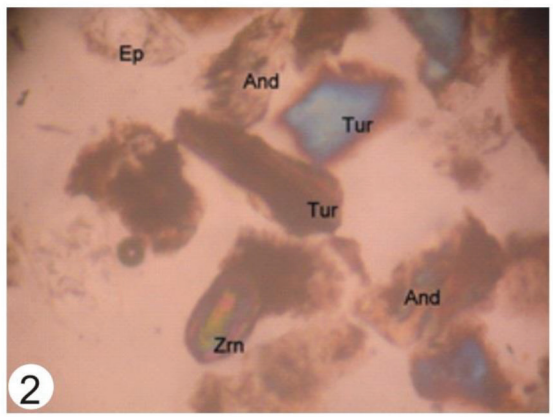

Sample LOK1 S2B: Epidote (Ep), Andalusite (And), Tourmaline (Tur) and Zircon (Zrn). Mag. X40

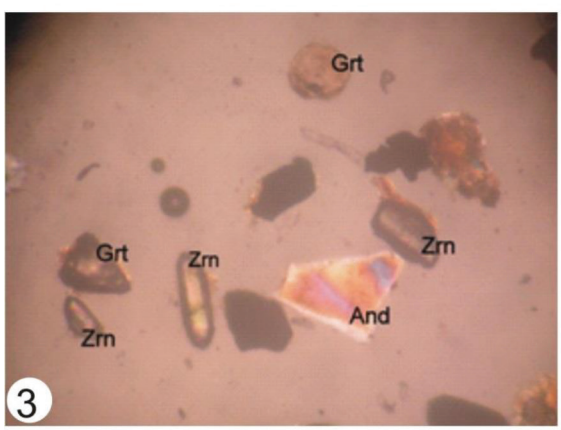

Sample LOK1 S4B: Zircon (Zrn), Garnet (Grt), Andalusite (And). Mag. X40

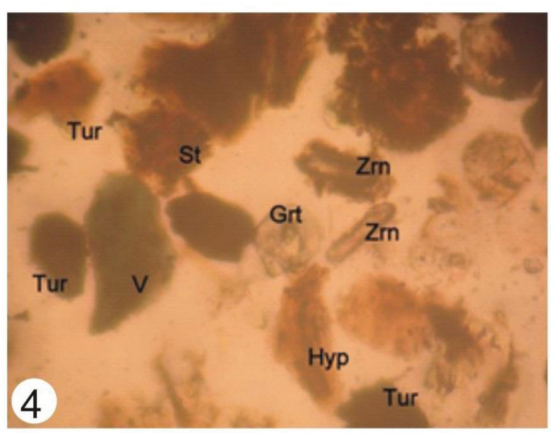

Sample LOK2 S2: Green coloured manganoan variety of Andalusite, Viridine (V), Staurolite (St), brown Tourmaline (Tur), Garnet (Grt), Hypersthene (Hyp), Zircon (Zrn). Mag. X40

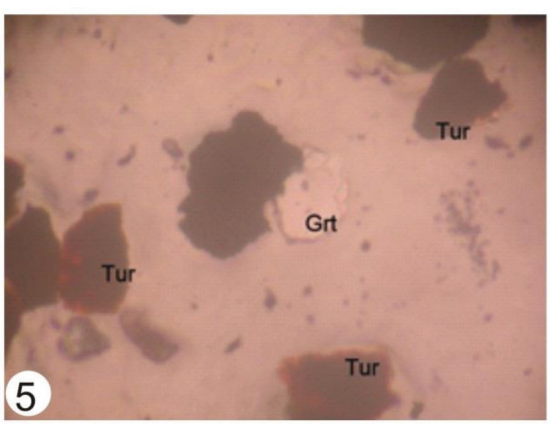

Sample LOK2 S6: Dark Tourmaline (Tur), Garnet (Grt). Mag. X40

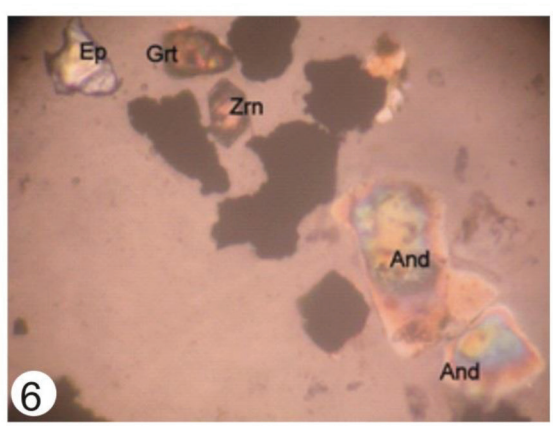

Sample LOK2 S8: Andalusite (And), Epidote (Ep), Zircon (Zrn), Garnet (Grt). Mag. X40

Appendix 1b

Plates 7-14

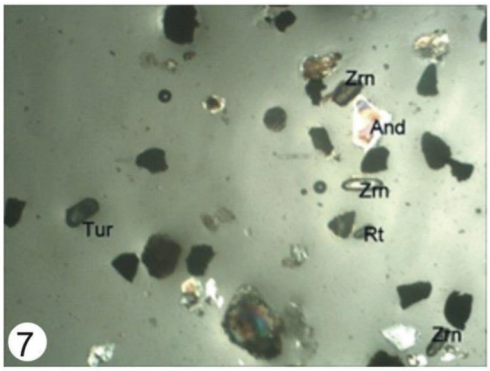

Sample LOK1 S4B: Tourmaline (Tur), Zircon (Zrn), Andalusite (And), Rutile (Rt). Mag. X10

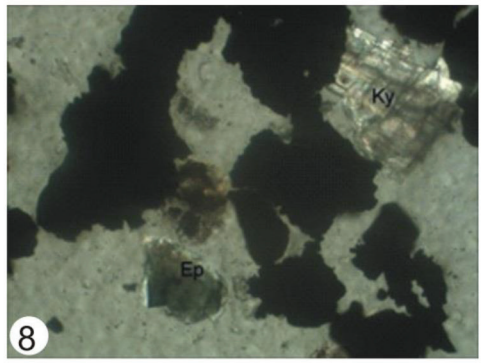

Sample LOK2 S8: Epidote (Ep), Kyanite (KY). Mag. X40

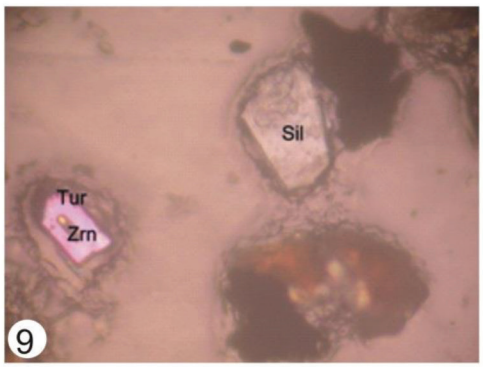

Sample PAT S1B: Sillimanite (Sil), Tourmaline (Tur) with zircon inclusion. Mag. X40

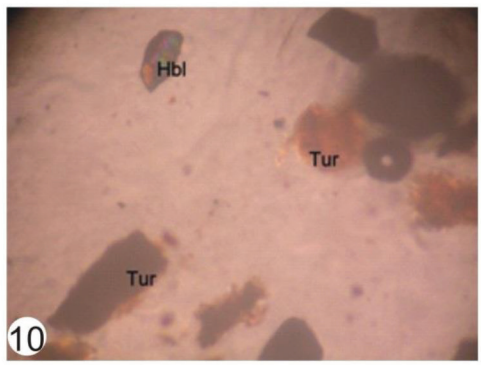

Sample PAT S2B: Hornblemde (Hbl), Tourmaline (Tur). Mag. X40

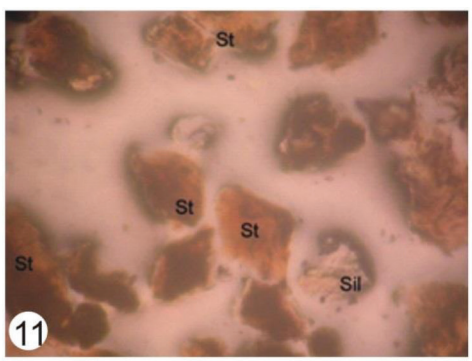

Sample PAT S5B: Staurolite (St), Sillimanite (Sil). Mag. X40

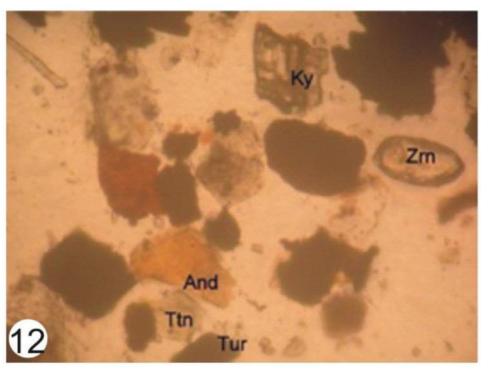

Sample PAT S7: Andalusite (And), Zircon (Zrn), Kyanite (Ky), Titanite (Ttn), Tourmaline (Tur), Mag. X40

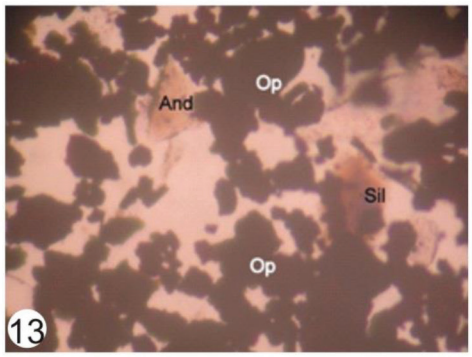

Sample PAT S17B: Andalusite (And), Sillimanite (Sil), Opaque minerals (Opq). Mag. X10

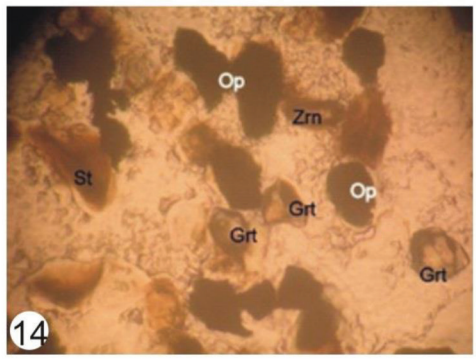

Sample PAT S1B: Staurolite (St), Garnet (Grt), Zircon (Zrn), Opaque minerals (Opq). Mag. X40

Original scientific paper

Received: Apr 08, 2019
Accepted: Nov 22, 2019
DOI: 10.2478/rmzmag-2019-0015

Assessment of Hydrogeological Potential and Aquifer Protective Capacity of Odeda, Southwestern Nigeria

Hidrogeološki potencial in ocena zaščitnih zmogljivosti vodonosnika na območju Odeda v Nigeriji

J.O. Aina*, O.O. Adeleke, V. Makinde, H.A. Egunjobi, P.E. Biere
Department of Physics, Federal University of Agriculture, Abeokuta, Nigeria
* johntemini20@gmail.com

Abstract

Hydrogeological assessment of groundwater resources was carried out with a view to evaluate the potential of the aquifers to provide portable water supply and access the distribution of electrical parameters of hydrogeologic units in some areas in Odeda, Ogun State, Nigeria. A geophysical survey using vertical electrical sounding (VES) with the Schlumberger electrode array, with half-current electrode spacing (AB/2) varying from 1 to 132 m was carried out at 30 different stations in the study area. The VES data were interpreted qualitatively and quantitatively. Three-to-five sub-surface layers consisting of topsoil, weathered layer consisting of clay, sandy clay, clayey sand and sand layers, and fractured/fresh basement were delineated. Layer resistivities and thicknesses obtained on the curves within the study area showed one main aquifer type, which is the fractured basement. The longitudinal unit conductance (ranging from 0.049720 to 1.4520000 mhos) of the study area aided the protective capacity to be rated into good, moderate and weak. About 33% of the study area falls within the weak protective capacity, 57% falls within the moderate protective capacity and 10% falls within the good protective capacity.

Key words: Groundwater potential, protective capacity, vertical electrical sounding, longitudinal unit conductance, overburden thickness

Povzetek

Raziskava hidrogeoloških podzemnih virov je potekala z namenom ocenitve potenciala vodonosnika za zagotovitev preskrbe z vodo. Pri tem je bila narejena porazdelitev električnih parametrov hidrogeoloških enot na nekaterih območjih kraja Odeda. Uporabljena je bila geofizikalna raziskava z navpičnim električnim sondiranjem (VES) z uporabo Schlumbergerjeve elektrodne postavitve s polovično razdaljo elektrode (AB/2), ki je variirala med 1 in 132 m. Preiskava je bila izvedena na 30 različnih lokacijah. Izmerjeni podatki so bili interpretirani kvalitativno in kvantitativno. Razmejenih je bilo tri do pet podzemnih plasti, ki so jih sestavljale: vrhnja plast, preperela plast (sestavljena iz gline, peščene gline, zaglinjenega peska), peščena plast in razpokana sveža podlaga. Upornost in debelina posameznih plasti kaže na eno glavno vrsto vodonosnika (razpokana podlaga). Glede na vzdolžno prevodnost (v območju med 0.049720 do 1.452000 mhos) raziskovanega območja je mogoče zaščitno zmogljivost vodonosnika razvrstiti v dobro, srednjo in slabo. Okoli 33% raziskovanega območja leži znotraj slabe, 57% znotraj srednje in 10% znotraj dobre zaščitne sposobnosti.

Ključne besede: potencial podzemne vode, zaščitna zmogljivost, navpično električno sondiranje, vzdolžna prevodnost, debelina nadkritja

Introduction

In ensuring livelihood and sustainability across the world, groundwater resources play a major and concrete role. Consumption of groundwater as a feasible source of drinking, domestic, industrial and agricultural needs has proven to be not only safer but also more economical than surface water, as it is commonly unpolluted and available. In recent years, investigation of groundwater sources has become a burning issue and a major concern as groundwater basins are being rapidly stressed due to population explosion, high level of urbanisation, industrialisation and other human activities. Presently, the percentage increase in water usage on a global scale has exceeded twice that of the population [1].

Pores and fractured rock formations in the sub-surface are usually hosts of groundwater. In the basement terrain, groundwater occurs within the overlying unconsolidated material derived directly from weathering of rocks and fractured/faulted bedrock, while in the sedimentary terrain, groundwater occurs within the porous and permeable layer of the saturated zone in the sub-surface [2, 3]. Over the years, groundwater exploration has been carried out using geophysical methods, which include electrical resistivity surveying, electromagnetic techniques and seismic methods, to obtain accurate information about the sub-surface settings, such as aquifer's nature, type and depth of materials (consolidated or unconsolidated), depth of weathered or fractured zone, depth to groundwater, depth to bedrock and salt intrusions into groundwater [4].

Aquifers in the Precambarian basement complex are vulnerable to surface or near-surface contaminants as they commonly occur at shallow depths. Hence, successful exploration of groundwater in a basement terrain requires proper understanding of the hydrogeological characteristics of the aquifer units in relation to their susceptibility to environmental pollution and assessment of their protective capacity [3, 5]. One of the most effective ways of evaluating an environment without interfering with the hydrogeological system is through geophysical studies [6]. Over the years, geophysical survey using the vertical electrical sounding (VES) method has been applied in groundwater exploration within the basement complex rocks in Nigeria [7–10].

VES using the Schlumberger array method was carried out at 30 different stations in the study area with the aim to determine the geoelectric parameters, such as resistivities and thicknesses of the sub-surface layers and their hydrogeological properties. This study was also aimed at evaluating the groundwater potential of the area, establishing the aquifer protective capacity of the overlying formations, especially its isolation from contamination, and recommending suitable points for groundwater positioning.

Location and Geology of the Study Area

The study area, as shown in Figure 1, is located between latitudes 7°10'N and 7°12'N and between longitudes 3°23'E and 3°28'E. The study area is characterised by tropical climate with distinct wet and dry seasons. The annual rainfall ranges from 1400 mm to 1500 mm; the mean temperature is 30°C and varies from 25.7°C in July to 30.2°C in February [11]. The study area is underlain by Precambarian basement rocks (Figure 2), which are innately characterised by near-negligible permeability and low porosity. These rocks, according to a previous paper [12], were acknowledged to belong to the youngest of the three major provinces of the West African Craton. These rocks are of Precambarian age to early Palaeozoic age, which extends from the Northeastern part of Ogun State and dips towards the coast [13].

Materials and Methods

The electrical resistivity survey method using the VES method was carried out in the study area. The resistivity data were acquired using Campus Ohmega Terrameter. Thirty VES points were positioned in the study area using Schlumberger electrode configuration with half-current electrode separation (AB/2) ranging from 1 m to 132 m. The apparent resistivity values were obtained as the product of the resistance read from the resistivity meter

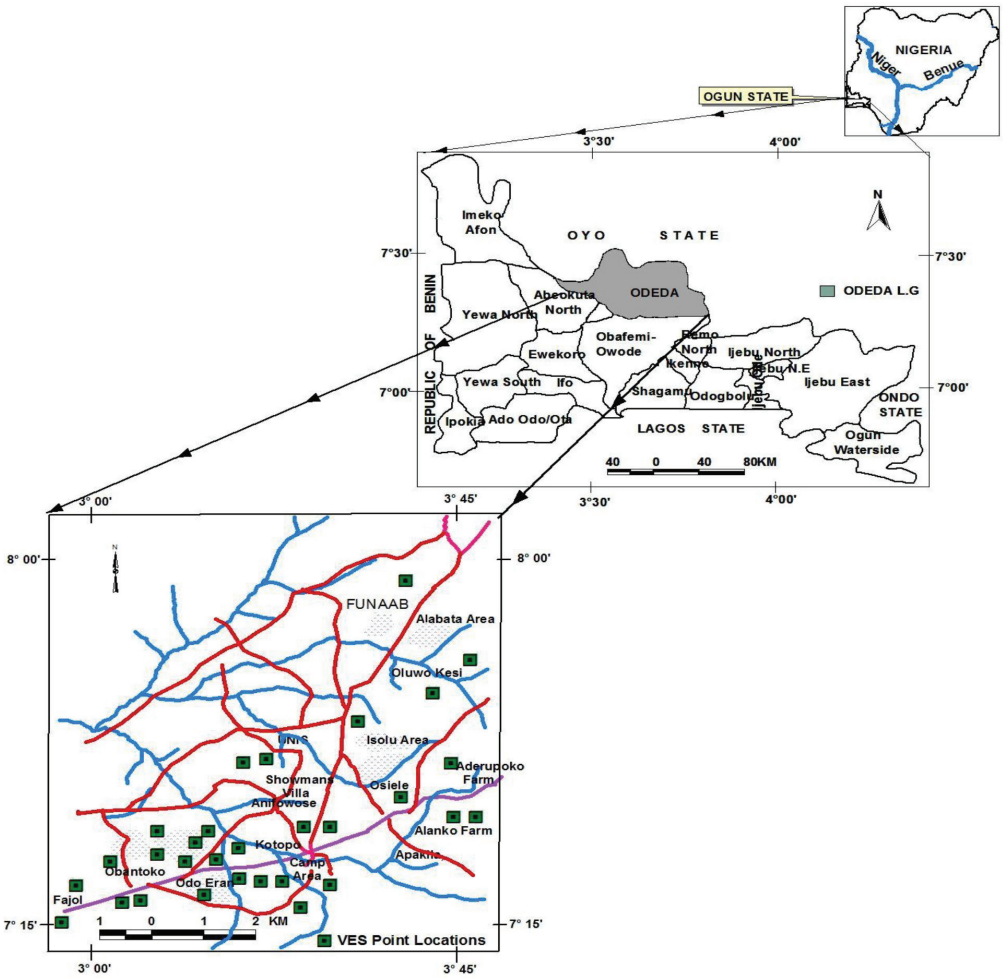

Figure 1: *Map of the study area showing the sounding points.*

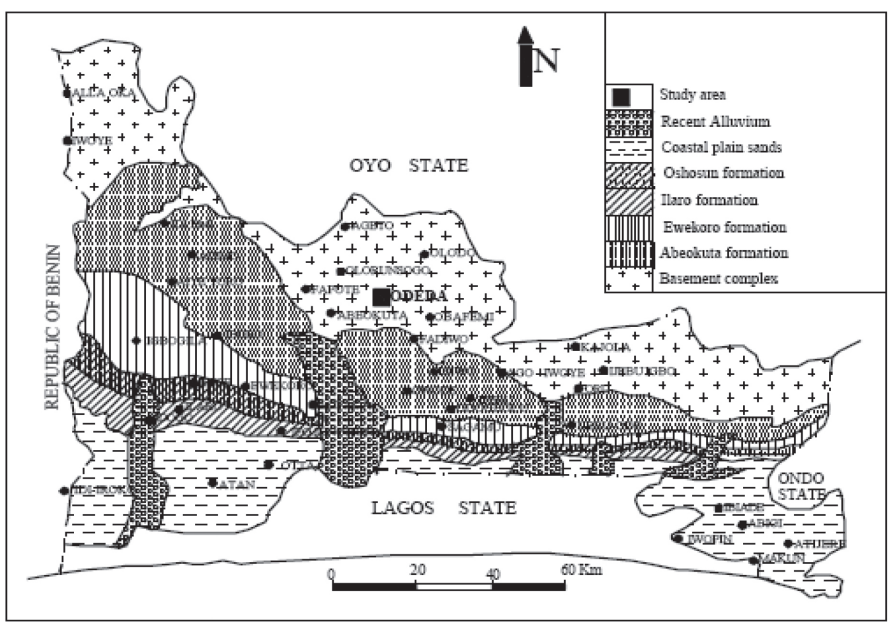

Figure 2: *Geological map of Ogun State. Modified after Badmus and Olatinsu [14].*

Table 1: *Longitudinal unit conductance/protective capacity rating (source: Oladapo and Akintorinwa [18]).*

Total longitudinal unit conductance (mhos)	Rating of overburden's aquifer protective capacity
<0.10	Poor
0.1–0.19	Weak
0.2–0.79	Moderate
0.8–4.90	Good
5.0–10.0	Very good
>10.0	Excellent

Table 2: *Groundwater potential yield (modified after Bayewu et al. [3]).*

Overburden thickness (m)	Reflection coefficient	Groundwater yield
>13	<0.8	High
>13	>0.8	Medium
<13	>0.8	Low
<13	<0.8	Very low

and its corresponding geometric factor (K) for each electrode separation. The apparent resistivity data were then plotted against AB/2 on a bi-logarithm graph as sounding curves. The plotted sounding curves were interpreted manually by partial curve matching using different master curves [15]. The geoelectric parameters from the partial curve matching served as the input model for computer-assisted iteration using WINRESIST.

The values of the longitudinal unit conductance of the overburden rock units in the study area serve as the basis for the characterisation of its aquifer protective capacity. The longitudinal unit conductance gives a measure of the impermeability of the confining clay layer, which has low resistivity and low hydraulic conductivity. The protective capacity of the overburden layers in a particular area is proportional to the longitudinal unit conductance [16]. The longitudinal layer conductance (S) of the overburden at each VES station was obtained as shown in Equation (1) [17].

$$S = \sum_{i=1}^{n} \frac{h_i}{\rho_i} \tag{1}$$

where h_i is the layer thickness, ρ_i is the layer resistivity, while the number of layers from the surface to the top of the aquifer varies in the range $i = 1, \ldots, n$. The results of the longitudinal unit conductance were used to classify the areas into good, moderate, weak and poor aquifer protective capacity (Table 1). This was done using the classification given by Oladapo and Akintorinwa [18].

Olayinka [19] opined that in identifying areas of favourable aquifers within a basement terrain, the resistivity of the basement cannot be exclusively relied upon; hence, one has to consider the basement's reflection coefficient in effectively evaluating groundwater potential in the study area. The degree of fracturing of the underlying basement is shown by the reflection coefficient [3]. The reflection coefficients (r) of the study area were calculated using Equation (2), as given by Bhattacharya and Patra [20] and Loke [21].

$$r = \frac{(\rho n - \rho(n-1))}{(\rho n + \rho(n-1))} \tag{2}$$

where ρn is the layer resistivity of the nth layer and $\rho(n-1)$ is the layer resistivity overlying the nth layer.

In a basement terrain, groundwater yield can be grouped into high, medium and low depending on the overburden thickness and/or reflection coefficient (Table 2), as stated by Bayewu et al. [3]. The highest groundwater yield is found in areas where thick overburden overlies the fractured zone [18].

Results and Discussion

The summary of the geoelectric parameters and inferred lithologies in the study area is presented in Table 3. The curve types obtained after partial curve matching ranges from the three-layer H type (66.7%), A type (3.3%) and K type (3.3%), through the four-layer KH type (23.3%), to the five-layer curve HKH type (3.3%). The predominant H type curve recorded in the study area further affirmed the findings of Oloruntola and Adeyemi [9], who recorded >72% of H curve type in the basement geological terrain at Abeokuta. Figures 3 and 4 show the typical iterated curves generated from the field measurements. The geoelectric interpretations revealed three to five layers, as follows: topsoil (23–700 Ωm); the weathered layer, which is composed of clay/sandy clay and clayey sand/sand (4–790 Ωm); underlying this layer are the fractured layer (93–437 Ωm) and the fresh basement (532–2106 Ωm). The aquifer unit in the study area is basically found in the fractured layer, the yield being dependent on the amount of clay content.

Table 3: *Summary of geoelectric parameters and inferred lithologies.*

VES no.	No. of layers	Curve types	Resistivity (Ωm)	Thickness (m)	Depth (m)	Reflection coefficient	Inferred lithology
1	1	H	117	2.3	2.3	0.876	Topsoil
	2		29	25.5	27.8		Clay
	3		437				Fractured basement
2	1	H	211	0.9	0.9	0.421	Topsoil
	2		110	5.0	5.9		Sandy clay
	3		270				Fractured basement
3	1	H	324	1.3	1.3	0.437	Topsoil
	2		162	13.1	14.4		Clayey sand
	3		413				Fractured basement
4	1	H	75	2.1	2.1	0.843	Topsoil
	2		30	24.1	26.2		Clay
	3		352				Fractured basement
5	1	H	100	1.2	1.2	0.977	Topsoil
	2		5	7.2	8.4		Clay
	3		427				Fractured basement
6	1	HKH	134	0.6	0.6	0.899	Topsoil
	2		35	1.8	2.4		Clay
	3		79	3.4	5.8		Sandy clay
	4		17	8.8	14.6		Clay
	5		318				Fractured basement
7	1	H	94	0.8	0.8	0.778	Topsoil
	2		24	4.9	5.7		Clay
	3		192				Fractured basement
8	1	H	30	1.0	1.0	0.996	Topsoil
	2		4	2.0	3.0		Clay
	3		2106				Fresh basement
9	1	KH	94	1.2	1.2	0.701	Topsoil
	2		120	6.6	7.8		Sandy clay
	3		60	11.8	19.6		Clay
	4		342				Fractured basement
10	1	H	109	0.8	0.8	0.489	Topsoil
	2		32	7.2	9		Clay
	3		93				Fractured basement
11	1	KH	26	0.6	0.6	0.841	Topsoil
	2		655	5.1	5.7		Sand
	3		51	13.1	18.8		Clay
	4		592				Fresh basement
12	1	KH	161	0.9	0.9	0.315	Topsoil
	2		191	9.1	10		Clayey sand
	3		114	8.6	18.6		Sandy clay
	4		219				Fractured basement

Table 3: *Summary of geoelectric parameters and inferred lithologies.*

13	1	H	369	2.6	2.6	0.625	Topsoil
	2		62	19.7	22.3		Clay
	3		269				Fractured basement
14	1	KH	269	0.7	0.7	0.534	Topsoil
	2		327	3.2	3.9		Sand
	3		198	8.8	12.7		Clayey sand
	4		652				Fresh basement
15	1	H	167	1.2	1.2	0.576	Topsoil
	2		66	12.7	13.9		Clay
	3		245				Fractured basement
16	1	H	700	1.5	1.5	0.887	Topsoil
	2		38	8.3	9.8		Clay
	3		637				Fresh basement
17	1	H	417	1.0	1.0	0.744	Topsoil
	2		61	8.7	9.7		Clay
	3		415				Fractured basement
18	1	H	81	2.3	2.3	0.880	Topsoil
	2		27	10	12.3		Clay
	3		422				Fractured basement
19	1	KH	34	0.5	0.5	0.761	Topsoil
	2		790	2.5	3.0		Sand
	3		59	12.6	15.6		Clay
	4		435				Fractured basement
20	1	KH	103	1.0	1.0	0.615	Topsoil
	2		146	2.1	3.1		Clayey sand
	3		40	16.8	19.9		Clay
	4		168				Fractured basement
21	1	H	273	1.7	1.7	0.702	Topsoil
	2		35	11.1	12.8		Clay
	3		200				Fractured basement
22	1	H	329	3.5	3.5	0.237	Topsoil
	2		135	35.5	39		Sandy clay
	3		219				Fresh basement
23	1	H	226	2.0	2.0	0.921	Topsoil
	2		42	19.4	21.4		Clay
	3		1019				Fresh basement
24	1	H	285	0.8	0.8	0.759	Topsoil
	2		99	7.8	8.6		Clay
	3		722				Fresh basement
25	1	A	23	0.8	0.8	0.777	Topsoil
	2		49	16.6	17.4		Clay
	3		391				Fractured basement
26	1	K	63	1.0	1.0	0.553	Topsoil
	2		153	16.0	17.0		Clayey sand
	3		532				Fresh basement
27	1	H	149	1.0	1.0	0.643	Topsoil
	2		81	10.4	11.4		Clay
	3		373				Fractured basement
28	1	KH	108	1,6	1.6	0.889	Topsoil
	2		296	6.7	8.3		Sand
	3		82	9.2	17.5		Clay
	4		1391				Fresh basement
29	1	H	161	1.0	1.0	0.522	Topsoil
	2		65	10.0	11.0		Clay
	3		207				Fractured basement
30	1	H	274	2.6	2.6	0.830	Topsoil
	2		40	19.6	22.2		Clay
	3		431				Fresh basement

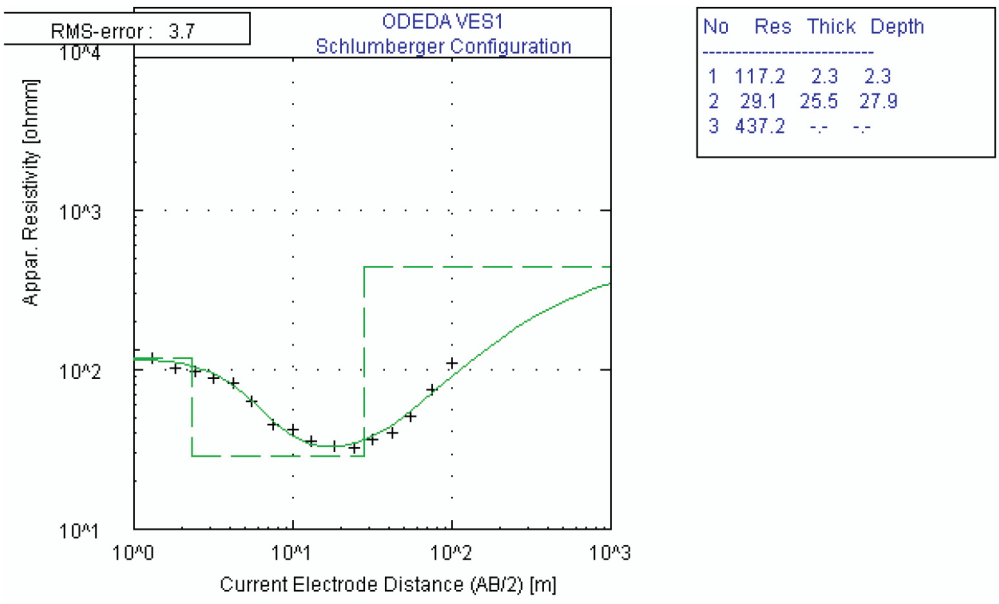

Figure 3: *Typical VES curve in the study area.*

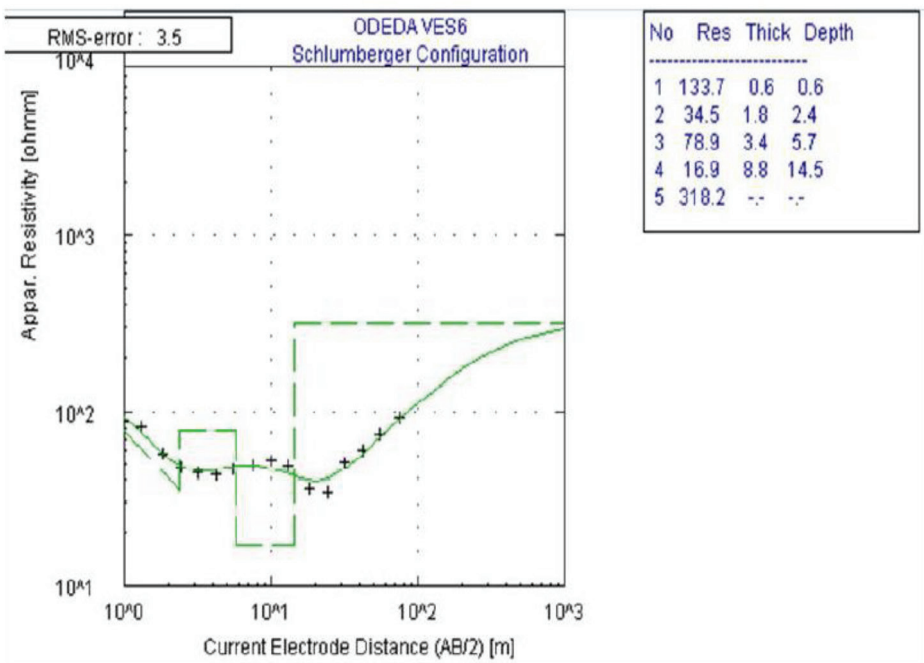

Figure 4: *Typical VES curve in the study area.*

Assessment of Aquifer Protective Capacity

The resistivities and thicknesses of the underground layers were used to compute the longitudinal unit conductance (S) of the layers in the study area. Table 4 shows the calculated longitudinal unit conductance in mhos and the protective capacity rating for the study area. The longitudinal unit conductance values of the overburden materials in the study area ranged from 0.049720 to 1.452000 mhos. It can be observed that the protective capacity in the study area reveals poor, weak, moderate and good capacity rating. Four VES stations have poor protective capacity, six shows weak protective

Table 4: *Longitudinal unit conductance and aquifer protective capacity of the study area.*

VES no.	Longitudinal unit conductance (mhos)	Overburden's aquifer protective capacity rating
1	0.898968	Good
2	0.049720	Poor
3	0.084877	Poor
4	0.824333	Good
5	1.452000	Good
6	0.616591	Moderate
7	0.212677	Moderate
8	0.533333	Moderate
9	0.264433	Moderate
10	0.232339	Moderate
11	0.287726	Moderate
12	0.128673	Weak
13	0.324788	Moderate
14	0.056833	Poor
15	0.199610	Moderate
16	0.220564	Moderate
17	0.145021	Weak
18	0.398765	Moderate
19	0.231430	Moderate
20	0.444092	Moderate
21	0.323370	Moderate
22	0.273601	Moderate
23	0.470754	Moderate
24	0.081595	Poor
25	0.373558	Moderate
26	0.120448	Weak
27	0.135106	Weak
28	0.149645	Weak
29	0.160057	Weak
30	0.499489	Moderate

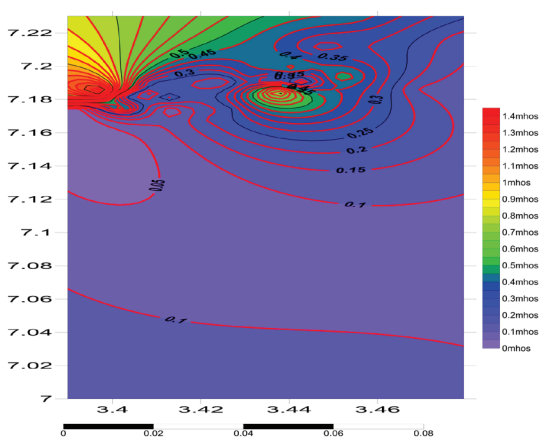

Figure 5: *The longitudinal unit conductance map of the study area.*

capacity, 17 show moderate protective capacity, while three show good protective capacity rating, with 33% of the study area falling within the poor/weak overburden protective capacity. About 57% falls within the moderate range, while 10% falls within good overburden protective capacity. The longitudinal unit conductance map of the study area in Figure 5 shows that the northeastern and northwestern parts of the study area are characterised by moderate-to-good protective capacity, and this signifies that there is a little or no infiltration due to precipitation.

Assessment of Groundwater Potential

Figures 6 and 7 show the reflection coefficient and overburden thickness map of the study area. The reflection coefficient in the study area varies from 0.24 to 1.00. The groundwater prospects in the study area are categorised

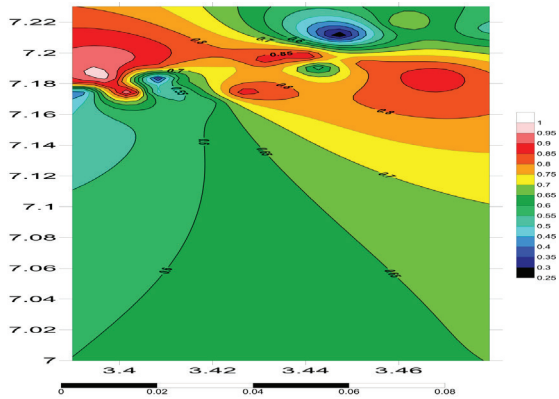

Figure 6: *The reflection coefficient map of the study area.*

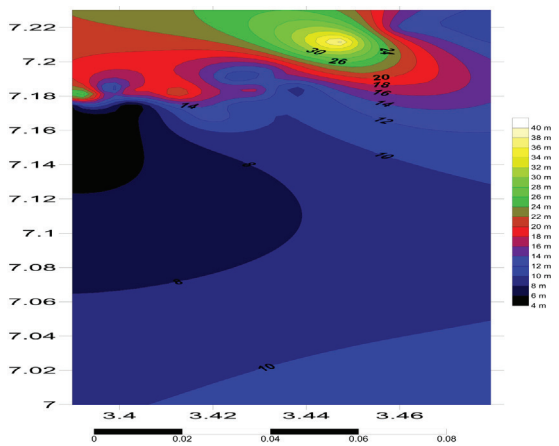

Figure 7: *Isopach map of overburden thickness of the study area.*

into high, medium and low potentials. In this study, zones where the overburden thickness is >13 m and the reflection coefficient is <0.8 are considered as zones with high groundwater potential, while zones with overburden thickness <13 m and reflection coefficient <0.8 are considered as zones having very low groundwater potential.

Generally, about 33% of the study area has high groundwater potential, which is restricted mostly to areas underlain by porphyritic granite and porphyroblastic gneiss, as established by a previous paper [22], while 23% of the study area has medium groundwater potential; moreover, 43% of the area has low groundwater potential. This result invariably indicates the significance of detailed groundwater survey and exploration in the study area for locating areas where successful boreholes can be sited.

Table 5: *Groundwater potential across the VES locations.*

VES no.	Overburden thickness (m)	Reflection coefficient	Groundwater yield
1	27.8	0.876	Medium
2	5.9	0.421	Very low
3	14.4	0.437	High
4	26.2	0.843	Medium
5	8.4	0.977	Low
6	14.6	0.899	Medium
7	5.7	0.778	Very low
8	3.0	0.996	Low
9	19.6	0.701	High
10	9.0	0.489	Very low
11	18.8	0.841	Medium
12	18.6	0.315	High
13	22.3	0.625	High
14	12.7	0.534	Very low
15	13.9	0.576	High
16	9.8	0.887	Low
17	9.7	0.744	Very low
18	12.3	0.880	Low
19	15.6	0.761	High
20	19.9	0.615	High
21	12.8	0.702	Very low
22	39.0	0.237	High
23	21.4	0.921	Medium
24	8.6	0.759	Very low
25	17.4	0.777	High
26	17.0	0.553	High
27	11.4	0.643	Very low
28	17.5	0.889	Medium
29	11.0	0.522	Very low
30	22.2	0.830	Medium

Conclusion

The geoelectric investigation of the study area has revealed three to five subsurface geoelectric layers: top soil, weathered basement and fresh basement rocks. The fractured layer constitutes the sole aquifer unit in the study area. The protective capacity in the study area is more of the moderate type and is therefore not exposed to pollution. About 33% of the study area falls within the high rated groundwater po-

tential zone, while the remaining 67% constituted the medium/low groundwater potential zone. Hence, the groundwater potential rating of the area is considered generally as medium/low. Therefore, areas for locating groundwater should be narrowed to zones of moderate/good groundwater protective capacity.

Acknowledgement

The authors are grateful to Mr. Afolabi and Mr. Oluwaseun Dada for their support in the collection of data on the field.

References

[1] Cosgrove, W.J., Loucks, D.P. (2015): Water Management: Current and Future Challenges and Research Directions. *Water Resources Research*, 51(6), pp. 4823–4839.

[2] Adagunodo, M.K., Sunmonu, L.A., Aizebeokhai, A.P., Oyeyemi, K.D., Abodunrin, F.O. (2018): Groundwater Exploration in Aaba Residential Area of Akure, Nigeria. *Front. Earth Science,* 66(6), pp. 1–12, DOI: 10.3389/feart.2018.00066.

[3] Bayewu, O.O., Oloruntola, M.O., Mosuroa, G.O., Laniyana, T.A., Ariyo, S.O., Fatoba, J.O. (2018): Assessment of groundwater prospect and aquifer protective capacity using resistivity method in Olabisi Onabanjo University campus, Ago-Iwoye, Southwestern Nigeria. *NRIAG Journal of Astronomy and Geophysics*, 7, pp. 347–360.

[4] Sajeena, S., Abdul Hakkim, V.M., Kurien, E.K. (2014): Identification of Groundwater Prospective Zones Using Geoelectrical and Electromagnetic Surveys. *International Journal of Engineering Inventions*, 3(6), pp. 17–21.

[5] Abiola, O., Enikanselu, P.A., Oladapo, M.I. (2009): Groundwater potential and aquifer protective capacity of overburden units in Ado-Ekiti, southwestern Nigeria. *International Journal of Physical Sciences*, 4(3), pp. 120–132.

[6] Mogaji, K.A., Adiat, K.A.N., Oladapo, M.I. (2007): Geoelectric investigation of the Dape phase III housing estate, FCT Abuja, North Central Nigeria. *Journal of Earth Sciences*, 1(2), pp. 76–84.

[7] Ayuk, M.A., Adelusi, A.O., Adiat, K.A.N. (2013): Evaluation of groundwater potential and aquifer protective capacity assessment at Tutugbua-Olugboyega area, off Ondo road, Akure Southwestern Nigeria. *International Journal of Physical Sciences*, 8(1), pp. 37–50.

[8] Ademilua, O.L., Eluwole, A.B. (2013): Hydrogeophysical Evaluation of the Groundwater Potential of Afe Babalola University Ado-Ekiti, Southwestern Nigeria. *Journal of Emerging Trends in Engineering and Applied Sciences (JETEAS),* 4(1), pp. 77–83.

[9] Oloruntola, M.O., Adeyemi, G.O. (2014): Geophysical and Hydrochemical Evaluation of Groundwater Potential and Character of Abeokuta Area, Southwestern Nigeria. *Journal of Geography and Geology*, 6(3), pp. 162–177.

[10] Abdullahi, M.G, Toriman, M.E., Gasim, M.B. (2015): The Application of Vertical Electrical Sounding (VES) for Groundwater Exploration in Tudun Wada Kano State, Nigeria. *Journal of Geology and Geosciences*, 4(1), pp. 1–3.

[11] Adeleke, O.O., Makinde, V., Eruola, A.O., Dada, O.F., Ojo, A.O., Aluko, T.J. (2015): Estimation of Groundwater Recharges in Odeda Local Government Area, Ogun State, Nigeria using Empirical Formulae. *Challenges,* 6, pp. 271–281.

[12] Hurley, P.M., Rank, J.R. (1976): Outline of Precambrian Chronology in lands bordering the South Atlantic exclusive of Brasil. In: *The Ocean Basins and Margins*, Nairn, Stehli (eds.). Plenum Press, pp. 391–410.

[13] Ako, B.D. (1979): *Geophysical Prospecting for Groundwater in Parts of South-western Nigeria*. Unpublished Ph. D. Thesis. Department of Geology, University of Ife: Ile-Ife, Nigeria, 371 p.

[14] Badmus, B.S., Olatinsu, O.B. (2010): Aquifer characteristics and groundwater recharge pattern in a typical basement complex, Southwestern Nigeria. *African Journal of Environmental Sciences and Technology*, 4(6), pp. 328–342.

[15] Zohdy, A.A. (1965): The Auxiliary Point Method of Electrical Sounding Interpretation and its relationship to the Dar Zarrouk parameters, *Geophysics*, 30, pp. 644–660.

[16] Tsepav, M.T, Ibrahim, S.I., Bayegun, F.A. (2015): Geoelectrical Characterization of Aquifer Precincts in Parts of Lapai, North Central Nigeria. *Journal of Applied Science and Environmental Management*, 19(2), pp. 295– 301.

[17] Henriet, J.P. (1976): Direct applications of the Dar Zarrouk parameters in ground water surveys. *Groundwater Prospecting*, 24, pp. 345–353.

[18] Oladapo, M.I., Akintorinwa, O.J. (2007): Hydrogeophysical study of Ogbese Southwestern Nige-

ria. *Global Journal of Pure Applied Science*, 13(1), pp. 55–61.

[19] Olayinka, A.I (1996): Non Uniqueness in the Interpretation of Bedrock Resistivity from Sounding Curves and its Hydrological Implications. *Water Resources Journal NAH*, 7(1&2), pp. 55–60.

[20] Bhattacharya, P.K., Patra, H.P. (1968): *Direct Current Geoelectric Sounding Methods in Geochemistry and Geophysics*. Elsevier: Amsterdam, 135 p.

[21] Loke, M.H. (1999): Time-lapse resistivity imaging inversion. In: *Proceedings of the 5th Meeting of the Environmental and Engineering Geophysical Society European Section, Em1.* 90 p.

Instructions for Authors

RMZ – MATERIALS & GEOENVIRONMENT (RMZ – Materiali in geookolje) is a periodical publication with four issues per year (established in 1952 and renamed to RMZ – M&G in 1998). The main topics are Mining and Geotechnology, Metallurgy and Materials, Geology and Geoenvironment.
RMZ – M&G publishes original scientific articles, review papers, preliminary notes, and professional papers in English. Only professional papers will exceptionally be published in Slovene. In addition, evaluations of other publications (books, monographs, etc.), in memoriam, presentation of a scientific or a professional event, short communications, professional remarks and reviews published in RMZ – M&G can be written in English or Slovene. These contributions should be short and clear.
Authors are responsible for the originality of the presented data, ideas and conclusions, as well as for the correct citation of the data adopted from other sources. The publication in RMZ – M&G obligates the authors not to publish the article anywhere else in the same form.

Specification of the Contributions

Optimal number of pages is 7 to 15; longer articles should be discussed with the Editor-in-Chief prior to submission. All contributions should be written using the ISO 80000.

- Original scientific papers represent unpublished results of original research.
- Review papers summarize previously published scientific, research and/or expertise articles on a new scientific level and can contain other cited sources which are not mainly the result of the author(s).
- Preliminary notes represent preliminary research findings, which should be published rapidly (up to 7 pages).
- Professional papers are the result of technological research achievements, application research results and information on achievements in practice and industry.
- Publication notes contain the author's opinion on newly published books, monographs, textbooks, etc. (up to 2 pages). A figure of the cover page is expected, as well as a short citation of basic data.
- In memoriam (up to 2 pages), a photo is expected.
- Discussion of papers (Comments) where only professional disagreements of the articles published in previous issues of RMZ – M&G can be discussed. Normally the source author(s) reply to the remarks in the same issue.
- Event notes in which descriptions of a scientific or a professional event are given (up to 2 pages).

Review Process

All manuscripts will be supervised shall undergo a review process. The reviewers evaluate the manuscripts and can ask the authors to change particular segments, and propose to the Editor-in-Chief the acceptability of the submitted articles. Authors are requested to identify three reviewers and may also exclude specific individuals from reviewing their manuscript. The Editor-in-Chief has the right to choose other reviewers. The name of the reviewer remains anonymous. The technical corrections will also be done and the authors can be asked to correct the missing items. The final decision on the publication of the manuscript is made by the Editor-in-Chief.

Form of the Manuscript

All papers must be submitted via the online system.
The original file of the Template is available on RMZ – Materials and Geoenvironment Home page address: **www.rmz-mg.com**.

The contribution should be submitted in Microsoft Word. Manuscript should be written in Arial font and 12 pt font with 1.5 line spacing and should contain all figures, tables and formulas. Headings should be written in Arial bold font and shuold not be numbered. Subheadings should be written in Arial italic font. The electronic version should be simple, without complex formatting, hyphenation, and underlining. For highlighting, only bold and italic types should be used.

Annexes

Annexes are images, spreadsheets, tables, and mathematical and chemical formulas. Math formulas should be included in article as editable text and not as images.
Annexes should be included in the text at the appropriate place, and they should also be submitted as a separate document, i.e. separated from the text in the article.
Annexes should be originals, made in an electronic form (Microsoft Excel, Adobe Illustrator, Inkscape, AutoCad, etc.) and in .eps, .tif or .jpg format with a resolution of at least 300 dpi.
The width of the annex should be at least 152 mm. They should be named the same as in the article (Figure 1, Table 1). The text in the annexes should be written in typeface Arial Regular (6 pt).
The title of the image (also schemes, charts and graphs) should be indicated in the description of the image.
When formatting spreadsheets and tables in text editors, tabs, and not spaces, should be used to separate columns.
Each formula should have its number written in round brackets on its right side.
References of the annexes in the text should be as follows: "Figure 1…" and not "as shown below:". This is due to the fact that for technical reasons the annex cannot always be placed at the exact specific place in the article.

Composition of the Manuscript

Title
The title of the article should be precise, informative and not longer that 100 characters. The author should also indicate the short version of the title. The title should be written in English as well as in Slovene..

Information on the Authors
Information on the authors should include the first and last name of the authors, the address of the institution and the e-mail address of the corresponding author.

Abstract
The abstract presenting the purpose of the article and the main results and conclusions should contain no more than 180 words. It should be written in Slovene and English.

Key words
A list of up to 5 key words (3 to 5) that will be useful for indexing or searching. They should be written in Slovene and English.

Introduction

Materials and methods

Results and discussion

Conclusions

Acknowledgements

References

The references should be cited in the same order as they appear in the article. **Where possible the DOI for the reference should be included at the end of the reference.** They should be numbered in square brackets. References should be cited according SIST ISO 690:1996 standards.

Book:
[1] Reynolds, J.M. (2011). *An introduction to Applied and Environmental Geophysics*. New York: Wiley, 710 p.

Unpublished Master thesis or PhD dissertation:
[2] Trček, B. (2001): *Solute transport monitoring in the unsaturated zone of the karst aquifer by natural tracers*. Ph. D. Thesis. Ljubljana: University of Ljubljana 2001; 125 p.

Chapter in an edited book:
[3] Blindow, N., Eisenburger, D., Illich, B., Petzold, H., Richer, T. (2007): *Ground Penetrating Radar*. In: Environmental Geology: Handbook of Field Methods and Case Studies, Knödel, K., Lange, G., Voigt, H.J. (eds.). Springer: Berlin; pp. 283–335.

Journal article : Journal title should be complete and not abbreviated.
[4] Higashitani, K., Iseri, H., Okuhara, K., Hatade, S. (1995): Magnetic Effects on Zeta Potential and Diffusivity of Nonmagnetic Particles. *Journal of Colloid and Interface Science*, 172, pp. 383–388.
[5] Mcmechan, G.A, Loucks, R.G, Mescher, P.A, Xiaoxian, Z. (2002): Characterization of a coalesced, collapsed paleocave reservoir analog using GPR and well-core data. *Geophysics*, 67, pp. 1148–1158. doi: 10.1190/1.1500376

Proceedings Paper:
[6] Benac, Č., Gržančić, Ž., Šišić, S., Ružić, I. (2008): Submerged Karst Phenomena in the Kvarner Area. In: Proceedings of the 5th International ProGEO Symposium on Conservation of the Geological Heritage, Rab, Croatia, Marjanac, T (ed.). Pro GEO Croatia: Zagreb; pp. 12–13.

Electronic source:
[7] CASREACT – Chemical reactions database [online]. Chemical Abstracts Service, 2000, renewed 2/15/2000 [cited 2/25/2000]. Available on: <http://www.cas.org/casreact.html>.

Scientific articles, review papers, preliminary notes and professional papers are published in English. Only professional papers will exceptionally be published in Slovene.

Units

SI System should be used for units. Physical quantities should be written in Italics (e.g. m, l, v, T). Symbols for units should be in plain text with spaces (e.g. 10 m, 5.2 kg/s, 2 s-1, 50 kPa). All abreviations should be spelt out in full on first appearance.

Manuscript Submission

Please submit your article via RMZ-M&G Editorial Manager System. You can find it on the address:
http://edmgr.editool.com/rmzmag/default.htm

Log in as an author and submit your article.
You can follow the status of your submission in the system manager and your e-mail.

Information on RMZ – M&G

— Assistant editor
  Jože Žarn
  E-mail address: joze.zarn@ntf.uni-lj.si

— Secretary
  Vukič Nivesč
  Telephone: +386 01 47 04 610
  E-mail address: nives.vukic@ntf.uni-lj.si

These instructions are valid from April 2017.